

Performance Analysis of Cellular and Ad-Hoc Sensor Networks: Theory and Applications

Hebatallah Shoukry

Electrical, Electronic and Computer Engineering Department
Institute of Sensors, Signals and Systems (ISSS)
School of Engineering and Physical Sciences
Heriot-Watt University
Edinburgh, United Kingdom

Under the supervision of

Prof. Mathini Sellathurai

Prof. John Thompson



A Thesis Submitted for the Degree of
Doctor of Philosophy (PhD) in Electrical Engineering
· Sep. 2019 ·

The copyright in this thesis is owned by the author. Any quotation from the thesis or use of any of the information contained in it must acknowledge this thesis as the source of the quotation or information.

Abstract

Fifth-generation (5G) mobile networks have three main goals namely enhanced mobile broadband (eMBB), massive machine-type communication (mMTC) and ultra-reliable low latency communication (URLLC). The performance measures associated with these goals are high peak throughput, high spectral efficiency, high capacity and mobility. Moreover, achieving ubiquitous coverage, network and device energy efficiency, ultra-high reliability and ultra-low latency are associated with the performance of 5G mobile networks. One of the challenges that arises during the analysis of these networks is the randomness of the number of nodes and their locations. Randomness is an inherent property of network topologies and could occur due to communication outage, node failure, blockage or mobility of the communication nodes. One of the tools that enable analysis of such random networks is stochastic geometry, including the point process theory. The stochastic geometry and Poisson point theory allow us to build upon tractable models and study the random networks, which is the main focus of this dissertation. In particular, we focus on the performance analysis of cellular heterogeneous networks (HetNet) and ad-hoc sensor networks. We derive closed-forms and easy-to-use expressions, characterising some of the crucial performance metrics of these networks. First, as a HetNet example, we consider a three-tier hybrid network, where microwave (μ Wave) links are used for the first two tiers and millimetre wave (mmWave) links for the last tier. Since HetNets are considered as interference-limited networks, therefore, we also propose to improve the coverage in HetNet by deploying directional antennas to mitigate interference. Moreover, we propose an optimisation framework for the over-

all area spectral and energy efficiency concerning the optimal signal-to-interference ratio (SIR) threshold required for μ Wave and mmWave links. Results indicate that for the μ Wave tiers (wireless backhaul) the optimal SIR threshold required depends only on the path-loss exponent and that for the mmWave tier depends on the area of line-of-sight (LOS) region. Furthermore, we consider the average rate under coverage and show that the area spectral and energy efficiency are strictly decreasing functions with respect to the SIR threshold. Second, in ad-hoc sensor networks, coverage probability is usually defined according to a fixed detection range ignoring interference and propagation effects. Hence, we define the coverage probability in terms of the probability of detection for localisability. To this end, we provide an analysis for the detection probability and S -Localisability probability, i.e. the probability that at least S sensors may successfully participate in the localisation procedure, according to the propagation effects such as path-loss and small-scale fading. Moreover, we analyse the effect of the number of sensors S on node localisation and compare different range based localisation algorithms.

Acknowledgements

First, I thank my supervisor Professor Mathini Sellathurai for her support and guidance throughout my Ph.D journey. Her academic expertise has been useful in completing the thesis, and the inspiring discussions have always been my source of motivation. I want to thank my second supervisor Professor John Thompson, the University of Edinburgh, for his beneficial comments on my work. I want to express my gratitude to Professor Kai-Kit Wong and Dr. Muhammed Khandaker for agreeing to be my external and internal examiners. I am grateful to be part of UDRC in Signal Processing for the Mobile Ad-hoc Sensor Networks (MASNET) project funded by DSTL and EPSRC.

I also thank Dr. Naveen Mysore Balasubramanya, Dr. Satyanarayana Vuppala, Dr. George Papageorgiou, Dr. Rongrong Qian and Dr. Navneet Garg for their invaluable help and useful discussions. My office colleagues Ankit, Ross, Darius, Sonam, Dr. Merlinda and Dr. Benoit thank you for your valuable support.

My parents, brother, and in-laws in Egypt, your support, encouragement, and prayers have always been my motivation to fulfil my dream and pursue this degree. I would like to thank my second family in Edinburgh Noha, Maymoona, Iman, Miral, Waqar and Hala, without your prayers and help with my kids' activities I couldn't have done it.

Last but not least, to my husband, Dr. Mohammed Saleh, you have always been my backbone and I can't thank you enough. My adorable kids, Noura and Mahmoud, thank you for your patience and understanding. It was you who made this possible

Research Thesis Submission

Name:	Hebatallah Shoukry		
School:	EPS/ISSS		
Version: <i>(i.e. First, Resubmission, Final)</i>	Final	Degree Sought:	PhD

Declaration

In accordance with the appropriate regulations I hereby submit my thesis and I declare that:

1. The thesis embodies the results of my own work and has been composed by myself
2. Where appropriate, I have made acknowledgement of the work of others
3. The thesis is the correct version for submission and is the same version as any electronic versions submitted*.
4. My thesis for the award referred to, deposited in the Heriot-Watt University Library, should be made available for loan or photocopying and be available via the Institutional Repository, subject to such conditions as the Librarian may require
5. I understand that as a student of the University I am required to abide by the Regulations of the University and to conform to its discipline.
6. I confirm that the thesis has been verified against plagiarism via an approved plagiarism detection application e.g. Turnitin.

ONLY for submissions including published works

7. Where the thesis contains published outputs under Regulation 6 (9.1.2) or Regulation 43 (9) these are accompanied by a critical review which accurately describes my contribution to the research and, for multi-author outputs, a signed declaration indicating the contribution of each author (complete)
8. Inclusion of published outputs under Regulation 6 (9.1.2) or Regulation 43 (9) shall not constitute plagiarism.

* *Please note that it is the responsibility of the candidate to ensure that the correct version of the thesis is submitted.*

Signature of Candidate:		Date:	
-------------------------	--	-------	--

Submission

Submitted By <i>(name in capitals)</i> :	
Signature of Individual Submitting:	
Date Submitted:	

For Completion in the Student Service Centre (SSC)

Limited Access	Requested	Yes	No	Approved	Yes	No
<i>E-thesis Submitted (mandatory for final theses)</i>						
Received in the SSC by <i>(name in capitals)</i> :		Date:				

Inclusion of Published Works

Declaration

This thesis contains one or more multi-author published works. In accordance with Regulation 6 (9.1.2) I hereby declare that the contributions of each author to these publications is as follows:

Citation details	H. Shoukry , N. Mysore Balasubramanya, S. Vuppala and M. Sellathurai. Performance Analysis of a Wireless Backhaul in a Three-Tier Hybrid Network with Directional Antennas, IEEE Access Journal, pp.18332-18344, Jan. 2019.
Hebatallah Shoukry	Analysis of the performance of a three-tier hybrid network using directional antennas, comparing the analytical and simulation results.
All other authors	Supervision on work, Feedback /comments on publication, proofreading
Signature:	
Date:	

Citation details	H. Shoukry , S. Vuppala, P. Chambers, M. Sellathurai and J. Thompson. Non-cooperative target localisation using rank-based EDM Approach. Sensor Signal Processing for Defence Conference (SSPD), pp. 1-4, Dec. 2017.
Hebatallah Shoukry	Applied and EDM rank based algorithm for the considered system model and comparing the results with other conventional algorithms.
All other authors	Supervision on work, Feedback /comments on publication, proofreading
Signature:	
Date:	

Citation details	H.Shoukry , R.Qian and M.Sellathurai. Performance Analysis in indoor Femtocell Networks using ESPAR antennas. IEEE 17 th International Workshop on Signal Processing Advances in Wireless Communications (SPAWC), PP. 1-5, Jul., 2016
Hebatallah Shoukry	Analysis of the performance of single-tier network using ESPAR antennas, comparing the analytical and simulation results.
All other authors	Supervision on work, Feedback /comments on publication, proofreading
Signature:	
Date:	

Publications Related to the PhD Thesis

- **H. Shoukry**, R. Qian and M. Sellathurai. Performance analysis in indoor femtocell networks using ESPAR antennas. 2016 IEEE 17th International Workshop on Signal Processing Advances in Wireless Communications (SPAWC), pp. 1-5, Jul., 2016.
- **H. Shoukry**, S. Vuppala, P. Chambers, M. Sellathurai and J. Thompson. Non-Cooperative Target Localisation Using Rank Based EDM Approach. 2017 Sensor Signal Processing for Defence Conference (SSPD), pp.1-4, Dec., 2017.
- **H. Shoukry**, N. Mysore Balasubramanya, S. Vuppala and M. Sellathurai. Performance Analysis of a Wireless Backhaul in a Three-Tier Hybrid Network With Directional Antennas. IEEE Access Journal, pp. 18332-18344, Jan., 2019.
- **H. Shoukry**, et. al. Tractable Analysis of Target Detection and Localisation in a three dimensional MASNET. in preparation for submission, Mar., 2020

Acronyms and Notations

Acronyms

SCN	Small Cell Network
HetNet	Heterogeneous Networks
UT	User Terminal
ESPAR	Electronically Steerable Parasitic Array Receptor
RF	Radio Frequency
FAP	Femtocell Access Point
μ Wave	Microwave
mmWave	Millimetre Wave
SIR	Signal-to-Interference Ratio
SNR	Signal-to-Noise Ratio
SINR	Signal-to-Interference-plus-Noise Ratio
LOS	Line-of-Sight
NLOS	Non-Line-of-Sight
PPP	Poisson Point Process
EDM	Euclidean Distance Matrices

FC	Fusion Centre
LLS	Linear Least Squares
ToA	Time of Arrival
TDoA	Time-Difference of Arrival
LS	Least Squares
WLS	Weighted Least Squares
SRD-LS	Squared-Range-Difference-based Least Squares
SPPP	Spatial Poisson Point Process
MASNET	Mobile Ad-hoc Sensor Networks
PDF	Probability Density Function
CDF	Cumulative Distribution Function
BS	Base-Station
ASE	Area Spectral Efficiency
EE	Energy Efficiency
5G	Fifth-Generation
UHF	Ultra-High Frequency
MIMO	Multiple-Input Multiple-Output
MBS	Macro Base Station
RSS	Received Signal Strength
WSN	Wireless Sensor Network

AoA	Angle of Arrival
DDG	Distributed Directivity Gain
MDS	Multidimensional Scaling
FBS	Femtocell Base Station
pBS	Picocell Base Station
RV	Random Variable
WINNER	Wireless World Initiative New Radio
D2D	Device-to-Device
MTC	Machine-Type Communication
PGFL	Probability Generating Functional
CCDF	Complementary Cumulative Distribution Function
eMBB	enhanced Mobile Broadband
mMTC	massive Machine-Type Communication
URLLC	Ultra-Reliable Low Latency Communication
QoE	Quality of Experience
M-MIMO	Massive multiple input multiple output
AWGN	Additive White Gaussian noise
QoS	Quality of Service

Contents

Abstract	II
Acknowledgements	IV
Publications Related to the PhD Thesis	VII
Acronyms and Notations	IX
List of Figures	XVII
List of Tables	XXI
List of Algorithms	XXII
1 Introduction	1
1.1 Background	1
1.2 Literature Review and Motivation	9
1.2.1 Single and Multi-tier Small Cell Networks (SCN)	10
1.2.2 Ad-hoc Sensor Networks	13
1.3 Contributions of the Thesis	15
1.4 Thesis Structure	17
2 Single-Tier SCN Analysis	21
2.1 Introduction	21
2.2 System Model	22

2.2.1	Poisson point process (PPP) base-station (BS)s and Users . . .	23
2.2.2	Directional beamforming modelling	23
2.2.2.1	ESPAR configuration	24
2.2.3	Channel modelling	25
2.2.4	SINR modelling	26
2.3	Coverage Probability Analysis	26
2.4	Results	30
2.5	Summary	33
3	Multi Tier SCN Analysis	35
3.1	Introduction	36
3.2	System Model	37
3.2.1	Poisson Point Process (PPP) BSs and Users	37
3.2.2	Directional beamforming modelling	38
3.2.3	Small-Scale Fading	39
3.2.4	LOS BS and path-loss Model for mmWave links	40
3.2.5	SINR modelling:	41
3.2.5.1	μ Wave tiers	41
3.2.5.2	mmWave tier	41
3.3	Performance Analysis for μ Wave and mmWave tiers	42
3.3.1	Coverage Probabilities \mathcal{P}_μ^c and \mathcal{P}_w^c	42
3.3.1.1	μ Wave tier Coverage Probability \mathcal{P}_μ^c	42
3.3.1.1.1	Model Configuration	43
3.3.1.2	mmWave tier Coverage Probability \mathcal{P}_w^c	45
3.3.2	Average Rates R_μ and R_w	47
3.3.3	ASE and EE Analysis in terms of minimum rate model	47
3.3.3.1	ASE η and EE Ω Optimisation	47
3.3.3.1.1	μ Wave tier	49

3.3.3.1.2	mmWave tier	50
3.3.4	ASE and EE Analysis in terms of average rate under coverage	51
3.3.4.1	Average Rate under Coverage R^c	51
3.3.4.2	ASE η_μ^c and EE Ω_μ^c Analysis	55
3.4	Results	56
3.4.1	μ Wave tiers	60
3.4.1.1	Results for minimum rate model analysis	60
3.4.1.2	Results for average rate under coverage	60
3.4.2	mmWave tier	65
3.5	Summary	65
4	Wireless Ad-hoc Sensor Networks: Detection	67
4.1	Introduction	68
4.2	System Model	69
4.3	Performance Analysis	71
4.3.1	Detection Probability Analysis	71
4.3.2	S -localisability probability	74
4.4	Optimal density for S -localisability	75
4.5	Results	78
4.5.1	PPP Model	78
4.5.2	Fixed Model	81
4.6	Summary	83
5	Wireless Ad-hoc Sensor Networks: Localisation	85
5.1	Introduction	86
5.2	System Model	88
5.3	ToA localisation algorithms	89
5.3.1	LLS algorithm	89
5.3.2	Alternating Rank-based Euclidean distance matrices (EDM) algorithm	90

5.3.2.1	Definition and properties of EDM	90
5.4	TDoA localisation algorithms	96
5.4.1	LLS and WLS	96
5.4.2	SRD-LS algorithm	97
5.5	Results	99
5.5.1	ToA Algorithms	99
5.5.1.1	Localisation error plots versus varying the delay pa- rameter μ	101
5.5.1.2	CDF plots for random choice of sensors	101
5.5.2	TDoA Algorithms	102
5.5.2.1	Localisation error plots versus varying number of time slots	102
5.5.2.2	CDF plots for the localisation error	109
5.5.2.3	Localisation error plots versus varying number of sensors	109
5.5.2.4	CDF plots for urban and rural environments	109
5.5.2.5	Results using EM Terrano Software	111
5.6	Summary	114
6	Conclusions and Suggestions for Future Work	116
6.1	Conclusions	116
6.2	Suggestions for Future Work	120
6.2.1	Performance analysis of multi tier hybrid network using an inhomogeneous PPP	120
6.2.2	Soft-Decision Detection Analysis in Ad-hoc Sensor Networks .	120
6.2.3	Localisation analysis for Heterogeneous Sensor Networks. . .	120
6.2.4	Analysis of multiple target detection and localisation	121
A	Stochastic Geometry Background	122
A.1	Mathematical Preliminaries	123

Bibliography

127

List of Figures

1.1	Thesis overview	2
1.2	5G-network-architecture.	4
1.3	Different BSs used in different scenarios (Rural, Urban, etc.).	5
1.4	Heterogeneous Multi-tier Network.	6
1.5	Localisation in Sensor Networks.	8
2.1	System model consists of multiple femtocell base station (FBS)s, user terminal (UT)s, desired FBS and typical UT.	23
2.2	Sector beampatterns of the 7-element electronically steerable parasitic array receptor (ESPAR) [58].	30
2.3	The coverage probability $\mathbb{P}[\gamma > \gamma_{\text{th}}]$ for different SIR thresholds γ_{th} for Models 1 and 2.	31
2.4	The coverage probability $\mathbb{P}[\gamma > \gamma_{\text{th}}]$ for different SIR thresholds γ_{th} for Model 1 at different intensities λ_f	32
2.5	The coverage probability $\mathbb{P}[\gamma > \gamma_{\text{th}}]$ for different SIR thresholds γ_{th} for Model 2 at different intensities λ_f	32
3.1	A three-tier hybrid cellular HetNet using μ Wave links (wireless back-haul links) for the first two-tiers and mmWave links for the last tier	38
3.2	The coverage probability ($\mathcal{P}[SIR > \gamma_\mu]$) of μ Wave tiers for different SIR thresholds γ_μ for models 1 and 4.	57

3.3	The coverage probability ($\mathcal{P}[SIR > \gamma_\mu]$) of μ Wave tiers for different SIR thresholds γ_μ for models 2 and 3.	57
3.4	Average rate multiplied by Probability of Coverage ($R_\mu * P_\mu^c$) at different SIR threshold γ_μ for models 1 and 4.	59
3.5	Average rate multiplied by Probability of Coverage ($R_\mu * P_\mu^c$) at different SIR threshold γ_μ for models 2 and 3.	59
3.6	μ Wave link area spectral efficiency (ASE) η_μ for different SIR thresholds γ_μ	61
3.7	μ Wave link energy efficiency (EE) Ω_μ for different SIR thresholds γ_μ	61
3.8	μ Wave rate under coverage multiplied by Probability of Coverage ($R_\mu^c * P_\mu^c$) at different SIR threshold γ_μ	62
3.9	μ Wave tier ASE in terms of average rate under coverage for different SIR thresholds γ_μ	63
3.10	μ Wave tier EE in terms of average rate under coverage for different SIR thresholds γ_μ	63
3.11	mmWave tier ASE η_w for different signal-to-interference-plus-noise ratio (SINR) thresholds γ_w	64
3.12	mmWave tier EE Ω_w for different SINR thresholds γ_w	64
4.1	3-dimensional System Model MASNET with red cross as the typical target node, blue and black circles are sensors and "active" sensors, respectively.	69
4.2	The probability of detection P_d with respect to the intensity of the PPP of the sensors λ_s at different false alarm probabilities and different transmit power $\mathbb{E}[a^2]$	79
4.3	The probability of detection P_d with respect to the false alarm probability p_f at different intensities λ_s . Markers are the simulation results and the lines are the analytical results.	79

4.4	The S -localisability probability P_L^S with respect to the intensity of the PPP of the sensors λ_s	80
4.5	The minimal S -localisability probability $P_{L_{\min}}^S$ with respect to intensity of the PPP of the sensors λ_s	81
4.6	The probability of detection P_d with respect to the false alarm probability p_f at different intensities λ_s	82
5.1	2-D top view of System model in Chapter 4 for the two scenarios mixed (left) and separated (right).	86
5.2	Estimated pairwise distances is illustrated with one distance missing [90].	92
5.3	Localisation error vs μ for the two scenarios: separated (top) and mixed (bottom), with different number of sensors ($N_s = 4, 10$). The solid lines are for the ten sensors and the dotted lines are for two different picks of four sensors.	100
5.4	cumulative distribution function (CDF) plot for the random choice of four sensors from the ten sensors for the mixed (top) and separated (bottom) scenarios with high delays $\mu = -7$	103
5.5	Localisation error vs. varying numbers of time slots for three localisation algorithms for the mixed (top) and separated (bottom) scenarios.	104
5.6	CDF plots for the localisation error for $t = 1$ for the mixed (top) and separated (bottom) scenarios.	105
5.7	CDF plots for the localisation error for $t = 10$ for the mixed (top) and separated (bottom) scenarios.	106
5.8	CDF plots for the localisation error for $t = 50$ for the mixed (top) and separated (bottom) scenarios.	107
5.9	Localisation error vs different number of sensors for $t = \{10, 30, 50\}$ for the mixed (top) and separated (bottom) scenarios.	108

5.10	CDF plots for the localisation error for $t = \{1, 5, 10\}$ using squared-range-difference-based least squares (SRD-LS) for mixed (top) and separated (bottom) rural environments.	110
5.11	CDF plots for the localisation error for $t = \{1, 5, 10\}$ using SRD-LS for mixed (top) and separated (bottom) urban environments	112
5.12	Sensor nodes, actual and estimated target locations using EM Terrano measurements for a mixed scenario ($P_T = -23$ dB).	113
5.13	Sensor nodes, actual and estimated target locations using EM Terrano measurements for a separated scenario ($P_T = -23$ dB).	113

List of Tables

1.1	Comparison for Different Range-based localisation techniques [72]	12
2.1	Modelling Notations	25
2.2	Antenna configurations for different models.	27
3.1	Modelling Notations	40
3.2	Antenna configurations for different models.	43
3.3	The values for parameters used in simulation and analytical results [5, 77].	56
4.1	Summary of Notations	70
4.2	The values for parameters used in simulation and analytical results.	78
4.3	The optimal intensities λ_S^*	81
5.1	Notations and Definitions	87

List of Algorithms

1	Alternating Rank Based EDM Algorithm [90]	91
2	SRD-LS Algorithm [52]	99

Chapter 1

Introduction

Fig. 1.1 gives a brief overview of the thesis and its main contents. We analyse the performance of 5G wireless communication networks namely HetNet cellular networks and sensor networks using the tools of stochastic geometry. Initially, we consider the coverage probability analysis of a single-tier cellular network exploiting directional antenna at the receiver end. Furthermore, we examine the performance analysis of a multi-tier HetNet cellular network deploying directional antennas in terms of coverage probability, ASE and EE for the minimum rate model and average rate under coverage model. Since 5G communication also supports localisation, we consider homogeneous sensor networks in a 3-d space where we analyse the performance with respect to detection probability; which can be observed similar to the coverage probability; and S -Localizability probability i.e. the probability that at least S sensors may successfully participate in localisation procedure. Finally, based on the results from the analysis of the sensor networks, we present a comparison between conventional range-based localisation algorithms in terms of the minimum number of sensors required.

1.1 Background

As we approach 2020, it is expected that the number of connected devices will be more than 50 billion. Moreover, we will be surrounded by the Internet-of-Things

(IoT), for example we will have connections between our home appliances and our cars. 5G is being designed and built taking this into consideration [1]. The first goal of 5G is eMBB and the performance measures associated with it are high peak throughput, high spectral efficiency, high capacity and mobility. The second goal is mMTC which aims at achieving ubiquitous coverage, high network and device energy efficiency and a massive number of connections [2]. The final goal of 5G is URLLC that leads to extremely high reliability and extremely low latency. Furthermore, privacy and security are also key considerations in 5G and future generations as well as battery life which is a fundamental facet of mobile connectivity.

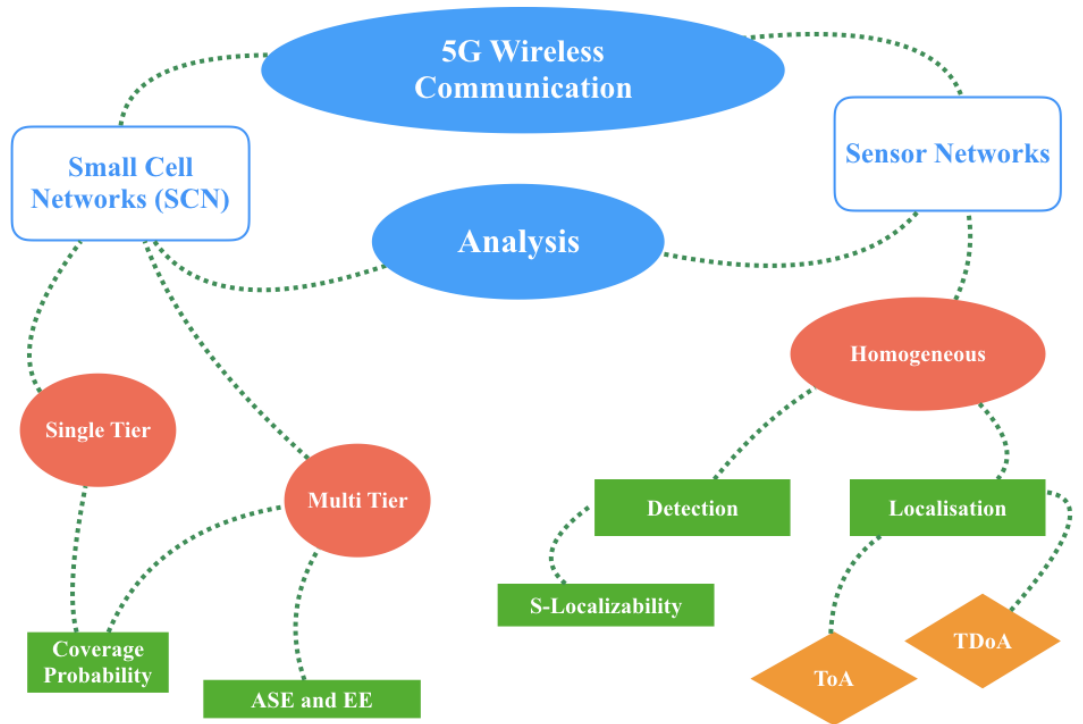


Figure 1.1 Thesis overview

More precisely, 5G standards are expected to have these eight advanced features [3] :

- 1 – 10 Gbps connections to endpoints in the field,
- 1-millisecond latency,
- 1000x bandwidth per unit area,
- 10 – 100x number of connected devices,
- 99.999% availability,
- 100% coverage,
- 90% reduction of network energy usage,
- up to ten years of battery life for low power devices.

To attain these performance requirements, numerous technologies [4] are applied to 5G systems, such as small cell multi-tier (Heterogeneous Networks (HetNet)) [5,6], massive multiple input multiple output (M-MIMO) [7,8], millimetre wave (mmWave) communications [9] and device-to-device (D2D) communications [10].

The three key areas that have been investigated for the research of 5G mobile networks (Fig. 1.2) are

- **Millimetre Wave [9]:** For 5G, frequencies above 50 GHz are being examined. This presents challenges with respect to technology, circuit design and the operation of the system because these frequencies are almost entirely absorbed by obstacles such as buildings and foliage.
- **massive Multiple-Input Multiple-Output (MIMO) [7]:** Although MIMO is exploited in plenty of applications from LTE to Wi-Fi, etc., the number of antennas is relatively limited. For 5G, there is a high possibility of deploying a large number of antennas on single user equipment due to antenna sizes and spacings with respect to the wavelength.

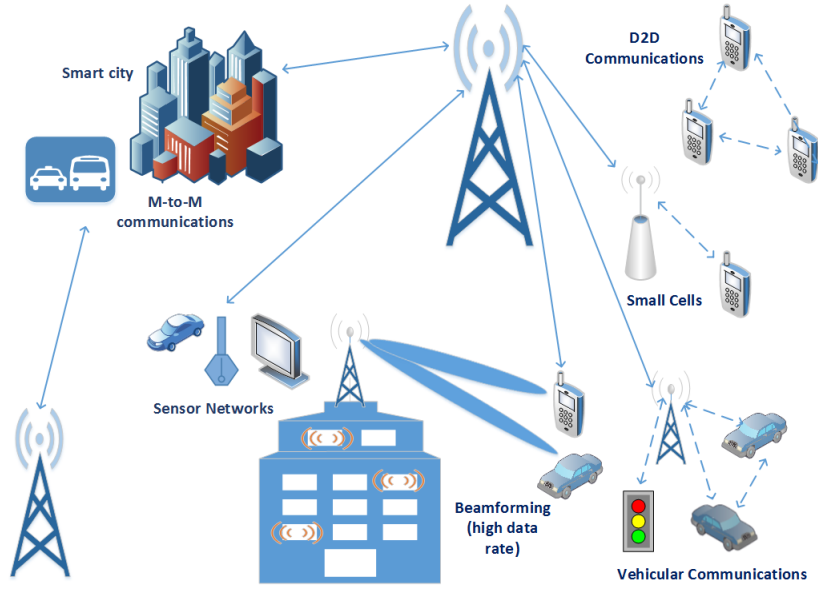


Figure 1.2 5G-network-architecture.

- **Small Cell Networks (SCN)** [6,11]: Decreasing the size of cells provides an effective usage of the available spectrum. The small cell size in the macrocell network; deploying femtocells or picocells, accomodates different techniques to ensure that all small cells can operate adequately as needed.

One of the advanced features for 5G is 100% coverage, one solution to achieve this feature is multi-tier SCN (HetNet) and a more advanced solution is a hybrid network that consists of microwave (μ Wave) and mmWave links which will be discussed in more details in Chapter 3.

First of all, small cell is a term used for low-cost and low-power radio access nodes that have a limited range of several hundred meters as shown in Fig. 1.3. SCNs such as femtocells and picocells [12–14], are considered a promising solution to enhance the system coverage and the smaller size of the network provides high spectrum efficiency by reusing spatial resources. Moreover, these networks increase the data capacity and decrease the overall cost by helping the service providers to eliminate expensive installation and rental costs. Hence, these networks help in improving the overall performance of the network. A simple example is if a user is closer to a small cell BS, it transmits at lower power levels, which effectively lowers the power out of the user terminal.

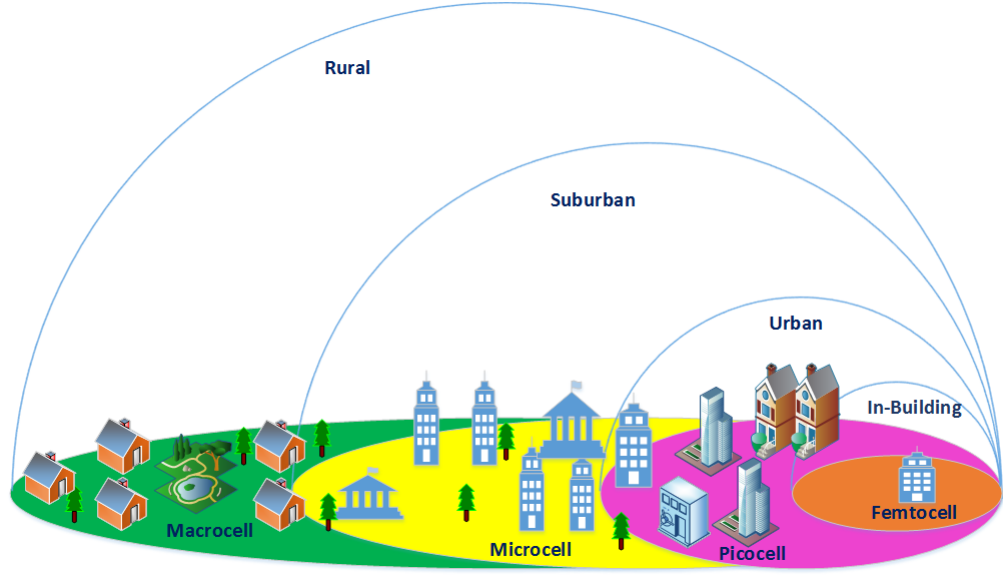


Figure 1.3 Different BSs used in different scenarios (Rural, Urban, etc.).

Recently, more work has been done to overlay these SCN on top of the macrocell networks that are already being used for a decent amount of time. Incorporating a layered structure of macrocells, femtocells, and/or picocells is referred to HetNets (see Fig. 1.4). They are utilised to offer improved wireless coverage in numerous scenarios ranging from open outdoor environments to homes, office buildings and underground areas. Apart from improved coverage, there are several benefits to HetNets as opposed to traditional homogeneous wireless networks including improved spectrum efficiency and increased reliability [5, 15–20]. Not only the coverage and reliability improve because the BSs in one tier can fill the coverage holes of other tiers and maintain a connection, but also spectral efficiency is enhanced due to better load balancing of users across BSs from different tiers.

We observe in Fig. 1.4, that HetNet supports cellular and D2D modes. D2D refers to direct communication between two user terminals without traversing the BS. Nowadays, the number of mobile UTs is rapidly increasing which could potentially enhance direct communications, especially for high data rate services. Hence, D2D communications in such scenarios can greatly increase the spectral efficiency of the network.

The advantages of D2D communications go beyond spectral efficiency; they can potentially improve throughput, energy efficiency, delay, and fairness [21].

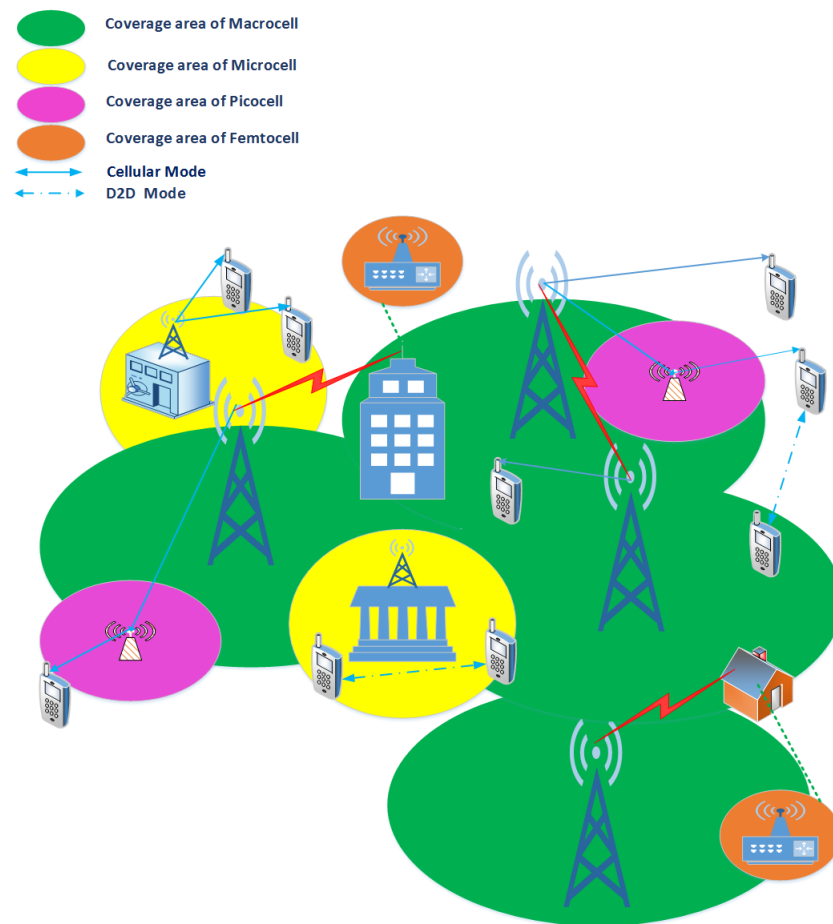


Figure 1.4 Heterogeneous Multi-tier Network.

Therefore, 5G standards are expected to support D2D communication as shown in Fig. 1.4. Apart from the expected accomplishments related to communications for 5G networks, 5G will also support network-based localisation in 3-dimensional space, with $1\text{ m} < \text{accuracy} < 10\text{ m}$ on 80% of the time and for indoors accuracy $< 1\text{ m}$ [22]. Relying on such meticulous location information, the first generation to benefit from localisation in wireless networks design and optimisation would be 5G [23].

Moreover, 5G supports machine-type communication (MTC), wireless sensor network (WSN) is an example of MTC as shown in Fig. 1.2. In the WSN, sensors are set up for metering (e.g., energy, gas, and water) in rural, suburban and urban areas, lights management of building or city, vehicle traffic control, environment monitoring (e.g., temperature, pollution, humidity, and noise) and localisation [22, 24–31].

To support MTC, several requirements should be met by 5G networks, such as higher data rate, higher quality of experience (QoE) for users, lower energy consumption and lower end-to-end latency. Furthermore, 5G network topology is expected to shift from base station centric to a device-centric network, because 5G requirement is sub-millisecond latency and to avoid the bandwidth limitations in the traditional wireless spectrum. These device-centric networks are referred to wireless ad-hoc networks which can be classified into Vehicular Ad hoc Networks (VANETs) [32, 33], Mobile Ad hoc Networks (MANETs) [34, 35], Smartphone Ad hoc Networks (SPANs) [36], Wireless mesh networks [37] and so on. These are networks with no pre-existing infrastructure and easy to install.

Because of the advantages of wireless ad-hoc and sensor networks, wireless ad-hoc sensor networks are introduced and deployed in various applications [25, 38–40]. In [39], an efficient sensor network composed of low power sensor modules was developed and implemented for biomedical applications. In [38], a sensor network based on ad-hoc technology was implemented for agriculture applications and an information platform.

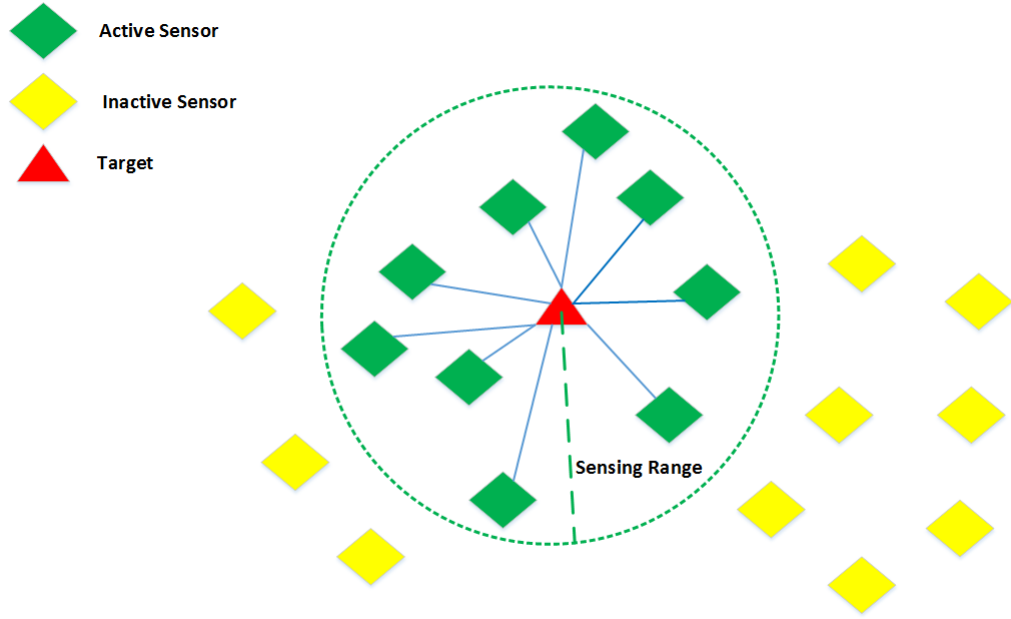


Figure 1.5 Localisation in Sensor Networks.

Localisation (also called positioning) is a crucial issue in cellular and WSN applications and deeply embedded in our daily lives [25, 27, 29, 38–43]. It has been studied for many years in various applications such as locating 911 calls, WiFi, GPS navigations, etc [22, 30, 31, 44–46]. In cellular networks, the driving force behind localisation research is to enable the location-based application services within certain accuracy requirements [22]. In [30], 5G-based localisation assisted driving applications are studied and provide centimetre-accurate positioning by optimising the network design in a highway scenario. In [31], the radio signals have been used for position tracking, as well as the reconstruction of a 3-D map of the surrounding environment, which is useful to assist people with impaired vision. In wireless ad-hoc networks, localisation has a wide aspect as many real-life applications such as improving network connectivity in an urban area, rescue operations and battlefields. In these scenarios, the most common assumption is having a predefined sensing range and only the nodes within this range are defined as "active" nodes, which refer to the nodes that detected the target's transmitted signal (Fig. 1.5). Thus, only these nodes are deployed to locate the target node.

Localisation techniques can be classified into two categories viz. range based and range free. Range-based techniques rely on distance measurements such as received

signal strength (RSS) [47], angle of arrival (AoA) [48, 49], time of arrival (ToA) [50], and time-difference of arrival (TDoA) [51, 52].

A comparison between the aforementioned techniques is summarised in Table 1.1. For ToA, usually, multi-lateration approaches are used such as linear least squares (LLS) [26] and weighted least squares (WLS) [53]. With some modifications, these techniques are commonly used for TDoA algorithms, as well as squared-range-difference-based least squares (SRD-LS) [52]. All these algorithms will be discussed in detail in Chapter 5. Based on the topology, localisation can also be divided into two approaches viz. centralised and distributed. In the centralised approach, sensors forward the information to the fusion centre (FC) or the cluster head (CH), which combines the local decisions to yield a decision about the target. This structure can be considered suboptimal when there is a communication outage between some of the sensors and the FC. Thus, the FC does not have enough information to localize the target. However, in the distributed approach, each sensor can perform the localisation on its own, but this approach would have a higher cost because it requires the use of expensive and smart sensors that are able to do the analysis [54].

To summarise, we exempted a short background for the 5G wireless network architecture. We pointed out two main networks which are SCN cellular and wireless ad-hoc sensor networks. In Section 1.2, we present the related work in literature for these networks and the motivation of this thesis.

1.2 Literature Review and Motivation

Randomness is an inherent property of network topologies, not only for ad-hoc sensor networks, but also for SCN cellular ones, and could occur due to communication outage, node failure, blockage or mobility of the communication nodes. One of the tools that enable analysis of such random networks is stochastic geometry, which is a mathematical research area that provides suitable mathematical models and statistical methods to study and analyse random spatial patterns, where its main subfield is point process theory [55–57]. Some basic stochastic mathematical preliminaries, that are being used throughout the thesis, are stated in Appendix A in details with

the theorems' proofs.

1.2.1 Single and Multi-tier SCN

In the first part of the thesis, we concentrate on the analysis of single and multi-tier SCN. In SCN literature, a key result from single and multi tier SCN analysis is the derivation of the SINR distribution, using the stochastic geometry tools, which is then mapped to the coverage probability [5, 16, 58]. A favourable property of HetNets was shown in [19, 20], which declared that the distribution of the SINR is invariant to the network density, as long as all tiers have the same threshold. Thus, deploying more BSs would result in increasing the ASE of the HetNet. This demonstrates that more users can be supported by the network with a higher spatial reuse efficiency. However, the dense and random deployment of small cells raised questions about the EE implications. To this end in [18], active/sleep (on/off) modes were introduced for BSs, leading to improved EE. Another solution based on the joint maximisation of EE and spectral efficiency while ensuring proportional rate fairness among users and taking into account the backhaul capacity constraint was analysed in [8].

The improvement of spectrum efficiency and network capacity for homogeneous and HetNet is at the expense of the increased interference. In SCN with frequency reuse and several coexisting tiers, there are two types of interferences, namely, the co-tier and the cross-tier interference. Co-tier interference is the interference of the same tier, such as interference between users of the same tier. While cross-tier interference refers to the interference between the users of two different network tiers such as the FBS and macro base station (MBS).

Thus, interference mitigation and modelling is an area of primary interest to both industry and academic communities. First, we consider the interference mitigation and then we state how stochastic geometry tools are equipped to model the interference. When traditional omni-directional antennas are deployed in SCN, the mitigation of the interference is achieved by resource allocation [59, 60] and power control [61, 62]. But the system complexity increases significantly due to the need for co-operation across femtocells and/or message exchange. To achieve interference

mitigation while maintaining minimum cost and complexity, the directional antennas have been considered for femtocells [58, 63–66]. The switched multi-element antenna has been suggested to be deployed at the FBSs, where one beam pattern or combination of more is selected dynamically from predefined ones to the serving UT [63–66]. The exploitation of directional antennas in single tier SCN at the UT increases the received SINR, thereby enhancing the system capacity [58]. However, the results in [58] were achieved experimentally and we extended this work in Chapter 2 using the tools of stochastic geometry to obtain a closed-form expression for the coverage probability and the corresponding numerical results. There are several methods used to reduce the interference for multi-tier HetNet as presented in [67–69], but the required additional infrastructure leads to increased expenditure.

Stochastic geometry tools are used to model the interference, for example when the nodes are scattered randomly in a certain region following a PPP Φ with density λ . Based on this assumption some of the well-known theorems such as Campbell-Mecke (sum over PPPs) and probability generating functional (PGFL) (product over PPPs) are exploited to find a closed-form expressions for the performance metrics such as coverage probability, success probability, outage probability, ASE and EE. For instance, in [70], heterogeneous networks consisting of macrocell and femtocells were considered and the tools of stochastic geometry were used to derive the general expressions of the success probability.

The performance of two-tier SCN was analysed and a closed-form expression for the outage probability was derived in [71] using an approximation for the interference distribution.

Other performance metrics such as coverage probability, ASE and EE were analysed using the tools of stochastic geometry, mainly point process theory [5, 16–20]. For example, a flexible and tractable model for a downlink HetNet consisting of K tiers was presented in [5]. They assumed that the mobile user associates to the strongest BS and they derived the probability of coverage as well as the average rate under coverage achieved by a randomly located mobile user. In [17], a multichannel HetNet was considered and they developed a framework for the uplink ASE analysis

Table 1.1 Comparison for Different Range-based localisation techniques [72]

Technique	Advantage	Disadvantage
RSS	Easy to implement, cost-efficient, can be combined with other techniques	Suffers from multi-path fading and environmental noise, low localisation accuracy
AoA	Can provide high localisation accuracy	Might require directional antenna and complex hardware, performance deteriorates as the distance between target and sensor nodes increases, requires complex algorithms comparatively
ToA	Provides high localisation accuracy	Require time synchronisation between target and sensor nodes, LOS is mandatory for accurate performance
TDoA	Does not require synchronisation between target and sensor nodes	Requires synchronisation between the sensor nodes, requires larger bandwidth

exploiting a biased cell association scheme with channel inversion power control to lessen the interference and coordinated sub-channel allocation. The success probability and EE were derived for homogeneous single-tier and heterogeneous K -tier wireless networks under different sleeping policies [18]. Furthermore, they showed the utilisation of small cells generally leads to higher EE, however, this gain saturates as the density of small cells increases.

While [16–20] focused on μ Wave HetNets, mmWave communication has emerged as a key enabler for higher spectral efficiency and EE in the 5G wireless communication networks. Unlike μ Wave, they operate at 10 to 300 GHz frequency bands with available bandwidths of 2 GHz or more [73–78]. A general framework to evaluate coverage and a tractable model for rate performance was proposed in [76, 77], where it was shown that dense mmWave networks can achieve comparable coverage and much higher data rates than conventional ultra-high frequency (UHF) cellular systems, despite the presence of blockages.

Recently, because of the advantages of μ Wave and mmWave communications, hybrid networks consisting of a HetNet with μ Wave and mmWave tiers were introduced [7, 79, 80]. In [79], the performance in terms of coverage and rate of hybrid

cellular networks consisting of BSs operating at mmWave and sub 6 GHz bands was investigated. The results showed that the hybrid network achieved an average rate under coverage which is comparable to that of a mmWave network and much higher than the stand-alone UHF network. In [7], the downlink performance in terms of coverage and rate of a three-tier hybrid network where M-MIMO macro base stations (MBSs) are overlaid with small cells operating at either sub 6 GHz or mmWave bands was presented and the users were assumed to connect to any of the tiers according to the association probability. It was observed that the implementation of M-MIMO on macro tier and deployment of high density of mmWave small cells led to the enhancement of rate and coverage. A similar system model was presented in [80], but the MBSs were not equipped with M-MIMO, and the effects of BS density on ASE and EE were studied. Based on the analysis, introducing mmWave small cells considerably improved coverage and hence ASE, and EE. This motivated us to extend the coverage analysis of single-tier SCN to the performance analysis of a hybrid multi-tier HetNet using the stochastic geometry tools in terms of coverage probability, ASE and EE in Chapter 3.

1.2.2 Ad-hoc Sensor Networks

In Chapters 4 and 5, we focus on wireless ad-hoc sensor networks specifically detection and localisation analysis. As stated in Section 1.1, ad-hoc sensor networks are a crucial part of the 5G network architecture. One of the interesting topics in ad-hoc sensor networks is localisation which is useful for various applications such as disaster recovery, rescue operation, military communication, environmental monitoring, asset tracking in warehouses, people with impaired vision (WSNs), locating 911 calls and assisted driving (cellular networks).

A very trivial solution for providing accurate location information in the aforementioned networks is the global navigation satellite systems (GNSS), e.g., GPS. However, such systems are not always reliable and available. Furthermore, this solution is not very efficient especially in WSN which often consists of a large number of sensor nodes, implying that this solution is not economically viable and costly

to equip all nodes with GNSS receivers. As an alternative, other localisation approaches are used based on sensor nodes (anchors) measurements to locate the target node (node to be localised). These approaches can also be equipped in cellular networks, where the BSs are considered the sensor nodes and the user is the node to be located. We should note that for the cellular network, the communication between BS and the desired user is considered successful when less interference is available from other BSs. But in a localisation problem, the main objective is to make sure that the user to be located can receive signals from a sufficient number of BSs which is referred to as the hearability problem [81–83].

Since localisation performance fundamentally depends upon the number of participating nodes and the accuracy of the measurements. In literature, if these aforementioned factors are considered deterministic, the localisation performance is analysed using the Cramer-Rao lower bound (CRLB) for a specific topology of the nodes [84–86]. Recently, it has been shown in cellular networks that none of the aforementioned factors can be considered deterministic [81–83]. In [81], a new tractable approach for analysing localisation performance was developed using the tools from stochastic geometry to obtain easy-to-use expressions for the base station (BS) hearability, with and without base station coordination. Moreover, an improvement in the device localisability through the collaboration among BSs was investigated in [83].

When discussing localisation for wireless ad-hoc sensor networks, the studies differ from the cellular scenario. Because in ad-hoc sensor networks literature almost certainly ignores the interference and propagation effects, instead the coverage (detection) probability is defined using some fixed detection range [87]. A novel three-dimensional localisation algorithm was proposed in [88], that improves the accuracy of node localisation and reduces the impact of positioning error by decreasing the communication radius and increasing the density of sensor nodes (anchors). However, as shown in Fig. 1.5, this approach assumes that all the sensor nodes inside the detection range are "active" and participating in the localisation. This is not an accurate assumption, because the sensor nodes within this fixed detection range

might experience a communication outage, blockage or sensor node failure. This results in a random number of active nodes, not deterministic, which confirms the work conducted in cellular localisation literature.

To this end, our work in Chapters 4 and 5 is related to the localisation problem in 3-D MASNET (a class of WSN) which is divided into two steps. The first step is the detection analysis using the stochastic geometry tools for the minimum number of nodes required for successful localisation under the effect of path-loss and small scale fading (Chapter 4). The second step is to analyse and compare between the conventional range based ToA and TDoA localisation algorithms in terms of the effect of the minimum number of sensor nodes participating in the localisation procedure (Chapter 5).

1.3 Contributions of the Thesis

The contributions of this thesis are summarised as follows:

- In Chapter 2, we present a performance analysis of a single-tier femtocell network with directional and omni-directional antennas at the UT. We show the impact of the usage of directional antennas to mitigate interference and increase SIR. The SIR is then mapped to the coverage probability, which is used to analyse the performance of the considered network, using a simplified mathematical model. This model provides an approximate distribution for femtocell signal to co-channel interference ratio by approximating the number of interfering FBSs to a binomial distribution. This analysis shows that using a directional antenna at the receiver end improves the coverage performance of the network. This framework can be used for an indoor scenario as well by taking into account the wall penetration losses [11].
- In Chapter 3, we extend this model into multi-tier and also study the effect of adding the directional antenna at both transmitter and receiver ends. This model is a downlink three-tier hybrid cellular HetNet using μ Wave links for the first two tiers and mmWave links for the last tier. We examine the impact of

the usage of directional antennas for the wireless backhaul network and analyse the performance of the considered network in terms of coverage probability, ASE and EE using the conventional minimum rate model.

We formulate an optimisation problem to find the optimal SIR threshold that maximises the ASE and EE for the entire network. Our system model enables us to separate this problem into two independent subproblems corresponding to μ Wave backhaul link and mmWave user links, respectively. We show that the ASE and EE optimisation problems of the wireless backhaul HetNet results in an optimum solution that is only dependent on the path-loss exponent of the μ Wave network. Unfortunately, the optimisation problem for mmWave communications is not analytically tractable. Therefore, the optimal SIR threshold is evaluated numerically and an analytical plot for the ASE of the mmWave link with respect to different SIR thresholds is presented. For both subproblems, we use Monte-Carlo simulations to demonstrate the proximity of our analytical results with the experimental ones.

We also analyse the ASE and EE for the μ Wave link considering the average rate under coverage. The average rate under coverage refers to the average rate achieved by the picocells conditioned that they are covered, i.e., the received SIR is greater than a predefined threshold. This metric is greater than the minimum rate and closer to the rate observed in practical deployments. Moreover, we will show that using the average rate under coverage, ASE and EE will be strictly decreasing functions and are maximised by choosing the lowest possible SIR threshold in the system. Furthermore, since we use μ Wave link as the wireless backhaul, we analyse its average rate under coverage separately in order to determine its suitability as a reliable wireless backhaul [6].

- In Chapter 4, we present a tractable stochastic geometric approach to perform the analysis of ad-hoc sensor networks in 3-dimensional space. We examine not only the path-loss effect but also the small scale fading. We analyse the performance of the considered network in terms of detection and S -localisability probabilities. The S -localisability probability P_L^S is defined as the probability

that at least S sensors may successfully participate in the localisation procedure. We formulate an optimisation problem to find the optimal density of sensors λ_s that maximises the minimal S -localisability probability for the considered network. Furthermore, we compare between the PPP model and a fixed model, where the number of nodes is fixed with random locations. The experimental results of both models are close, however, the analytical results for the fixed model are computationally intensive which is another benefit of using the tools of stochastic geometry [89].

- In Chapter 5, we present an analysis of the localisation error with respect to the number of active nodes participating in the localisation procedure. Specifically, we consider range based localisation techniques that rely on distance measurements between nodes based on ToA and TDoA. For ToA, we present an alternating rank-based EDM algorithm and compare its results with the conventional LLS (multi-lateration) approach. For TDoA, we compare between the performance of LLS, WLS and SRD-LS [42].

1.4 Thesis Structure

This thesis consists of six chapters. Specifically, each chapter is organised as follows.

In Chapter 2, a downlink femtocell network is considered which consists of FBSs and UTs. Both FBSs and UTs are modelled as independent PPP. We derive a closed-form expression for the coverage probability by using a simplified mathematical model introduced in [71]. This model provides an approximate distribution for the femtocell signal to the co-channel interference ratio by approximating the number of strong interfering FBSs to a binomial distribution. We compare between Model 1 and Model 2, wherein Model 1, we assume both FBS and UT are equipped with omni-directional antenna. However, in Model 2, we assume the UT is equipped with a directional antenna which helps in the mitigation of interference. Finally, the simulated and the analytical closed-form of the coverage probability are compared for various intensities of the PPP of the proposed femtocell networks and we show

that considerable improvement can be achieved when a directional antenna is deployed at the UT (Model 2).

In Chapter 3, a three-tier hybrid cellular HetNet is considered using μ Wave links for the first two tiers and mmWave links for the last tier. The two-tiers with μ Wave links form a wireless backhaul to the last tier with mmWave links. The main challenge in having a wireless backhaul is to suppress interference. Thus, we propose a novel and practical model where we can reuse the μ Wave infrastructure, but equip the BSs with directional antennas to have a robust wireless backhaul network. To solve the bottleneck rate problem, we assume that the rate required by the mmWave users is comparable to that offered by the μ Wave links. Different configurations based on the placement of the directional antennas at each tier are explored. The analysis of the key performance indicators, namely, the coverage probability, area spectral efficiency, and energy efficiency using the conventional minimum rate model, and the simulation results associated with these parameters are presented. In order to analyse this hybrid network with a wireless backhaul, an optimisation problem for the overall ASE and EE with respect to the optimal acsir threshold required for μ Wave and mmWave links is investigated. Results indicate that the optimal SIR threshold required for the μ Wave tiers (wireless backhaul) depends only on the path-loss exponent and that for the mmWave tier depends on the area of LOS region. Finally, instead of the conventional minimum rate model, we consider the average rate under coverage and show that the ASE and EE are strictly decreasing functions with respect to the threshold, thereby concluding that they can be maximised by choosing the lowest possible SIR threshold available in the system.

In Chapter 4, a three-dimensional ad-hoc sensor network consists of a large number of inexpensive sensor nodes distributed over a large region. The considered network is typically used for target detection and localisation to provide a greater level of situational awareness for units in the operational region. Although the number of sensors might be fixed, yet due to communication outage or node failure, the actual number of participating sensors in localisation is random, which

makes the localisation analysis intractable. Therefore, in this chapter, we propose a tractable model to analyse the localisation performance metrics such as detection probability and S -localisability probability. S -localisability probability is defined as the probability that at least S sensor nodes participate in the localisation procedure, successfully. Using the tools of stochastic geometry, we derive closed-form and easy-to-use expressions for these metrics, which agree with the simulations. Further, to optimise the localisation process, we obtain the density of sensors to maximise the minimal S -localisability probability. This density can be used as a lower bound for the minimum number of sensor nodes required for higher \mathcal{P}_L^S . Finally, considering a practical fixed model for MASNET, we demonstrate that the performance metrics have the same behaviour as the derived expressions using stochastic geometry. Moreover, we observe that obtaining the performance metrics for the fixed model is computationally intensive, thereby concluding the benefit of the derived expressions in the practical sense.

In Chapter 5, we analyse the effect of the number of sensors on the non-cooperative target node localisation for ToA and TDoA. This work examines the target localisation using a centralised range based approach. For ToA, we consider a search and rescue scenario, this work leverages an algorithm based on a class of matrix structure called EDMs for the specific purpose of improving localisation performance when the fusion centre (FC) cannot receive certain sensors' information due to fading or shadowing, etc. While this interesting approach to the problem of localisation has been found to be successful, it is also shown at high delay values the presented alternating rank-based EDM algorithm [90] outperforms the conventional LLS based algorithm for the minimum number of sensors. The localisation error decreases when the conditioning of EDM is better, i.e., when the sensors are further apart from each other and closer to the target. When no clock synchronisation is available between the target and sensor nodes, then the TDoA range based is a better approach. We extend the LLS algorithm [26, 91] to TDoA. The LLS performance is compared with WLS [53], and SRD-LS [52]. Although the LLS algorithm is known to be of low complexity, its main disadvantage is that its performance is sensitive to the outliers.

Thus, in order to have a better performance, outliers must be identified and their effect should be minimised. Once the outliers are identified, WLS can be used such that the outliers have smaller weights and hence have minimum impact on the final result. In general, the performance of WLS is dependent on the choice of weights. However, it has been shown in [52] that SRD-LS demonstrates the best performance with respect to finding the estimated target node position. SRD-LS uses a different approach than multi-lateration to estimate the target node location. The approach is based on the minimisation of the least squares (LS) criterion. The results show that the localisation error can be minimised if the sensors are scattered enough and are not too far from the sensors.

Finally, Chapter 6 states the overall conclusions for the thesis and proposes various ideas for future work and Appendix A summarises the mathematical preliminaries used in the main chapters with more details.

Chapter 2

Single-Tier SCN Analysis

In this chapter, we analyze the single-tier SCN in terms of coverage probability under the impact of the usage of directional antennas to the UTs. We analyze the performance of the considered network in terms of coverage probability, using a simplified mathematical model. This model provides an approximate distribution for femtocell signal to co-channel interference ratio by approximating the number of strong interfering FBSs to a binomial distribution. The results show a considerable improvement in the coverage probability when exploiting directional antennas. As the density of PPP increases, the coverage probability decreases due to the increase of the interference. However, the results show that this degradation decreases when exploiting directional antennas [11].

2.1 Introduction

As stated in Section 1.1 in Chapter 1, SCN such as femtocells and picocells, are considered a promising solution to improve coverage. The small cells size of femtocell and picocell not only provides high spectrum efficiency by using spatial reuse of resources, but also decreases the transmission range and hence results in higher probability of connectivity [92]. Furthermore, the key advantage of SCN (femtocell and picocell) is the minimum required upfront cost to the service provider. However, the main disadvantage of SCN is the interference vulnerability which is caused by

aggressive frequency reuse, dense deployment and cell-size reduction.

To this end, this chapter analyses the coverage performance of downlink single-tier SCN, where we use sectorized directional antennas for the reception at the UT. The FBSs are assumed to be distributed as a homogenous spatial Poisson point process (SPPP) and each FBS is equipped with an omni-directional antenna. Please note that this analysis is applicable to any sectorized directional antenna but we compare the analytical results with the simulation results by using an ESPAR antenna. The ESPAR antenna uses only a single radio frequency (RF) chain surrounded by passive elements to form electronic beam patterns. Thus, it is practical to fulfil the requirements of wireless user terminals constrained by low-cost, low-power and small-size [58]. Considering our presented system model, we derive a closed-form formula for coverage probability by using a simplified mathematical model [71]. This model provides an approximate femtocell co-channel interference distribution by approximating the number of FBS to a binomial distribution by considering only the strong interfering FBSs. The strong interferers are defined within a specified distance R from the typical user. Moreover, because the UT is equipped with a sectorized directional antenna which forms receiver beam patterns that divide the receiving angular space into several sectors. We add one more constraint for choosing the strong interferers, i.e. the FBSs whose angles of arrival (AoA) to the UT lie within the desired and neighbouring sectors. Hence, the usage of directional antenna plays a role in the mitigation of interference. Finally, the simulated and the analytical closed-form of the coverage probability performance are compared for various intensities of the PPP of the proposed femtocell networks and we show that considerable improvement can be achieved when a sectorized directional antenna is deployed at the UT.

2.2 System Model

In this section, we define our system model for the coverage analysis of the single-tier SCN. The system model is shown in Fig. 2.1, which consists of the typical UT communicating with the desired FBS whose location is fixed and known. The other interfering FBS are randomly located and the total area is divided into sec-

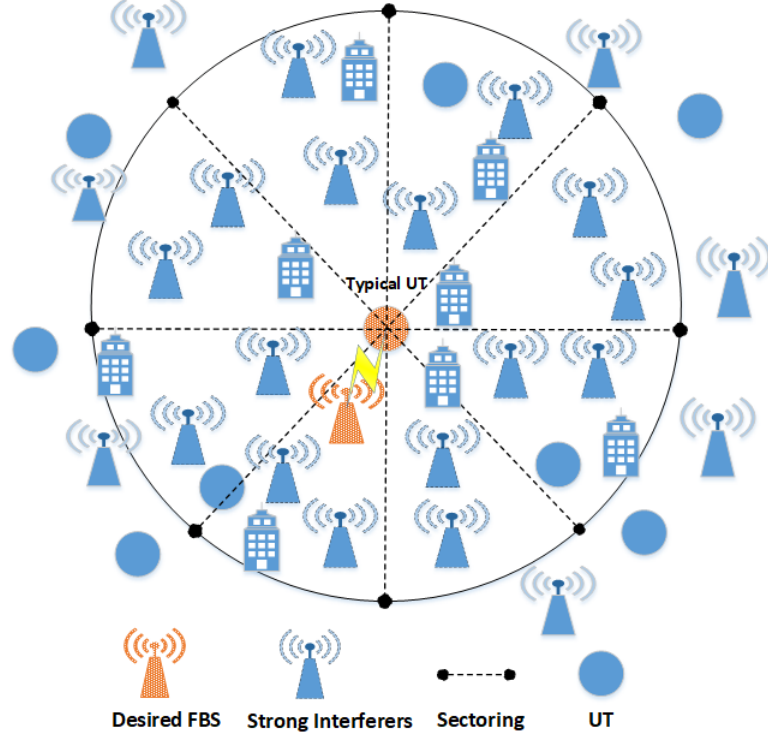


Figure 2.1 System model consists of multiple FBSs, UTs, desired FBS and typical UT.

tors according to the sectored directional antenna located at the typical UT. The interfering FBSs are considered strong interferers when they are located within a certain distance from the typical UT. The detailed mathematical formulation and underlying assumptions are discussed in the following subsections.

2.2.1 PPP BSs and Users

The considered network is a downlink scenario, it consists of FBSs and UTs, which are both modelled as an independent PPP Φ_k with density λ_k , where $k \in \{f, u\}$ indicating FBSs and UTs, respectively.

2.2.2 Directional beamforming modelling

For each UT, a directional antenna is approximated by a sectored antenna model which renders the analysis tractable [76]. In the sectored antenna model, antenna gains are assumed to be constant M for all angles within the beamwidth of the main lobe, and another constant S otherwise. The beampatterns of directional antenna

are formed to divide the whole angular space into several sectors.

Mathematically, the antenna gain (transmit/ receive) is given as

$$G_{T/R}(\theta) = \begin{cases} M_{T/R} & \text{if } |\theta_{T/R}| \leq \theta_M \\ S_{T/R} & \text{otherwise,} \end{cases} \quad (2.1)$$

where T is the transmitter and R is the receiver, $\theta_{T/R}$ is the transmit/receive angle of antenna directivity and θ_M is the beamwidth of the main lobe width for the directional antenna.

However, we assume that FBSs (transmitters) are equipped with omni-directional antenna, then their antenna directivity gain would be unity and the total antenna directivity gain for the desired link is $G_{\max} = M_R$.

The total antenna directivity for the interfering links are given as

$$G_{\text{int}} = \begin{cases} M_R, & \text{with } p_M = \frac{\theta_R}{2\pi} \\ S_R, & \text{with } p_S = \frac{2\pi - \theta_R}{2\pi}, \end{cases} \quad (2.2)$$

where p_M and p_S denotes the probability that antenna gains M and S are seen by the receiver, respectively.

It should be noted that although employing directional antennas improves performance, it incurs additional cost. Therefore, we advocate the use of ESPAR as the directional antenna for the considered network.¹ As a result, Model 2 is indeed physically realisable.

2.2.2.1 ESPAR configuration

We consider a 7-element circular ESPAR array, that consists of an active element surrounded by 6 parasitic elements on equal angular separation on a circle of radius r . The ESPAR is a parasitic antenna that uses a single RF chain to transmit and receive data, and as such is a practical solution to the constraints of size, power, weight and cost on a variety of radio equipment [93].

¹Note that the performance analysis holds for any sectorized directional antenna

Table 2.1 Modelling Notations

Notation	Description
P_T	Transmit power,
Φ_k	PPP, where $k \in \{f, u\}$
λ_k	Density of PPP, where $k \in \{f, u\}$
β	Path-loss exponent
D_0	Intended link length between desired FBS and typical UT
D_i	Distance from the i^{th} interferer to the typical UT
Ψ_0	Desired Shadowing
Ψ_m	Interference Shadowing
G_{\max}	Maximum (assuming perfect alignment) distributed directivity gain (DDG)
G_{int}	Interfering (non-intended links) DDG
ζ	Received SINR from μ Wave tiers
N_0	Noise power
γ_{th}	SIR threshold
$\mathbf{E}[\cdot]$	Expectation

Furthermore, the antenna system requires mutual coupling between the active and parasitic elements; this requires closely spaced antenna elements, which makes the ESPAR antenna suitable for small mobile equipment applications, such as UT as stated in our problem.

The ESPAR antennas have been studied for a variety of applications [11, 58, 94–97]. For example, the ESPAR antenna has been used as a switched-beam antenna to implement alignment of blind interference [98] and to perform spectrum sensing for cognitive radio systems [94, 95]. Furthermore, the ESPAR has the ability to estimate signal direction by reactance domain multiple signal classification (MUSIC) [99].

2.2.3 Channel modelling

The channel model consists of lognormal shadowing and path loss components [71]. In particular, we assume that the received power P_R is given as

$$P_R = P_T G_{\max} D^{-\beta} \Psi, \quad (2.3)$$

where D denotes the distance between the transmitter and the receiver and the rest of the notations are stated in Table 2.1. The random variable (RV) Ψ represents the lognormal shadowing distributed as $\mathcal{LN}(0, \sigma^2)$ lognormal random variable with a

mean of 0 dB and a standard deviation of σ_{dB} . The shadowing is assumed to be independent of the positions of the transmitters and the receiver and also independent across channels [71].

2.2.4 SINR modelling

Using Slivnyak's theorem [100], we assume that the typical UT is located at the origin. The received SINR of the typical UT at a distance D_0 can be expressed as

$$\zeta = \frac{P_T G_{\max} D_0^{-\beta} \Psi_0}{N_0 + \sum_{i \in \Phi_f \setminus \{0\}} P_T^i G_{\text{int}}^i D_i^{-\beta} \Psi_i} \quad (2.4)$$

where $\Phi_f \setminus \{0\}$ indicates the exclusion of the node located at the origin and the rest of the notations are given in Table 2.1.

For the rest of this chapter, we assume an interference-limited network, where the background thermal noise is ignored [101]. This assumption is valid for indoor networks and dense small cell networks similar to our system model in Fig. 2.1. Thus, (2.4) reduces to

$$\gamma = \frac{P_T G_{\max} D_0^{-\beta} \Psi_0}{\sum_{i \in \Phi_f \setminus \{0\}} P_T^i G_{\text{int}}^i D_i^{-\beta} \Psi_i}. \quad (2.5)$$

2.3 Coverage Probability Analysis

In this section, we compute the coverage probability of the considered network. Directional antennas are equipped to increase SIR and hence improve the coverage. The coverage probability is referred to as the probability that the received SIR γ is greater than the required threshold γ_{th} .

The considered system model is evaluated under two different configurations according to the type of antenna (Omni or directional) and its placement at the UT, as shown in Table 2.2. The FBS always uses an omnidirectional antenna.

Instead of working with γ , its inverse $Z = 1/\gamma$ is considered, which can be defined as the co-channel interference power normalised by the desired signal power [71].

Thus, the coverage probability for UT located at distance D_0 can be written as

$$\mathcal{P}^c = \mathbb{P}(\gamma > \gamma_{\text{th}}) = \mathbb{P}(Z < \gamma_{\text{th}}^{-1}) = F_Z(\gamma_{\text{th}}^{-1}), \quad (2.6)$$

where $F_Z(\gamma_{\text{th}}^{-1})$ is the CDF of Z . From (2.6), we observe that the coverage probability can be defined as the CDF of the random variable Z .

Table 2.2 Antenna configurations for different models.

Model \ Node type	1	2
UT	Omni	Directional
FBS	Omni	Omni

Unfortunately, the interference term $\sum_{i \in \Phi_f \setminus \{0\}} P_T^i G_{\text{int}}^i D_i^{-\beta} \Psi_i$ has no closed-form expression for its CDF [102], thus it is difficult to find the distribution $F_Z(\gamma_{\text{th}}^{-1})$ in (2.6).

In order to find the distribution $F_Z(\gamma_{\text{th}}^{-1})$, we follow the approach proposed in [71], where the femtocell distribution is expressed approximately and then the coverage probability $F_Z(\gamma_{\text{th}}^{-1})$ is derived using the approximate distribution. This is explained in more detail in Proposition 1.

Proposition 1 *We consider a circular region denoted as \mathcal{R} as shown in Fig. 2.1. This assumption is valid because the received signals from FBSs outside this region will be minimal due to path-loss and blockage effects. Femtocells are randomly distributed according to a PPP in \mathcal{R} with a density λ_f . We assume that \mathcal{R} is equally divided into N subregions, such that $\mathcal{R} = \cup_{n=1}^N \mathcal{A}_n$ and $|\mathcal{A}_n| = |\mathcal{R}|/N$, where $|\cdot|$ denotes the area. One FBS is placed in \mathcal{A}_n with probability $p = \lambda_f |\mathcal{R}|/N$, if $p < 1$. Then, the total number of FBSs in \mathcal{R} is approximated by a binomial distribution with parameters N and p .*

Proof 1 *The proof is obtained by induction as stated in [71]. According to Proposition 1, the distribution of FBSs is approximated with N independent Bernoulli trials with a success probability $p = \lambda_f |\mathcal{R}|/N$. To numerically express the approximate*

femtocell distribution, \mathbf{y} is defined as a random vector of N independent Bernoulli RVs, where the n^{th} element indicates whether an FBS is placed in \mathcal{A}_n or not, as 1 or 0, respectively. The probability of having 1 as an outcome is p . A realisation of \mathbf{y} is denoted as $\mathbf{y}_m = [y_{m1}, \dots, y_{mN}]$, which represents an approximate femtocell configuration. The range of \mathbf{y} is denoted by \mathcal{Y} with a cardinality of 2^N [103].

The distribution of $F_Z(z)$ in (2.6) is obtained from the weighted sum of the distribution of Z conditioned on the given femtocell configuration \mathbf{y}_m over all possible realisations \mathcal{Y} as

$$F_Z(z) = \sum_{\mathbf{y}_m \in \mathcal{Y}} F_{Z|Y}(z|\mathbf{y}_m) \mathbb{P}(\mathbf{Y} = \mathbf{y}_m). \quad (2.7)$$

Since equal subdivisions are assumed, $\mathbb{P}(\mathbf{Y} = \mathbf{y}_m)$ is calculated using $p = \lambda_f |\mathcal{R}|/N$ as

$$\mathbb{P}(\mathbf{Y} = \mathbf{y}_m) = p^k (1-p)^{N-k}, \quad (2.8)$$

where $k = \sum_{i \in \mathcal{N}} y_{mi}$ and $\mathcal{N} = \{1, 2, \dots, N\}$.

Now that the distribution $\mathbb{P}(\mathbf{Y} = \mathbf{y}_m)$ is known, in order to have an expression for the coverage probability, the conditional distribution needs to be computed. To calculate the distribution $F_{Z|Y}(z|\mathbf{y}_m)$ which is expressed as

$$F_{Z|Y}(z|\mathbf{y}_m) = \mathbb{P} \left(\sum_{i \in \mathcal{N}} \frac{P_T^i G_{int}^i \Psi_i D_i^{-\beta} y_{mi}}{P_T G_{\max} \Psi_0 D_0^{-\beta}} > z | \mathbf{Y} = \mathbf{y}_m \right). \quad (2.9)$$

We define Z_m as

$$Z_m = \sum_{i \in \mathcal{N}} \frac{P_T^i G_{int}^i \Psi_i D_i^{-\beta} y_{mi}}{P_T G_{\max} \Psi_0 D_0^{-\beta}} = \sum_{i \in \mathcal{N}} \kappa_i e^{X_i} = e^{X_m}, \quad (2.10)$$

where

$$\kappa_i = \frac{P_T^i G_{int}^i D_i^{-\beta} y_{mi}}{P_T G_{\max} D_0^{-\beta}},$$

$$e^{X_i} = \frac{\Psi_i}{\Psi_0}$$

and e^{X_i} is lognormal RV distributed as $\mathcal{LN}(0, \sigma_{X_i}^2)$, $\sigma_{X_i}^2 = \sigma_i^2 + \sigma_0^2$. The distribution

$F_{Z|Y}(z|\mathbf{y}_m)$ can be obtained as

$$F_{Z|Y}(z|\mathbf{y}_m) \approx 1 - Q\left(\frac{\ln(z) - \mu_{f,m}}{\sigma_{f,m}}\right) \quad (2.11)$$

where $\mu_{f,m}$ and $\sigma_{f,m}$ are the mean and standard derivation, respectively. $Q(\cdot)$ is the complementary cumulative distribution function (CCDF) of the standard normal distribution defined as

$$Q(x) = \frac{1}{\sqrt{2\pi}} \int_x^\infty e^{-t^2/2} dt. \quad (2.12)$$

Fenton-Wilkinson (FW) approximation [104] is used to obtain the mean $\mu_{f,m}$ and variance $\sigma_{f,m}^2$ of e^{X_m} . The FW approximation is a lognormal probability density function (PDF) with parameters

$$\mathbb{E}[e^{X_m}] = e^{(\mu_{f,m} + 0.5\sigma_{f,m}^2)} \quad (2.13a)$$

$$\mathbb{E}[e^{2X_m}] = \left(e^{(2\mu_{f,m} + \sigma_{f,m}^2)}\right) (e^{\sigma_{f,m}^2} - 1) \quad (2.13b)$$

The mean $\mu_{f,m}$ and standard deviation $\sigma_{f,m}$ in (2.11) are obtained from (2.13) as

$$\mu_{f,m} = 2 \ln \mathbb{E}[e^{X_m}] - 0.5 \ln \mathbb{E}[e^{2X_m}] \quad (2.14)$$

$$\sigma_{f,m}^2 = \ln \mathbb{E}[e^{2X_m}] - 2 \ln \mathbb{E}[e^{X_m}] \quad (2.15)$$

Therefore, the coverage probability for the considered network can be obtained as

$$\mathcal{P}^c(\lambda_f) = \sum_{\mathbf{y}_m \in \mathcal{Y}} \left(1 - Q\left(\frac{-\ln(\gamma_{th}) - \mu_{f,m}}{\sigma_{f,m}}\right)\right) p^k (1-p)^{N-k}, \quad (2.16)$$

where $p = \lambda_f |\mathcal{R}|/N$.

This concludes the proof.

Although we could only derive an approximation for the closed-form expression for the coverage probability as given in (2.16). However, this formula can be considered as a good assumption for the analytical results which can be confirmed from the results in Section 2.4.

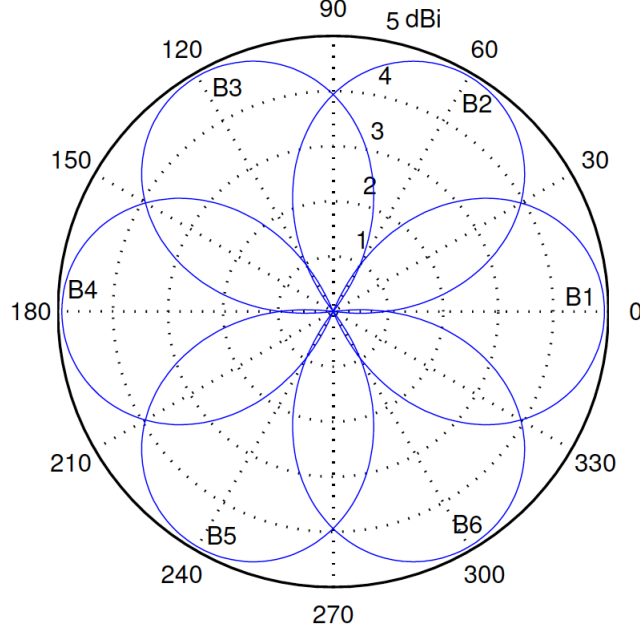


Figure 2.2 Sector beampatterns of the 7-element ESPAR [58].

2.4 Results

We compare the numerical results derived in Section 2.3 with the experimental results obtained using Monte-Carlo simulations. The values for the parameters used in simulation and analytical results are transmit power $P_T = -10$ dB, the path-loss exponent $\beta = 3$, the intensity of PPP $\lambda = 0.001$ per m^2 , the lognormal shadowing for all FBSs are considered i.i.d with mean $\mu_f = 0$ dB and standard deviation $\sigma_f = 4$ dB.

As mentioned in Section 2.3, the model configurations presented in Table 2.2 enables us to show the effect of adding directional antenna at UT to enhance the performance of the considered network. In Model 1, FBSs and UT use omnidirectional antennas, which increases the interference signal received by the typical UT, leading to reduced SIR and hence reduced coverage probability. However, in Model 2, directional antenna at the typical UT receiver ensures that the amount of interference received is limited to the angular spread of the main lobe of the antenna. This in-turn increases the SIR and hence results in improved coverage.

The antenna directivity gains for the ESPAR in simulation results are calcu-

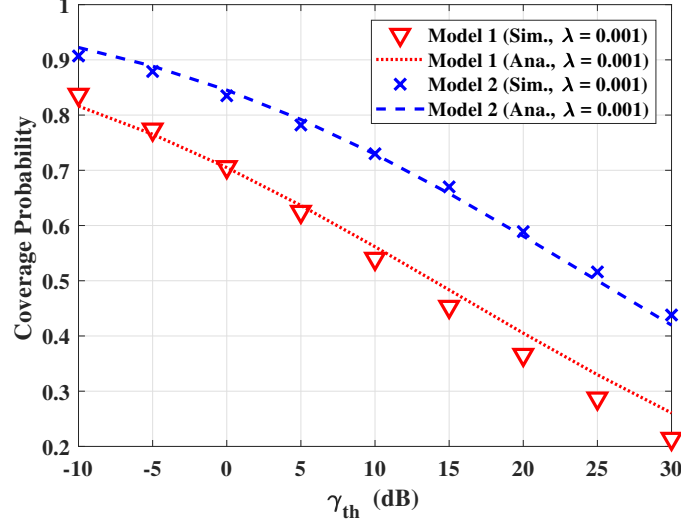


Figure 2.3 The coverage probability $\mathbb{P}[\gamma > \gamma_{th}]$ for different SIR thresholds γ_{th} for Models 1 and 2.

lated by considering a low-complexity approach where the ESPAR is exploited as a switched-beam antenna capable of predefining directional beampatterns accessing to different angle sectors. In [58, 94], it is shown that reactance loads of parasitic elements can be optimised to maximise the beampattern gain to a specific direction. Because of the symmetric antenna structure, the beampattern can be rotated to different angular positions by shifting the optimal reactance loads circularly as shown in Fig. 2.2. However, for the analytical results, we do not use the directional antenna as a switched beam antenna and choose the values for the maximum and average directivity gains approximately using the beam pattern in one particular direction. Hence, there is a small difference between simulation and analytical results for the directional antennas.

In Fig. 2.3, the coverage probability of the considered network is plotted with respect to the SIR threshold γ_{th} comparing the two Models in Table 2.2. From Fig. 2.3, we observe that Model 2 outperforms Model 1, resulting in higher coverage probability at the typical UT, as expected. In Figures 2.4 and 2.5, the effect of increasing the intensity λ of PPP on the coverage probability is presented for Models 1 and 2, respectively.

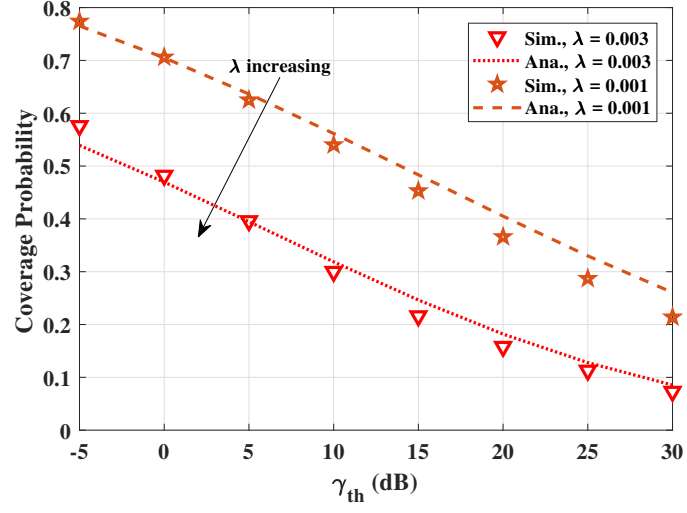


Figure 2.4 The coverage probability $\mathbb{P}[\gamma > \gamma_{th}]$ for different SIR thresholds γ_{th} for Model 1 at different intensities λ_f .

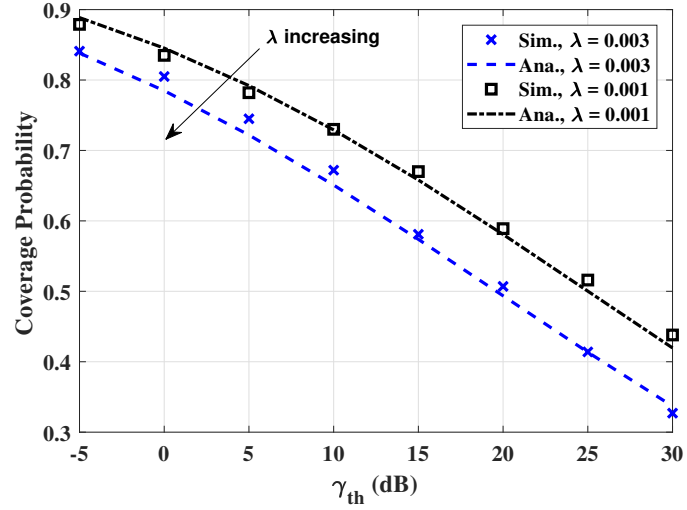


Figure 2.5 The coverage probability $\mathbb{P}[\gamma > \gamma_{th}]$ for different SIR thresholds γ_{th} for Model 2 at different intensities λ_f .

As the intensity increases, the number of FBSs increases as well as the interfering power. This results in a decrease in coverage probability as the received SIR γ decreases. This might seem as a counterintuitive result, however, this result holds for not scaling the power. Therefore, by increasing the intensity, the interference increases, hence, the coverage probability decreases. Although the coverage probability decreases in both models. However, in Model 2, the decrease of coverage probability is less than Model 1.

This is because in Model 2, having a directional antenna at the UT ensures that the amount of interference received is limited, as identified. Therefore, the number of interfering FBSs is less in Model 2 and hence the coverage probability is better.

2.5 Summary

To summarise this chapter, we analysed the coverage probability of downlink femtocell networks in presence of omnidirectional and directional antennas at the UT. Because directional antennas introduce additional cost. We proposed to exploit a 7-element ESPAR antenna which uses a single RF chain and is a practical solution for power, cost and size constraints. We assume that the channel model consists of path-loss and shadowing components. The coverage probability is calculated using the distribution for the ratio of femtocell co-channel interference to desired signal, which doesn't have a closed-form expression. Thus, we propose to obtain an approximation for the coverage probability of the considered network. First, we defined a circular region which contains the strong FBSs and ignore the interfering signal received from the other FBSs. In this region, we exploited a simplified mathematical model which presents an approximate distribution for femtocell co-channel interference to desired signal ratio by approximating the number of strong interfering FBSs to a binomial distribution. In addition to that, we used FW approximation to calculate the mean and the variance of the sum of lognormal distributions. The simulated and analytical results showed that the coverage performance of femtocell networks improves considerably when directional antenna was used at the UT, as expected. We presented also the results of varying the intensity of the PPP and its

effect on the coverage performance. The intensity of the PPP with the considered area gives an indication of how dense the network is. The denser the network, the worse the coverage performance due to the increase in the interference especially from the closer FBSs.² However, using the directional antennas showed that this degradation can be minimal, as identified.

²Under the assumption of no power scaling.

Chapter 3

Multi Tier SCN Analysis

In Chapter 2, we analysed the performance of a single-tier SCN in terms of coverage. In this chapter, we extend this work to the performance analysis of multi-tiers SCN in terms of coverage probability, ASE and EE. In Chapter 2, the channel model consisted of lognormal shadowing and path-loss components. However, in this chapter we assume small scale fading (Rayleigh) and path-loss components for our channel model. The reason for this assumption is that we already observed in Chapter 2, that assuming lognormal shadowing does not lead to a closed-form expression for the coverage probability. Moreover, the multi-tier HetNet is a more complex system model, thus we wanted to work with simple assumption for the channel conditions to give us a better understanding of the performance analysis. This work could then be continued with more complex assumptions that mimics the real-world scenarios. In this chapter, specifically, we consider a three-tier hybrid cellular HetNet using microwave (μ Wave) links for the first two-tiers and mmWave links for the last tier. The two-tiers with μ Wave links form a wireless backhaul to the last tier with mmWave links. Different configurations based on the placement of the directional antennas at each tier are explored similar to our approach in Chapter 2.

3.1 Introduction

As stated in Chapter 1 [Section 1.1], a layered structure of macrocells, femtocells, and/or picocells can be incorporated in a HetNet to offer more improvement for the wireless coverage in various scenarios ranging from open outdoor environments to office buildings, homes and underground areas. Apart from the improved coverage, there are several benefits to HetNet, including increased reliability and improved spectrum efficiency [5, 16, 17].

In this chapter, we study the performance of a three-tier hybrid cellular HetNet using μ Wave links for the first two-tiers and mmWave links for the last tier. This system model resembles the system model used in [80] which consists of small cells overlaid with macrocells. However, in our model the UTs can only communicate to mmWave tier and have no direct access links to the μ Wave tiers. We assume that the rate required by the mmWave users is compared to that offered by the μ Wave links. In previous works [7, 79, 80], the end-users were assumed to have the ability to operate in μ Wave or mmWave, which implies that the user's radio equipment operates over a wide frequency range. Practically, this assumption increases the cost of end-user's equipment. Therefore, we considered the scenario where end-users have mmWave equipment only and hence can connect to the last tier. Moreover, we use the μ Wave links as the wireless backhaul to the mmWave users.

Wireless backhaul recently gained a lot of attention in multi-tier networks to overcome the expensive cost of wired backhaul architecture and the installation difficulty [67–69, 105–109]. One of the main challenges in having a wireless backhaul is to mitigate interference. The proposed methods in [67–69] tried to reduce the interference, but these methods required additional infrastructure that led to increased expenditure.

This motivated us to propose a novel and practical model where we can reuse the μ Wave infrastructure, but equip the BSs with directional antennas to have a robust wireless backhaul network. The use of directional antennas not only suppresses interference and increases SINR, but also leads to lower system complexity

as discussed later in Section 2.2.2.1 in Chapter 2.

Therefore, we equip directional antennas to mitigate the interference and different configurations based on the placement of the directional antennas at each tier are explored. The analysis of the key performance indicators, namely, the coverage probability, ASE and EE using the conventional minimum rate model, and the simulation results associated with these parameters are presented. Since we want to analyse the considered hybrid network with a wireless backhaul, we investigate an optimisation problem for the overall ASE and EE with respect to the optimal SIR threshold required for μ Wave and mmWave links. Results show that the optimal SIR threshold required for the μ Wave tiers (wireless backhaul) depends only on the path-loss exponent and that for the mmWave tier depends on the area of LOS region.

Finally, we consider the average rate under coverage instead of the conventional minimum rate model, and present that the ASE and EE are strictly decreasing functions with respect to the threshold, thereby we conclude that they can be maximized by choosing the lowest possible SIR threshold available in the system [6].

3.2 System Model

In this section, we define our system model for the performance analysis of the hybrid HetNet. We focus on evaluating a two-tiers μ Wave network as a wireless backhaul network for a non-dense mmWave network in terms of coverage, rate under coverage, ASE and EE. The system model is shown in Fig.3.1. The mathematical formulation and the underlying assumptions are discussed in the following subsections.

3.2.1 Poisson Point Process (PPP) BSs and Users

The μ Wave tier consists of MBSs and FBSs and the mmWave tier consists of picocell base station (pBS)s. Each tier of the HetNet is modelled as an independent PPP Φ_k with density λ_k , where $k \in \{m, f, w\}$ indicating macro, femto and pico tiers, respectively. All base stations (femto and macro) are considered to operate in open

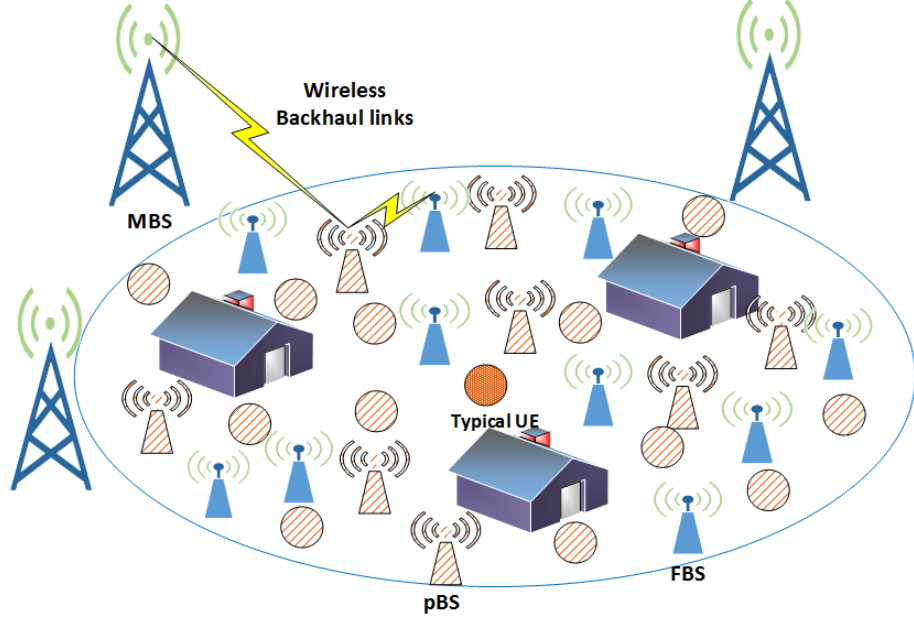


Figure 3.1 A three-tier hybrid cellular HetNet using μ Wave links (wireless backhaul links) for the first two-tiers and mmWave links for the last tier

access. Open access refers to the scenario that a typical pBS is allowed to connect to base stations from any μ Wave tier [5]. The decision criteria on whether to connect to a MBS or to a FBS will be discussed in more detail in Section 3.3.

The end-users, referred by the term user equipments (UEs), are also modelled as a PPP Φ_u with density λ_u . The UEs only communicate with pBSs in the mmWave band. In other words, the pBSs relay the information from the first two-tiers (μ Wave) to the UEs. It is assumed that the rate required by the mmWave UE is comparable to that offered by the μ Wave links.

3.2.2 Directional beamforming modelling

For μ Wave and mmWave tiers, all directional antennas are approximated by a sectorized antenna model which renders the analysis tractable [76]. In the sectorized antenna model, antenna gains are assumed to be constant M for all angles within the beamwidth of the main lobe, and another constant S otherwise. Mathematically, the antenna gain (transmit/ receive) is given in (2.1).

As discussed in Chapter 2 [Section 2.2.2], when the transmitter node is equipped

with omni-directional antenna, then its antenna directivity gain would be unity and the total antenna directivity gain for the desired link is $G_{\max} = M_R$. The total antenna directivity for the interfering links G_{int} as in (2.2).

For both transmit and receive nodes equipped with directional antennas, we assume perfect alignment between the desired and typical nodes. Then for the desired link, $G_{\max} = M_T M_R$, but for other interfering links, θ_T and θ_R are assumed to be independent and uniformly distributed in $(0, 2\pi]$, which results in a random directivity gain G_{int} . Therefore, the directivity gain in an interference link G_{int} is a discrete random variable, as shown in (3.1)

$$G_{\text{int}} = \begin{cases} M_T M_R & p_{MM} = \left(\frac{\theta_T}{2\pi}\right) \left(\frac{\theta_R}{2\pi}\right) \\ M_T S_R & p_{MS} = \left(\frac{\theta_T}{2\pi}\right) \left(\frac{2\pi - \theta_R}{2\pi}\right) \\ S_T M_R & p_{SM} = \left(\frac{2\pi - \theta_T}{2\pi}\right) \left(\frac{\theta_R}{2\pi}\right) \\ S_T S_R & p_{SS} = \left(\frac{2\pi - \theta_T}{2\pi}\right) \left(\frac{2\pi - \theta_R}{2\pi}\right), \end{cases} \quad (3.1)$$

where p_{lk} , with $l, k \in \{M, S\}$ denotes the probability that the corresponding antenna gains are seen by the receiver.

3.2.3 Small-Scale Fading

We assume independent small-scale Rayleigh fading channels¹ Ψ_k where $k \in \{f, m, w\}$, with β as the path-loss exponent for the two μ Wave links. But in mmWave networks, measurements have shown difference between the path-loss exponents for LOS and non-line-of-sight (NLOS) links [76].

Therefore, the path-loss exponents in mmWave links are α_L and α_N , for LOS and NLOS, respectively. Due to the thinning property in stochastic geometry [56], the density of pBSs Φ_w can be split into two marked PPPs Φ_w^L with density $p_L \lambda_w$ and Φ_w^N with density $(1 - p_L) \lambda_w$. All notations are listed in Table 3.1.

¹Small scale fading on mmWave networks is applicable for some particular cases of mmWave networks [110].

Table 3.1 Modelling Notations

Notation	Description
P_T^k	Transmit power, where $k \in \{m, f, w\}$
Φ_k	PPP, where $k \in \{m, f, w\}$
λ_k	Density of PPP, where $k \in \{m, f, w\}$
D_j	Intended link length between j^{th} BS and typical pBS, where $j \in \{m, f\}$
D_w	Intended link length between p^{th} BS and typical mmWave UE
β	Path-loss exponent of μ Wave tiers
α_L	LOS path-loss exponent for pBSs (mmWave tier)
α_N	NLOS path-loss exponent for pBSs (mmWave tier)
p_L	LOS probability
D_i	Distance from the interferer i to the typical pBS
h_0^k	Desired fading channel, where $k \in \{m, f, w\}$
h_i^k	Interference fading channel, where $k \in \{m, f, w\}$
G_{\max}^k	Maximum (assuming perfect alignment) DDG, where $k \in \{m, f, w\}$
G_{int}^k	Interfering (non-intended links) DDG, where $k \in \{m, f, w\}$
ζ_μ	Received SINR from μ Wave tiers
ζ_w	Received SINR from mmWave tier
σ^2	Thermal noise
r_w	Radius of LOS region in mmWave tier
γ_{th_j}	μ Wave SIR threshold, where $j \in \{m, f\}$
ζ_{th_w}	mmWave SINR threshold

3.2.4 LOS BS and path-loss Model for mmWave links

Let the length of the mmWave link between p^{th} BS and the typical UE be denoted by D_w . Since the distribution of blockages is stationary and isotropic, the probability that the link is LOS, indicated by p_L , only depends on the link length D_w [111]. Considering the LOS area to be within a circular ball of radius r_w centered around the pBS location (where r_w denotes the maximum distance for LOS communication), we get

$$p_L = \begin{cases} 1 & \text{if } D_w \leq r_w \\ 0 & \text{otherwise.} \end{cases} \quad (3.2)$$

Since the LOS and NLOS probabilities are complementary, the NLOS probability $p_N = 1 - p_L$.

Different path-loss laws apply to LOS and NLOS links. Given a link length D_w between intended p^{th} BS and typical mmWave UE, the path-loss value $L(D_w)$ can be computed as in [76].

3.2.5 SINR modelling:

3.2.5.1 μ Wave tiers

Using Slivnyak's theorem [100], we assume that the receiver for the first two μ Wave tiers, the typical pBS, is located at the origin. The received SINR of the typical pBS at a distance D_j associated with its j^{th} tier BS, for $j \in \{m, f\}$ can be expressed as

$$\zeta_\mu^j = \frac{P_T^j |h_0^j|^2 G_{\max}^j D_j^{-\beta}}{\sigma^2 + \sum_{j \in \{m, f\}} \sum_{i \in \Phi_j \setminus \{0\}} P_T^j |h_i^j|^2 G_{\text{int}_i}^j r_i^{-\beta}} \quad (3.3)$$

where the notations and descriptions are given in Table 3.1.

3.2.5.2 mmWave tier

μ Wave and mmWave tiers are independent, therefore, we can apply Slivnyak's theorem to the last tier by considering a typical UE at the origin. Thus, the received SINR of a typical UE at distance D_w from pBSs can be expressed as

$$\zeta_w = \frac{P_T^w |h_0^w|^2 G_{\max}^w L(D_w)}{\sigma^2 + \sum_{z \in \{L, N\}} \sum_{y \in \Phi_w^z \setminus \{0\}} P_T^w |h_y^w|^2 G_{\text{int}_y}^w L(r_y)} \quad (3.4)$$

where $L(r_y)$ is the path loss value with respect to the interfering pBSs and $L(D_w)$ is defined in Section 3.2.4. The rest of the notations and definitions are given in Table 3.1.

3.3 Performance Analysis for μ Wave and mmWave tiers

We analyse the coverage probability, ASE and EE in the proposed system using the stochastic geometry tools. For the μ Wave tier, pBSs are considered as receivers and for the mmWave tier, the UEs are considered as receivers. Directional antennas are equipped at the μ Wave tiers to increase SINR and hence improve the coverage. The coverage probability is referred to as the probability that the received SINR is bigger than a required threshold and it is considered as the base building block for the analysis of all other parameters such as average rate, ASE and EE [16, 17]. ASE can be quantified as the total rate in the unit area normalised by the bandwidth. EE can be measured as the ratio of the ASE to the average network power consumption. In this section, we consider the minimum average rate model for both μ Wave and mmWave tiers [112, 113]. Our objective is to find the optimal SINR threshold that maximises ASE and EE.

3.3.1 Coverage Probabilities \mathcal{P}_μ^c and \mathcal{P}_w^c

3.3.1.1 μ Wave tier Coverage Probability \mathcal{P}_μ^c

For the rest of the μ Wave analysis, we consider SIR ζ instead of SINR γ . This is because it was shown in Section V of [5] that in multi-tier HetNets, self-interference dominates thermal noise. Hence, thermal noise has a very limited effect on the coverage probability of multi-tier HetNets. We consider instantaneous SIR based scheme [18], where the pBS connects to the μ Wave tier j if the instantaneous SIR γ_j exceeds γ_{th_j} , where $j = \{m, f\}$. In the case where both tiers have a connection with the typical pBS, then this typical pBS is covered by the tier with the highest SIR. We assume that the SIR can connect to at most one tier and that $\gamma_{\text{th}_j} > 1$ [5].

Table 3.2 Antenna configurations for different models.

Model \ BS Type	1	2	3	4
FBS	Omni	Directional	Omni	Directional
pBS	Omni	Omni	Directional	Directional

3.3.1.1.1 Model Configuration

The considered system model is evaluated under four different configurations according to the type of antenna and its placement at FBS and FBS, as shown in Table 3.2. The MBSs always use an omni-directional antenna and the UEs always employ a directional antenna for all the configurations. Evaluating different configurations enables us to show the effect of adding directional antenna at one or more tiers to enhance the performance of the considered network.

Proposition 2 *Following the model in [114], the analytical coverage probability for directional antenna used at different tiers can be derived as*

$$\mathcal{P}_\mu^c = \frac{\pi}{C(\beta)} \frac{\sum_{j \in \{m, f\}} \lambda_j (P_T^j G_{\max}^j)^{2/\beta} \gamma_{th_j}^{-2/\beta}}{\sum_{j \in \{m, f\}} \lambda_j (P_T^j G_{\min}^j)^{2/\beta}}, \quad (3.5)$$

where $C(\beta) = \frac{2\pi^2}{\beta} \csc(\frac{2\pi}{\beta})$, $\csc(\cdot) = \frac{1}{\sin(\cdot)}$, G_{\min}^j is the average interfering directivity gains, where $G_{\min}^f = \sum p_{lk} (l_T k_R)$ where $l, k \in \{M, S\}$, and $G_{\min}^m = p_M M + p_S S$.

Proof 2 *The coverage probability in a K -tier wireless backhaul network under instantaneous SIR based scheme for directional antennas equipped at FBSs and typical pBS can be derived as follows:*

$$\begin{aligned} \mathcal{P}_\mu^c &\stackrel{(a)}{=} \sum_{i=1}^K \mathbb{E} \left[\sum_{x_i \in \Phi_i} \mathbf{1}(\gamma_i > \gamma_{th_i}) \right] \\ &\stackrel{(b)}{=} \sum_{i=1}^K \lambda_i \int_{\mathbb{R}^2} \mathbb{P} \left(\frac{P_T^i G_{\max}^i |h_0^i|^2 x_i^{-\beta}}{I_{x_i}} > \gamma_{th_i} \right) dx_i, \\ &\stackrel{(c)}{=} \sum_{i=1}^K \lambda_i \int_{\mathbb{R}^2} \mathcal{L}_{I_i} \left(\frac{\gamma_{th_i} x_i^\beta}{P_T G_{\max}^i} \right) dx_i, \end{aligned} \quad (3.6)$$

(a) follows Lemma 1 [5] under the assumption that $\theta_i > 1$, (b) follows Campbell-

Mecke Theorem [55], and (c) follows the assumption of Rayleigh distributed channel coefficients. Since the point processes are stationary, the interference is independent of the location of the nodes. Thus, the total interference $I_{total} = \sum_{i=1}^K I_{x \in \Phi_i}$, where $I_i = \sum_{j \in \Phi_j} P_T^j G_{int}^i |h_j|^2 x_j^{-\beta}$ for $i = (1, 2, 3 \dots K)$. Then, $\mathcal{L}_{I_i}(s)$ is given by.

$$\begin{aligned} \mathcal{L}_{I_i}(s) &= \prod_{j=1}^K \mathbb{E}_{\Phi_j} \left[\prod_{j \in \Phi_j} \mathbb{E}_h \exp \left(-s \epsilon x^\beta P_T^j G_{int}^j |h_j|^2 x_j^{-\beta} \right) \right], \\ &\stackrel{(a)}{=} \prod_{j=1}^K \mathbb{E}_{\Phi_j} \left[\prod_{j \in \Phi_j} \frac{1}{(1 + s \rho x_j^{-\beta})} \right], \\ &\stackrel{(b)}{=} \prod_{j=1}^K \exp \left(-2\pi \lambda_j p_j \int_0^\infty \left(1 - \frac{1}{(1 + s \rho x_j^{-\beta})} \right) dx_j \right), \end{aligned} \quad (3.7)$$

where $\rho = \epsilon x^\beta P_T^j G_{int}^j$, $\epsilon = \gamma_{th}^i / P_T^i G_{max}^i$, (a) follows the assumption of Rayleigh fading, and (b) follows from PGFL of PPP [55]. By substituting (3.7) in (3.6) and under the assumption of Rayleigh fading and neglecting the noise, a closed-form expression for the total coverage probability is given by

$$\mathcal{P}_\mu^c = \frac{\pi}{C(\beta)} \frac{\sum_{j \in \{m, f\}} \lambda_j (P_T^j G_{max}^j)^{2/\beta} \gamma_{th_j}^{-2/\beta}}{\sum_{j \in \{m, f\}} \lambda_j (P_T^j G_{min}^j)^{2/\beta}}. \quad (3.8)$$

This concludes the proof.

The total coverage probability can be calculated as the sum of all the individual coverage probabilities of all tiers given that $\gamma_j > 1$ [5]:

$$\mathcal{P}_\mu^c = \mathcal{P}_m^c + \mathcal{P}_f^c, \quad (3.9)$$

Our system model is based on the assumption that the probabilities of different tiers are mutually exclusive, .i.e., if $\mathcal{P}_m^c = 1$, then $\mathcal{P}_f^c = 0$. Then, the individual coverage

probabilities are given as

$$\mathcal{P}_f^c = \frac{\pi}{C(\beta)} \frac{\lambda_f (P_T^f G_{\max}^f)^{2/\beta} \gamma_{\text{th}_f}^{-2/\beta}}{\sum_{j \in \{m, f\}} \lambda_j (P_T^j G_{\min}^j)^{2/\beta}}, \quad (3.10a)$$

$$\mathcal{P}_m^c = \frac{\pi}{C(\beta)} \frac{\lambda_m (P_T^m G_{\max}^m)^{2/\beta} \gamma_{\text{th}_m}^{-2/\beta}}{\sum_{j \in \{m, f\}} \lambda_j (P_T^j G_{\min}^j)^{2/\beta}}, \quad (3.10b)$$

3.3.1.2 mmWave tier Coverage Probability \mathcal{P}_w^c

For the mmWave analysis, unlike the μ Wave analysis, we consider SINR threshold ζ_{th} . Because mmWave is a single tier and we assume non-dense network, therefore the thermal noise can not be ignored [76]. Hence, the coverage probability for the mmWave links (UEs) based on the highest received SINR is analysed. We consider the UE to be covered by the pBS with the highest SINR [113]. Note that in mmWave networks, different path-loss laws are applied to LOS and NLOS links [9, 75].

Proposition 3 *The total coverage probability of the mmWave tier, \mathcal{P}_w^c , is given by*

$$\mathcal{P}_w^c = \mathcal{P}_L^c + \mathcal{P}_N^c, \quad (3.11)$$

where \mathcal{P}_L^c and \mathcal{P}_N^c are the LOS, and NLOS coverage probabilities, respectively.

The LOS and NLOS coverage probabilities $\mathcal{P}_L^c, \mathcal{P}_N^c$ can be written mathematically as,

$$\mathcal{P}_L^c = e^{-s_L - 2\pi\lambda_w\Theta_1} \quad (3.12a)$$

$$\mathcal{P}_N^c = e^{-s_N - 2\pi\lambda_w\Theta_2} \quad (3.12b)$$

respectively,

where

$$s_L = \frac{\zeta_{th_w} r_w^{\alpha_L} \sigma^2}{P_T^w G_{\max}^w}, s_N = \frac{\zeta_{th_w} r_w^{\alpha_N} \sigma^2}{P_T^w G_{\max}^w}, \quad (3.13a)$$

$$\Theta_1 = \left[p_L \int_0^{r_w} \frac{y}{1 + s_1^{-1} y^{\alpha_L}} dy + p_N \int_0^{r_w} \frac{z}{1 + s_1^{-1} z^{\alpha_N}} dz \right], \quad (3.13b)$$

$$\Theta_2 = \left[p_L \int_{r_w}^{\infty} \frac{y}{1 + s_2^{-1} y^{\alpha_L}} dy + p_N \int_{r_w}^{\infty} \frac{z}{1 + s_2^{-1} z^{\alpha_N}} dz \right], \quad (3.13c)$$

$$s_1 = \frac{\zeta_{th_w} r_w^{\alpha_L} G_{\min}^w}{G_{\max}^w}, s_2 = \frac{\zeta_{th_w} r_w^{\alpha_N} G_{\min}^w}{G_{\max}^w}. \quad (3.13d)$$

where p_L and p_N are defined in Section 3.2.4, G_{\max}^w and G_{\min}^w are the maximum and minimum antenna directivity gains, respectively, that can be calculated as described in Section 3.2.2 and Proposition 2. The rest of the notations are defined in Table 3.1.

Proof 3 *The mmWave typical user is always connected to the nearest mmWave pBS. The nearest mmWave pBS can be located either in the LOS or NLOS regions. The LOS region is denoted as a circle surrounding the mmWave UE with a certain radius r . If the mmWave pBS is within this circle, then it is a LOS mmWave pBS. If this circle is empty, (i.e. there is no mmWave pBS in it), then the nearest mmWave pBS is a NLOS pBS. We consider the PPP of the mmWave pBSs divided into two-tiers network, consisting of the LOS PPP (Φ_L) with intensity λp_L and NLOS PPP (Φ_N) with intensity λp_N . These two marked PPPs are homogeneous due to the assumption of fixed LOS probability. Therefore the coverage probability can be written as*

$$\begin{aligned} \mathcal{P}_w^c &= \sum_{i \in \{L, N\}} \mathbb{E}_r [\mathbf{1}(\zeta_i > \zeta_{th_w} | r \leq r_w)] f_r(r_w), \\ &= \sum_{i \in \{L, N\}} \int_{r>0} \mathbb{P} \left(\frac{P_T^w G_{\max} |g_0|^2 x_i^{-\alpha_i}}{\sigma^2 + I_i} > \zeta_{th_w} | x_i < r_w \right) f_{x_i}(r_w) dx_i, \\ &= \sum_{i \in \{L, N\}} \int_{r>0} \mathbb{P} \left(|g_0|^2 > \frac{\zeta_{th_w} x_i^{\alpha_i} (\sigma^2 + I_i)}{P_t^w G_{\max}} | x_i < r_w \right) f_{x_i}(r_w) dx_i. \end{aligned} \quad (3.14)$$

Since the mmWave channel experience Rayleigh fading, then the channel gain is

exponentially distributed. Therefore, (3.14) becomes

$$\mathcal{P}_w^c = \sum_{i \in \{L, N\}} e^{\frac{\zeta_{thw} x_i^{\alpha_i} \sigma^2}{P_T^w G_{\max}}} \mathbb{E}_{x_i \in \Phi_i} \left[e^{\frac{\zeta_{thw} x_i^{\alpha_i} I_i}{P_T^w G_{\max}}} \right], \quad (3.15)$$

where the total interference I is the sum of the interference from LOS and NLOS mmWave pBSs given as

$$I = \sum_{j \in \Phi_L} P_T^w G_{\min_j} |g_j|^2 y_j^{-\alpha_L} + \sum_{n \in \Phi_N} P_T^w G_{\min_n} |g_n|^2 y_n^{-\alpha_N}. \quad (3.16)$$

By substituting in (3.15) using (3.16), and using the stochastic geometry steps similar to the HetNet case, (3.12a) and (3.12b) are obtained. This concludes the proof.

3.3.2 Average Rates R_μ and R_w

In literature, typically the minimum rate model is used for μ Wave tiers, which is $R_\mu = \log(1 + \gamma_{th_\mu})$, where $\gamma_{th_\mu} = \gamma_{th_m} = \gamma_{th_f}$ is the predefined threshold common to all the μ Wave tiers [112]. Furthermore, the mmWave is a single tier with a single threshold ζ_{th_w} , that is the same for LOS and NLOS pBSs. Therefore, the minimum achieved rate by the typical UE only depends on the required threshold ζ_{th_w} is given by [115]

$$R_w = \log(1 + \zeta_{th_w}). \quad (3.17)$$

3.3.3 ASE and EE Analysis in terms of minimum rate model

3.3.3.1 ASE η and EE Ω Optimisation

Our objective is to find the optimal threshold ² for the considered system model that maximises ASE and EE. Because the μ Wave and mmWave tiers operate at different frequencies, they are considered independent and they have different thresholds. Thus, the overall ASE η_{tot} and EE Ω_{tot} for the three tier hybrid cellular network are

²Please note that the optimal threshold mentioned here is not the quality of service (QoS) threshold.

the sum of these metrics for each tier. Mathematically,

$$\eta_{\text{tot}} = \sum_{j \in \{m, f\}} \lambda_j \mathcal{P}_j^c(\gamma_\mu) R_\mu + \lambda_w \mathcal{P}_w^c(\gamma_w) R_w, \quad (3.18a)$$

$$\Omega_{\text{tot}} = \frac{\sum_{j \in \{m, f\}} \lambda_j \mathcal{P}_j^c(\gamma_\mu) R_\mu + \lambda_w \mathcal{P}_w^c(\gamma_w) R_w}{\sum_{j \in \{m, f\}} \lambda_j (P_{j0} + \Delta_j P_j) + \lambda_w (P_{w0} + \Delta_w P_w)}, \quad (3.18b)$$

where P_{k0} is the static power, P_k is the RF output power, and Δ_k is the slope of load-dependent power consumption [116], for $k \in \{f, m, w\}$, indicating femto, macro and pico tiers. Since we assume here that the density is fixed, the optimisation is with respect to the SIR threshold. This SIR threshold represents a value that acts as the minimal value the received SIR threshold should be to ensure coverage and communication. Moreover, this threshold not only affects the coverage probability (which implies that the transmission links are reliable), but also the rate at which the nodes are communicating. Moreover, since the μ Wave tiers operate as wireless backhaul to the mmWave tier, the rate of backhaul transmissions in μ Wave tiers should be greater than the rate of access transmissions in mmWave tier.

Therefore, the overall optimisation problems for the ASE (η_{tot}) and EE (Ω_{tot}) are given, respectively, as

$$\underset{\gamma_{\text{th}_\mu}, \gamma_{\text{th}_w}}{\text{maximize}} \quad \eta_{\text{tot}}, \quad (3.19)$$

$$\text{subject to} \quad R_\mu > R_w,$$

$$\underset{\gamma_{\text{th}_\mu}, \gamma_{\text{th}_w}}{\text{maximize}} \quad \Omega_{\text{tot}}, \quad (3.20)$$

$$\text{subject to} \quad R_\mu > R_w,$$

Considering that the μ Wave and mmWave tiers operate at different frequencies and the two-tiers are independent, the overall optimisation problem can be split into two independent problems as shown in the following.³

³Please note that we present the analysis for ASE only. This is because both EE and ASE are related by a constant (power consumption) which is independent of the required threshold. However, in the results section we present both metrics.

3.3.3.1.1 μ Wave tier

In order to find the optimal SIR threshold that maximises the ASE for the μ Wave tier, the optimisation problem is stated as in (3.19), where the constraint insures higher data rate for wireless backhaul information than access information [68].

The solution to the optimisation problem (3.19) is shown in the proof of the following Proposition.

Proposition 4 *The optimal threshold γ_μ^* of μ Wave tier to obtain the maximum ASE η_μ is only dependent on the path-loss exponent β of the μ Wave tier,*

$$\gamma_\mu^* = e^{\xi^*} - 1, \quad (3.21)$$

where $\xi^* = \frac{a * W(-\frac{e^{-1/a}}{a}) + 1}{a}$, $a = 2/\beta$, and $W(.)$ is the Lambert Function.

Proof 4 *The optimisation problem can be formulated as the following :*

$$\begin{aligned} & \underset{\gamma_\mu, \gamma_w}{\text{maximize}} \quad \left[\lambda_f \mathcal{P}_f^c(\gamma_\mu) + \lambda_m \mathcal{P}_m^c(\gamma_\mu) \right] \log(1 + \gamma_\mu) + \lambda_w \mathcal{P}_w^c(\gamma_w) R_w, \\ & \text{subject to} \quad \log(1 + \gamma_\mu) > \log(1 + \gamma_w), \end{aligned} \quad (3.22)$$

or as an equivalent problem,

$$\begin{aligned} & \underset{\gamma_\mu, \gamma_w}{\text{maximize}} \quad \left[\lambda_f \mathcal{P}_f^c(\gamma_\mu) + \lambda_m \mathcal{P}_m^c(\gamma_\mu) \right] \log(1 + \gamma_\mu) + \lambda_w \mathcal{P}_w^c(\gamma_w) R_w, \\ & \text{subject to} \quad \gamma_\mu > \gamma_w. \end{aligned} \quad (3.23)$$

To solve this problem, we first assume a fixed value for $\gamma_w = \gamma_w^{th}$ and the final optimisation problem is given as

$$\begin{aligned} & \underset{\gamma_\mu^*}{\text{maximize}} \quad \left[\lambda_f \mathcal{P}_f^c(\gamma_\mu) + \lambda_m \mathcal{P}_m^c(\gamma_\mu) \right] \log(1 + \gamma_\mu) + \eta_w, \\ & \text{subject to} \quad \gamma_\mu > \gamma_w^{th}. \end{aligned} \quad (3.24)$$

Using the Lagrangian function [117], we get

$$\mathbb{L}(\gamma_\mu) = - \left[\lambda_f \mathcal{P}_f^c(\gamma_\mu) + \lambda_m \mathcal{P}_m^c(\gamma_\mu) \right] \log(1 + \gamma_\mu) - \eta_w - \epsilon_1 [\gamma_\mu - \gamma_w^{th}], \quad (3.25)$$

where ϵ_1 is the Lagrange multiplier. The derivative of the Lagrangian function with respect to γ_μ is computed as :

$$\frac{\partial \mathbb{L}}{\partial \gamma_\mu} = \frac{\gamma_\mu}{1 + \gamma_\mu} - \frac{2}{\beta} \ln(1 + \gamma_\mu) - \epsilon_1. \quad (3.26)$$

Using the Karush-Kuhn-Tucker (KKT) conditions [117], and in particular the complementary slackness condition, $\epsilon_1(\gamma_\mu - \gamma_w^{th}) = 0$ and applying a change of variable, i.e., setting $\ln(1 + \gamma_\mu) = \xi$, the optimal solution can be found as

$$\xi^* = \frac{a * W\left(-\frac{e^{-1/a}}{a}\right) + 1}{a}, \quad (3.27)$$

where $a = 2/\beta$, and $W(\cdot)$ is the Lambert Function. Therefore, $\gamma_\mu^* = e^{(\xi^*)} - 1$, which shows that the optimal SIR threshold γ_μ^* only depends on the path-loss exponent β .

This concludes the proof.

3.3.3.1.2 mmWave tier

We need to find the optimal SINR threshold for mmWave BSs (γ_w) that maximises the ASE with the threshold of the μ Wave tiers fixed as γ_μ^{th} . To this end, we define a new optimisation problem,

$$\begin{aligned} & \underset{\gamma_w^*}{\text{maximize}} && \eta_\mu + \lambda_w \mathcal{P}_w^c(\gamma_w) R_w, \\ & \text{subject to} && \gamma_w < \gamma_\mu^{th}. \end{aligned} \quad (3.28)$$

The Lagrangian function is given by

$$\mathbb{L}(\gamma_w) = -(\eta_\mu + \lambda_w \mathcal{P}_w^c(\gamma_w) R_w) + \epsilon_2 [\gamma_w - \gamma_\mu^{th}], \quad (3.29)$$

where ϵ_2 is the Lagrange multiplier. The optimal SINR threshold can be computed by differentiating (3.29) with respect to γ_w , and equating the result to zero.

The integrals in (3.13) can be computed as

$$\int \frac{y}{1 + s_1^{-1} y^{\alpha_L}} dy = \frac{s_1}{2} \log(|1 + s_1^{-1} r_w^2|), \quad (3.30a)$$

$$\int \frac{z}{1 + s_1^{-1} z^{\alpha_N}} dz = \frac{1}{2} r_w^2 {}_2F_1(a_N, b; c; T_1), \quad (3.30b)$$

$$\int \frac{y}{1 + s_2^{-1} y^{\alpha_L}} dy = \frac{s_2}{2} \log(|1 + s_2^{-1} r_w^2|), \quad (3.30c)$$

$$\int \frac{z}{1 + s_2^{-1} z^{\alpha_N}} dz = \frac{1}{2} r_w^2 {}_2F_1(a_N, b; c; T_2), \quad (3.30d)$$

where $\alpha_L = 2$, $\alpha_N \neq 2$, ${}_2F_1(a_N, b; c; T)$ is the Hypergeometric function and $a_N = 2/\alpha_N$, $b = 1$, $c = a_N + 1$, $T_1 = -s_1^{-1} r_w^{\alpha_N}$ and $T_2 = -s_2^{-1} r_w^{\alpha_N}$, where s_1 and s_2 were defined in Proposition 3. Unfortunately, this problem is not analytically tractable. Therefore, we only show a plot of different SINR thresholds and their corresponding ASE in Section 3.4.

3.3.4 ASE and EE Analysis in terms of average rate under coverage

3.3.4.1 Average Rate under Coverage R^c

In this section, we redo the analysis of the ASE and EE ⁴ for multi-tier μ Wave links considering the average rate under coverage instead of the minimum rate model. Please note that this parameter is not the same as the classic ergodic rate, because the rate is calculated conditioned that the typical pBS being in coverage.

Proposition 5 *The average rate under coverage is greater than or equal to mini-*

⁴Please note that we present the analysis for area spectral efficiency only. This is because both energy and area spectral efficiencies are related by a constant (power consumption) which is independent of the required threshold. However, in the results section we present both metrics.

mm average rate and can be analytically computed as

$$R_\mu^c = \log(1 + \gamma_{\min}) + \frac{\sum_{j \in \{m, f\}} \lambda_j (P_t^j G_{\max}^j)^{2/\beta} \mathcal{A}(\beta, \gamma_j, \gamma_{\min})}{\sum_{j \in \{m, f\}} \lambda_j (P_t^j G_{\max}^j)^{2/\beta} \gamma_j^{-2/\beta}}, \quad (3.31)$$

where

$$\mathcal{A}(\beta, \gamma_j, \gamma_{\min}) = \int_{\gamma_{\min}}^{\infty} \frac{\max(\gamma_j, x)^{-2/\beta}}{1+x} dx$$

and $\gamma_{\min} = \min(\gamma_m, \gamma_f)$.

The rest of the notations and definitions are given in Table 3.1.

Proof 5 We denote the coverage event $\cup_{j \in \{m, f\}} \cup_{x \in \Phi_j} (\gamma(x) > \gamma_j)$ by $\mathbf{V}(\{\gamma_j\})$, the achievable average rate by a randomly chosen user when it is under coverage is given as

$$\bar{R} = \mathbb{E} \left[\log \left(1 + \max_{x \in \cup \Phi_j} \gamma(x) \right) | \mathbf{V}(\{\gamma_j\}) \right]. \quad (3.32)$$

First, the conditional CCDF of $\max_{x \in \cup \Phi_j} (\gamma(x))$ is derived as follows:

$$\begin{aligned} \mathbb{P} \left(\max_{x \in \cup \Phi_j} (\gamma(x) > T | \mathbf{V}(\{\gamma_j\})) \right) &\stackrel{(a)}{=} \frac{\mathbb{P} \left(\max_{x \in \cup \Phi_j} (\gamma(x) > T, \mathbf{V}(\{\gamma_j\})) \right)}{\mathbb{P}(\mathbf{V}(\{\gamma_j\}))}, \\ &\stackrel{(b)}{=} \frac{\mathbb{P}(\mathbf{V}(\{\max(T, \gamma_j)\}))}{\mathbb{P}(\mathbf{V}(\{\gamma_j\}))}, \\ &\stackrel{(c)}{=} \begin{cases} \frac{\sum_{j \in \{m, f\}} \lambda_j (P_T^j G_{\max}^j)^{2/\beta} \max(T, \gamma_j)^{-2/\beta}}{\sum_{j \in \{m, f\}} \lambda_j (P_T^j G_{\min}^j)^{2/\beta} \gamma_j^{-2/\beta}} & T > \gamma_j \\ 1 & \text{otherwise,} \end{cases} \end{aligned} \quad (3.33)$$

where γ_{\min} denotes $\min\{\gamma_m, \gamma_f\}$, (a) follows from Bayes' theorem, (b) follows from the assumption $\gamma_j > 1 \forall j$ and (c) follows from Proposition 2. We denote the random

variable $\max_{x \in \cup \Phi}(\gamma(x))$ by X , then \bar{R} is evaluated as follows

$$\begin{aligned}
\bar{R} &= \int_0^\infty \log(1+x) f_X(x | \mathbf{V}(\{\gamma_j\})) dx \\
&= \int_{x=0}^\infty \int_{y=0}^x \frac{1}{1+y} f_X(x | \mathbf{V}(\{\gamma_j\})) dy dx, \\
&\stackrel{(a)}{=} \int_{y=0}^\infty \left(\int_{x=y}^\infty f_X(x | \mathbf{V}(\{\gamma_j\})) dx \right) \frac{1}{1+y} dy \\
&= \int_0^\infty \frac{\mathbb{P}(X > y | \mathbf{V}(\{\gamma_j\}))}{1+y} dy,
\end{aligned} \tag{3.34}$$

where (a) follows from changing the order of integration. By substituting (3.33) in (3.34), we obtain the average rate under coverage as

$$\begin{aligned}
\bar{R} &= \int_0^{\gamma_{\min}} \left[\frac{1}{1+y} \right] dy \\
&\quad + \frac{1}{\sum_{j \in \{m, f\}} \lambda_j (P_T^j G_{\min}^j)^{2/\beta} \gamma_j^{-2/\beta}} \sum_{j \in \{m, f\}} \lambda_j (P_T^j G_{\max}^j)^{2/\beta} \int_{\gamma_{\min}}^\infty \max(x, \gamma_j)^{-2/\beta} dx, \\
&= \log(1 + \gamma_{\min}) \\
&\quad + \frac{1}{\sum_{j \in \{m, f\}} \lambda_j (P_T^j G_{\min}^j)^{2/\beta} \gamma_j^{-2/\beta}} \sum_{j \in \{m, f\}} \lambda_j (P_T^j G_{\max}^j)^{2/\beta} \int_{\gamma_{\min}}^\infty \max(x, \gamma_j)^{-2/\beta} dx.
\end{aligned} \tag{3.35}$$

This concludes the proof.

The second term in (3.31) shows that at different thresholds for the multi-tier μ Wave network, the average rate under coverage is density dependent at different thresholds ($\gamma_f \neq \gamma_m$). As mentioned in Section 3.1, since the multi-tier μ Wave links are deployed as the wireless backhaul, the rate under coverage is required to be separately calculated for μ Wave link in order to determine its suitability as a reliable wireless backhaul.

The computation of the average rate under coverage for each tier is not as straightforward as the coverage probability. This is due to the split of the constant term $\log(1 + \gamma_{\min})$.

Proposition 6 *The separated average coverage rate for each tier can be given as*

$$R_f^c = \frac{\lambda_f (P_T^f G_{\max}^f)^{2/\beta}}{\sum_{j \in \{m, f\}} \lambda_j (P_T^j G_{\max}^j)^{2/\beta} \gamma_j^{-2/\beta}} \left[\gamma_f^{-2/\beta} \log(1 + \gamma_{\min}) + \mathcal{A}(\beta, \gamma_f, \gamma_{\min}) \right], \quad (3.36a)$$

$$R_m^c = \frac{\lambda_m (P_T^m G_{\max}^m)^{2/\beta}}{\sum_{j \in \{m, f\}} \lambda_j (P_T^j G_{\max}^j)^{2/\beta} \gamma_j^{-2/\beta}} \left[\gamma_m^{-2/\beta} \log(1 + \gamma_{\min}) + \mathcal{A}(\beta, \gamma_m, \gamma_{\min}) \right]. \quad (3.36b)$$

Proof 6 *Given the HetNet average coverage rate as*

$$\bar{R} = \log(1 + \gamma_{\min}) + \frac{\sum_{i=1}^K \lambda_i (P_i G_{\max_i})^{2/\alpha} \mathcal{A}(\alpha, \gamma_i, \gamma_{\min})}{\sum_{i=1}^K \lambda_i (P_i G_{\max_i})^{2/\alpha} \gamma_i^{-2/\alpha}},$$

where

$$\mathcal{A}(\alpha, \gamma_i, \gamma_{\min}) = \int_{\gamma_{\min}}^{\infty} \frac{\max(\gamma_i, x)^{-2/\alpha}}{1 + x} dx.$$

Since $\mathcal{P}_f^c + \mathcal{P}_m^c = \mathcal{P}_\mu^c$, therefore $\frac{\mathcal{P}_f^c + \mathcal{P}_m^c}{\mathcal{P}_\mu^c} = 1$.

The first term in (3.31) can be written as

$$\log(1 + \gamma_{\min}) = \frac{\mathcal{P}_f^c \log(1 + \gamma_{\min})}{\mathcal{P}_\mu^c} + \frac{\mathcal{P}_m^c \log(1 + \gamma_{\min})}{\mathcal{P}_\mu^c}. \quad (3.37)$$

By substituting equation (3.5) of \mathcal{P}_μ^c , and equations (3.10a) of $\mathcal{P}_f^c, \mathcal{P}_m^c$, respectively, in (3.37), the first term in equations (3.36a) and (3.36b) is obtained. The second term in (3.31) can be divided into two independent parts for the 2 tier following the same assumption in Lemma 1. Therefore, (3.31) can be splitted into (3.36a) and (3.36b).

This concludes the proof.

Alternately, these two equations can be re-written with respect to the individual

probability of coverage $\mathcal{P}_f^c, \mathcal{P}_m^c$ and the total probability of coverage \mathcal{P}_μ^c , as follows

$$R_f^c = \frac{\mathcal{P}_f^c}{\mathcal{P}_\mu^c} \left[\log(1 + \gamma_{\min}) + \gamma_f^{2/\beta} \mathcal{A}(\beta, \gamma_f, \gamma_{\min}) \right], \quad (3.38a)$$

$$R_m^c = \frac{\mathcal{P}_m^c}{\mathcal{P}_\mu^c} \left[\log(1 + \gamma_{\min}) + \gamma_m^{2/\beta} \mathcal{A}(\beta, \gamma_m, \gamma_{\min}) \right]. \quad (3.38b)$$

Although the individual average rates under coverage were derived based on the assumption of different thresholds, we show that this split still holds for same thresholds. This can be proven by substituting $\gamma_f = \gamma_m = \gamma_\mu$ in (3.38), which results in

$$R_f^c = \frac{\mathcal{P}_f^c}{\mathcal{P}_\mu^c} \left[\log(1 + \gamma_\mu) + \gamma_\mu^{2/\beta} \mathcal{A}(\beta, \gamma_\mu, \gamma_\mu) \right], \quad (3.39a)$$

$$R_m^c = \frac{\mathcal{P}_m^c}{\mathcal{P}_\mu^c} \left[\log(1 + \gamma_\mu) + \gamma_\mu^{2/\beta} \mathcal{A}(\beta, \gamma_\mu, \gamma_\mu) \right]. \quad (3.39b)$$

3.3.4.2 ASE η_μ^c and EE Ω_μ^c Analysis

Proposition 7 *Under the assumption of $\gamma_j > 1$ [5], ASE and EE are strictly decreasing functions with respect to the threshold, thereby they can be maximised by choosing the lowest possible SIR threshold available in the system.*

Proof 7 *To have a comparison between our previous analysis in Section 3.3, we consider the case of same thresholds $\gamma_f = \gamma_m = \gamma_\mu$. Hence, the ASE and EE will be given as:*

$$\eta_\mu^c = \left[\lambda_f \mathcal{P}_f^c(\gamma_\mu) + \lambda_m \mathcal{P}_m^c(\gamma_\mu) \right] R_\mu^c(\gamma_\mu), \quad (3.40a)$$

$$\Omega_\mu^c = \frac{\left[\lambda_f \mathcal{P}_f^c(\gamma_\mu) + \lambda_m \mathcal{P}_m^c(\gamma_\mu) \right] R_\mu^c(\gamma_\mu)}{\sum_{j \in \{m, f\}} \lambda_j (P_{j0} + \Delta_j P_j)}, \quad (3.40b)$$

where all the parameters are defined previously in Section 3.3 and Table 3.1. By substituting (3.31) in (3.40), we obtain

$$\eta_\mu^c = \left[\lambda_f \mathcal{P}_f^c(\gamma_\mu) + \lambda_m \mathcal{P}_m^c(\gamma_\mu) \right] \left[\log(1 + \gamma_\mu) + \gamma_\mu^{2/\beta} \mathcal{A}(\beta, \gamma_\mu, \gamma_\mu) \right]. \quad (3.41)$$

After simplification, we obtain

$$\eta_\mu^c = \mathcal{C} \left[\gamma_\mu^{-2/\beta} \log(1 + \gamma_\mu) + \mathcal{A}(\beta, \gamma_\mu, \gamma_\mu) \right], \quad (3.42)$$

where $\mathcal{C} = (\lambda_f c_f + \lambda_m c_m)$,

and $c_j = \frac{\pi}{C(\beta)} \frac{\lambda_j (P_T^j G_{\max}^j)^{2/\beta}}{\sum_j \lambda_j (P_T^j G_{\min}^j)^{2/\beta}}$, where $j = \{f, m\}$. The rest of the notations are given in Table 3.1.

The derivative of η_μ^c with respect to γ_μ is given as

$$\partial \eta_\mu^c / \partial \gamma_\mu = -a \gamma_\mu^{-a-1} \log(1 + \gamma_\mu), \quad (3.43)$$

where $a = \frac{2}{\beta}$. Since $\gamma_\mu > 1$, $\partial \eta_\mu^c / \partial \gamma_\mu < 0$. Thus η_μ^c is a decreasing function.

3.4 Results

In this section, we compare the numerical results derived in Section 3.3 with the experimental results obtained using Monte-Carlo simulations. The values for the parameters used in simulation and analytical results are specified in Table 3.3.

Table 3.3 The values for parameters used in simulation and analytical results [5, 77].

Parameter	Value	Parameter	Value
total area	4 km ²	P_t^f	30 dBm
λ_m	2 /km ²	P_t^m	46 dBm
λ_f	50 λ_m	r_w	100 m or 150 m
λ_w	100 /km ²	N_0	-117 dBm/Hz
β	3	α_w^N	3.3
α_w^L	2	P_t^w	30 dBm

The coverage probability plots have the same behaviour to the work presented in [5], [80]. For ASE plots, similar curves have been obtained in [17] but for different system model and settings. The EE results are expected to behave as ASE, since both are related by a constant (power consumption) which is independent of the required threshold.

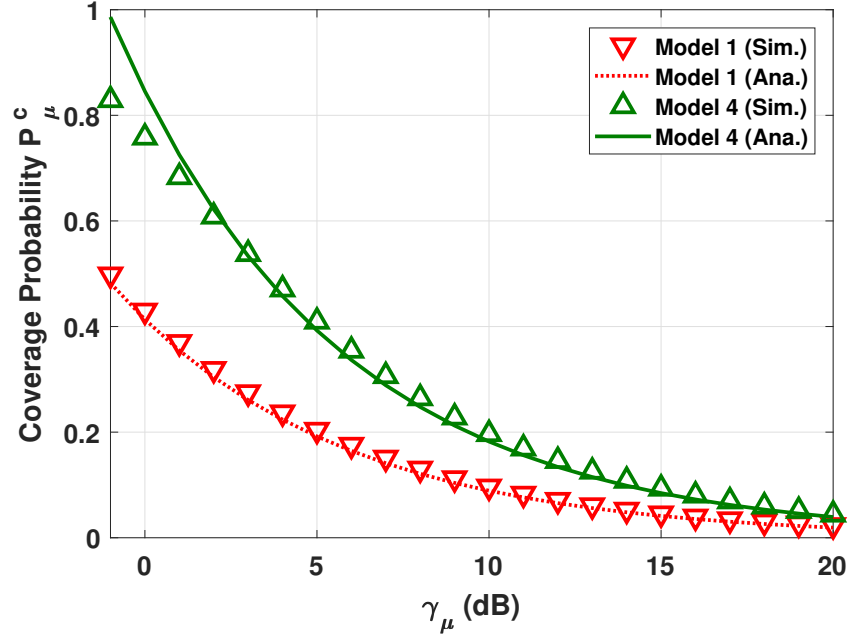


Figure 3.2 The coverage probability ($\mathcal{P}[SIR > \gamma_{\mu}]$) of μ Wave tiers for different SIR thresholds γ_{μ} for models 1 and 4.

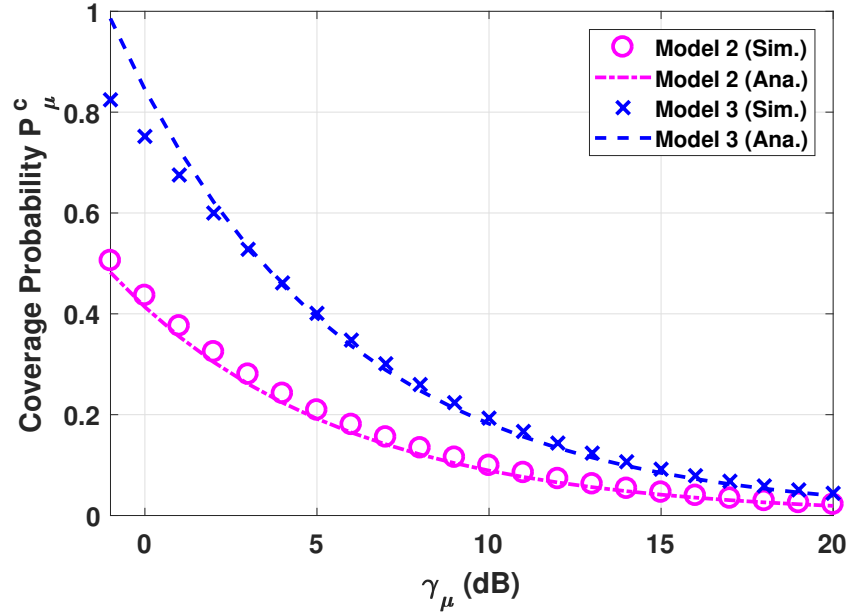


Figure 3.3 The coverage probability ($\mathcal{P}[SIR > \gamma_{\mu}]$) of μ Wave tiers for different SIR thresholds γ_{μ} for models 2 and 3.

As mentioned in Section 3.3.1.1.1, the model configurations presented in Table 3.2 enables us to show the effect of adding directional antenna at one or more tiers to improve the performance of the considered network.

For example, in Model 2 when the directional antenna is deployed at the FBSs only (assuming a random direction for the beam), we expect that the performance will be slightly better than Model 1. This is because in Model 1, all BSs use omnidirectional antennas, which increases the interference signal received by the typical pBS, leading to reduced SIR and hence reduced coverage probability.

However in Model 2, the use of directional antennas at FBSs results in lower interference to the typical pBS. In Model 3, directional antenna at the typical pBS receiver ensures that the amount of interference received is limited to the angular spread of the main lobe of the antenna. This in-turn increases the SIR and hence results in improved coverage. Similarly, further improvement can be obtained using Model 4 where both FBSs and pBS have directional antennas.

Since in Models 1 and 2 (3 and 4) pBSs are equipped with omni-directional (directional) antennas, respectively, we expect the results to be close results for Models 1 and 2 (3 and 4). It should be noted that although employing directional antennas improves performance, it incurs additional cost as stated in Section 2.2.2.1 in Chapter 2. Especially, in Model 3, directional antennas, for μ Wave and mmWave communication, equipped at the pBS cause more complexity, which would result in a physically unrealisable scenario. Hence, there is a trade-off between the cost and performance. To this end, we advocate the use of ESPAR as the directional antenna for the μ Wave communication.⁵ As a result, Model 3 is indeed physically realisable.

As in Chapter 2, for the analytical results, we do not use it as a switched beam antenna and choose the values for the maximum and average directivity gains approximately using the beampattern in one particular direction. Hence, there is a small difference between simulation and analytical results for the directional antennas.

⁵Note that our performance analysis holds for any sectorized directional antenna

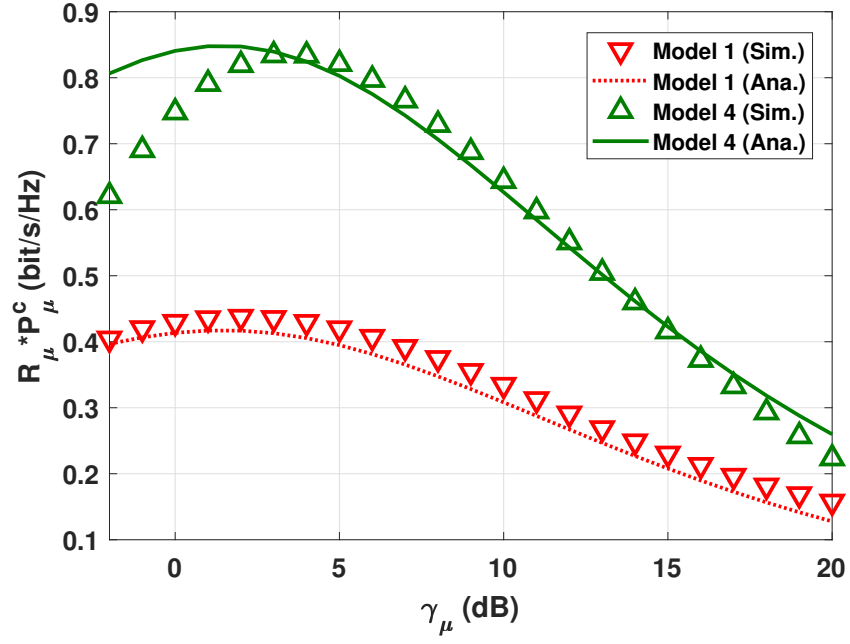


Figure 3.4 Average rate multiplied by Probability of Coverage ($R_\mu * P_\mu^c$) at different SIR threshold γ_μ for models 1 and 4.

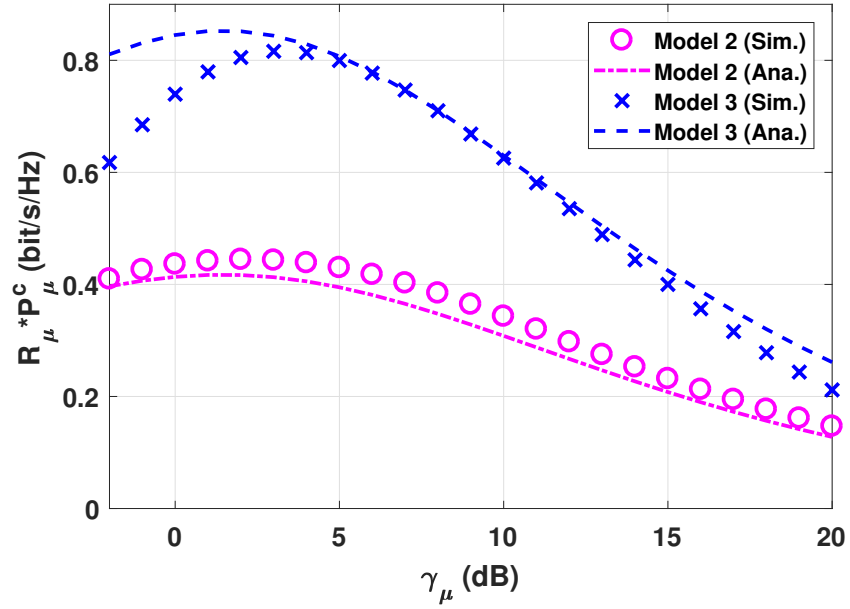


Figure 3.5 Average rate multiplied by Probability of Coverage ($R_\mu * P_\mu^c$) at different SIR threshold γ_μ for models 2 and 3.

In Figures 3.2, and 3.3, the coverage probability of the μ Wave is plotted with respect to the SIR threshold γ_μ comparing all four Models in Table 3.2. First from Fig. 3.2, we observe that Model 4 outperforms Model 1, resulting in higher coverage probability (almost double) at the typical pBS, as expected. In Fig. 3.3, we show the results for having the directional antenna at FBS (Model 2) and pBSs (Model 3), respectively. As identified before, the coverage probability of Model 1 is closer to Model 2 and Model 3 is close to Model 4.

3.4.1 μ Wave tiers

3.4.1.1 Results for minimum rate model analysis

In Figures 3.4 and 3.5, we present a plot for the overall average rate multiplied by the probability of coverage. This metric is considered as the ASE divided by the overall density of the μ Wave link. These results show a decrease as the required SIR threshold increases, because coverage probability decreases as the SIR threshold increases as shown in Figures 3.2 and 3.3. As expected, the results for Models 1 and 2 (3 and 4) are close.

The results of the optimisation problem of the ASE and EE for the wireless backhaul μ Wave tiers discussed in Section 3.3.3.1.1 are presented in Figures 3.6 and 3.7. According to the value of β defined in Table 3.3, and using (3.27), the analytical optimal SIR threshold $\gamma_\mu^* = 1.3970$ dB for all four models. As mentioned earlier, the slight difference in the simulation results with respect to analytical results (especially for Models 3 and 4) can be attributed to the way with which the analytical directivity gains was calculated.

3.4.1.2 Results for average rate under coverage

Following the analysis in Section 3.3.4, we present the results of the average rate under coverage multiplied by coverage probability, ASE and EE in terms of average rate under coverage. The results show that ASE and EE are decreasing function for $\gamma_\mu > 1$.

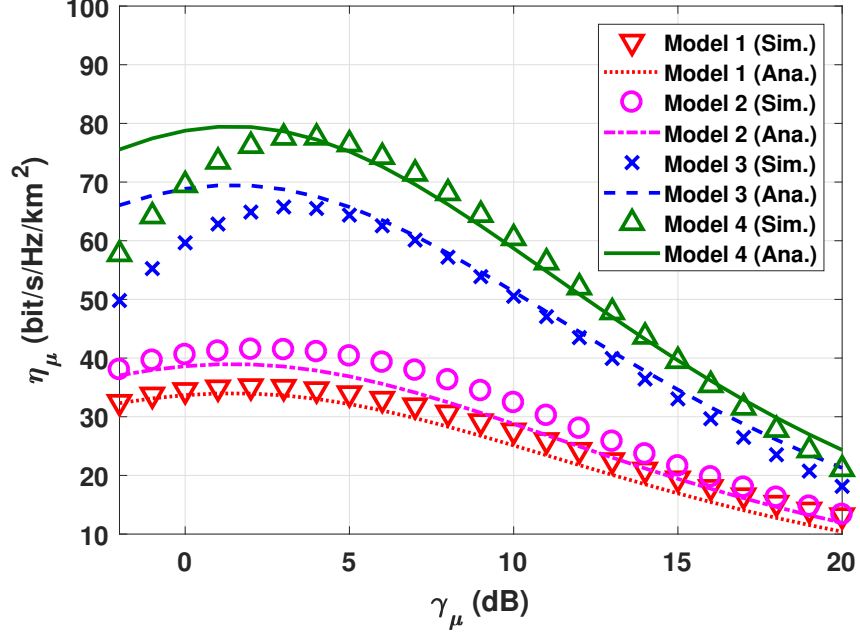


Figure 3.6 μ Wave link ASE η_μ for different SIR thresholds γ_μ .

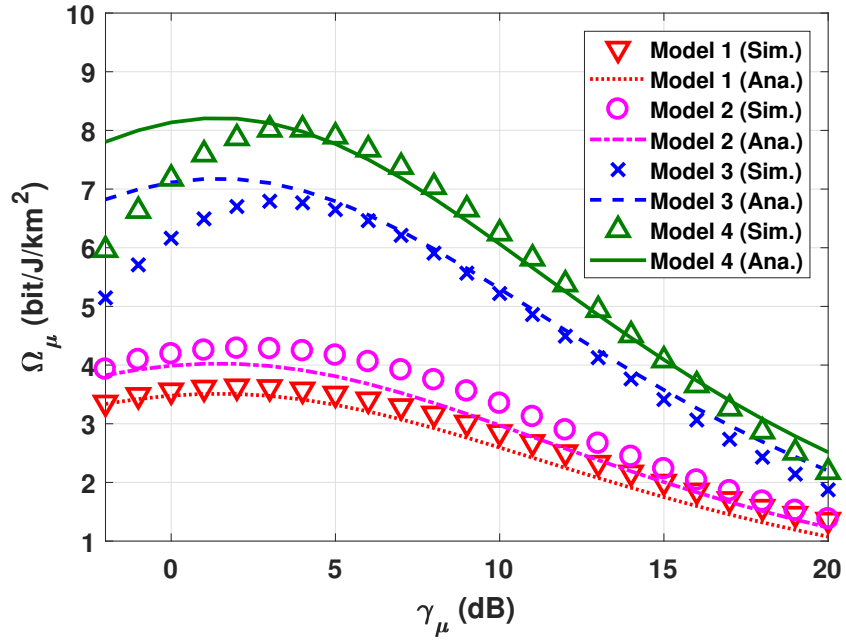


Figure 3.7 μ Wave link EE Ω_μ for different SIR thresholds γ_μ .

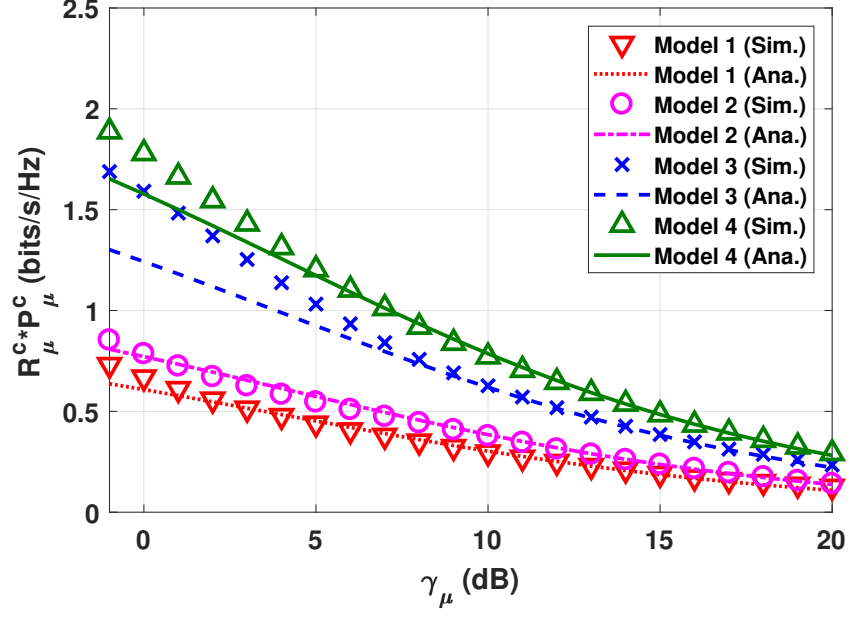


Figure 3.8 μ Wave rate under coverage multiplied by Probability of Coverage ($R_\mu^c * P_\mu^c$) at different SIR threshold γ_μ .

In Fig. 3.8, we present a plot for the overall average rate under coverage multiplied by the probability of coverage. This metric is considered as the average rate achievable by a random pBSs when it is in coverage. Fig. 3.8 shows a decrease as the SIR threshold increases, because coverage probability decreases as the threshold increases as shown in Figures 3.2 and 3.3.

As identified before, the way in which the analytical gain of ESPAR antenna was calculated might have resulted in the slight difference in the simulation results with respect to analytical results (especially for Models 3 and 4).

The coverage probability is the key parameter for calculating the ASE and EE. Therefore, we expect the same behaviour in Figures 3.2 and 3.3 for Figures 3.9 and 3.10. ASE and EE results presented in Figures 3.9 and 3.10 are considering the average rate under coverage. According to Proposition 7, the maximum ASE and EE occurs at $\gamma_\mu = 0$ dB. From these results, we conclude that the performance of the μ Wave tiers as wireless backhaul can be improved by exploiting directional antennas. This improvement depends on the placement of directional antenna on the transmitter and/or receiver.

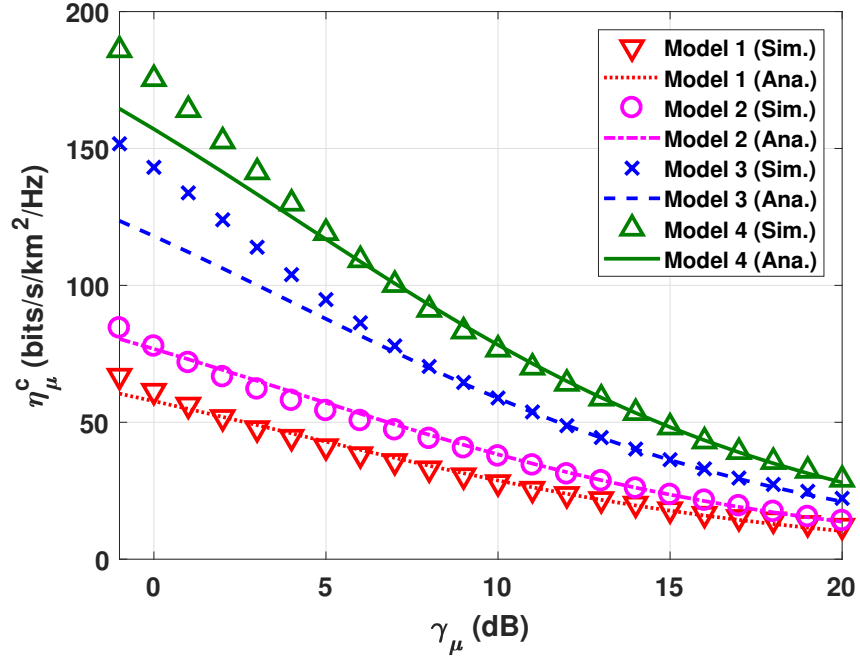


Figure 3.9 μ Wave tier ASE in terms of average rate under coverage for different SIR thresholds γ_μ .

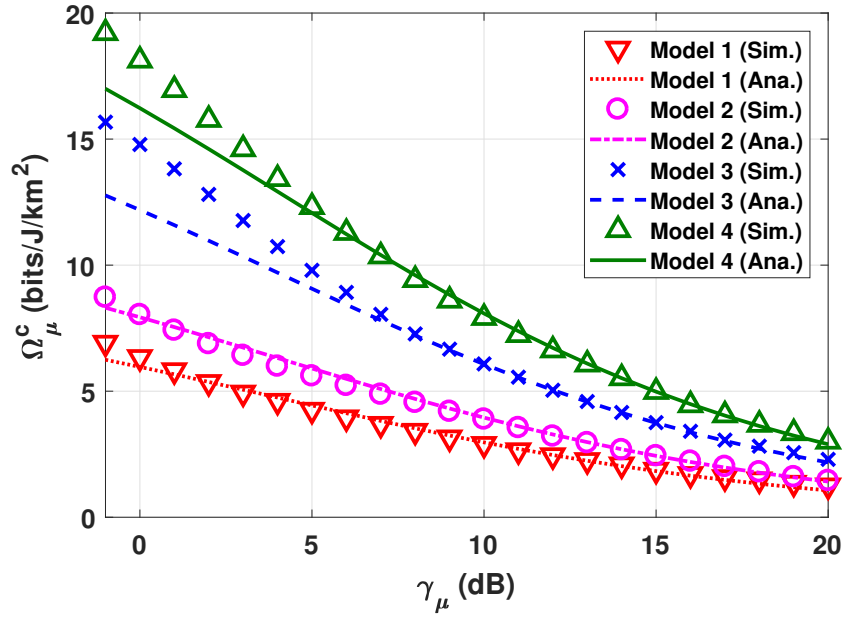


Figure 3.10 μ Wave tier EE in terms of average rate under coverage for different SIR thresholds γ_μ .

Moreover, the results in Figures 3.9 and 3.10 confirm what we stated in Proposition 7.

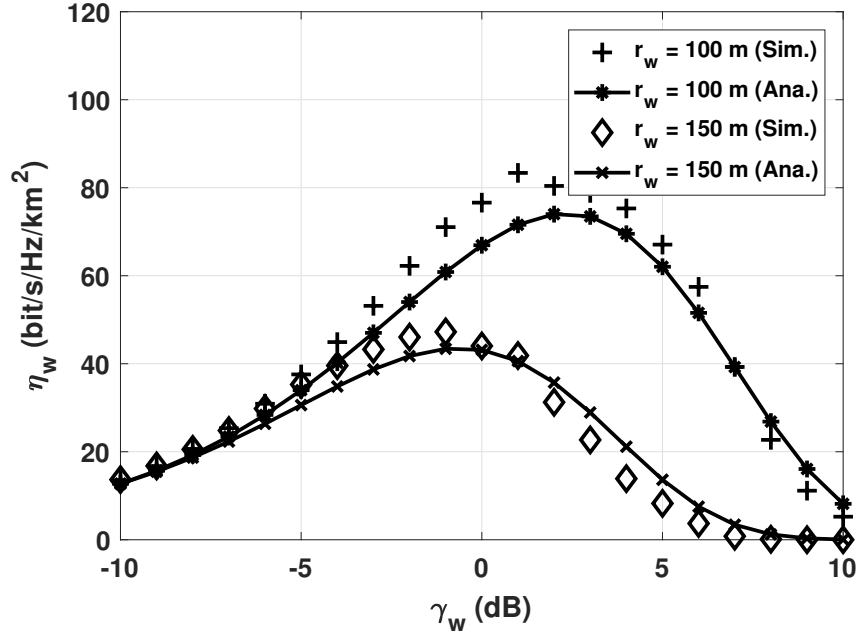


Figure 3.11 mmWave tier ASE η_w for different SINR thresholds γ_w .

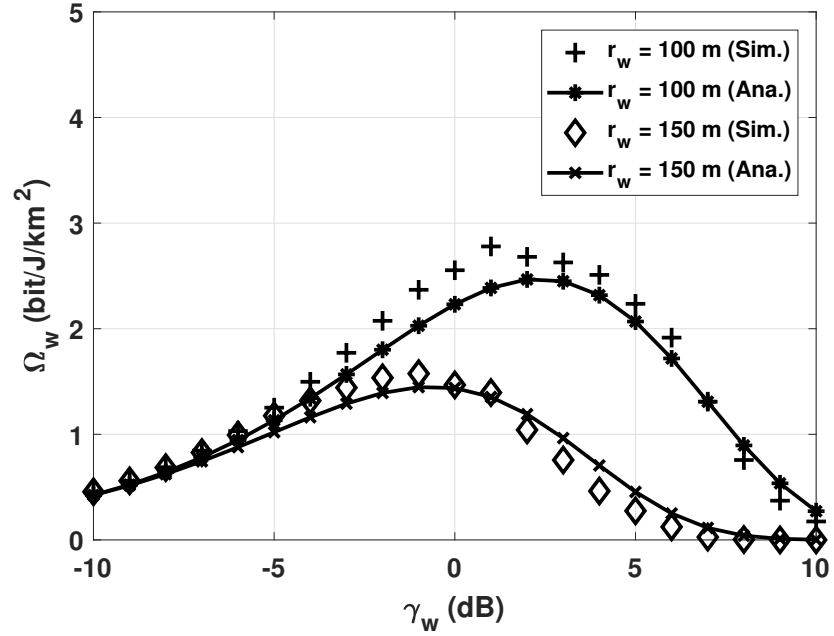


Figure 3.12 mmWave tier EE Ω_w for different SINR thresholds γ_w .

3.4.2 mmWave tier

In Figures 3.11 and 3.12, we present the results for ASE and EE of mmWave network γ_w . This plot is under the assumption that the distance between the desired pBS and UE is fixed. Although the optimisation problem explained in Section 3.3.3.1.2 didn't have a closed form, but the results show the dependence of the optimal SINR on the radius of LOS region. As the radius of the LOS region increases, more pBSs are considered LOS pBSs. This increase results in a smaller SINR threshold.

Thus, the curves for $r_w = 150\text{ m}$ have an optimal SINR threshold smaller than the case of $r_w = 100\text{ m}$. There is a slight difference between the simulation and analytical results. This is because of the accuracy of calculating the numerical integrations in (3.13).

3.5 Summary

As a summary for this chapter

- We considered a three-tier hybrid cellular HetNet using μ Wave links for the first two-tiers and mmWave links for the last tier. The μ Wave links were used as wireless backhaul to the last tier with mmWave links. It was assumed that the end-user could only connect to the last tier.
- Because the main challenge in having a wireless backhaul is mitigating interference, we proposed a novel and practical model where we reused the μ Wave infrastructure, and equipped the BSs with directional antennas to have a robust wireless backhaul network. Moreover, equipping the μ Wave tiers with directional antennas showed an improvement in the performance metrics, such as, coverage probability, average rate under coverage, ASE and EE. Furthermore, different placements for the directional antennas were presented, in order to have a robust wireless backhaul as well as an overall low system complexity.
- We studied an optimisation problem for the overall ASE and EE with respect to the optimal SIR threshold for μ Wave and mmWave links in terms of min-

imum rate model. The results indicated that the optimal threshold required for the μ Wave tiers (wireless backhaul) depends on the path-loss exponent and that for the mmWave tier depended on the area of LOS region.

- Furthermore, we studied the average rate under coverage, and its effect on ASE and EE. We proved that using the average rate under coverage model, the optimal threshold is the minimum, as ASE and EE are strictly decreasing functions. We concluded that the proposed hybrid HetNet model with μ Wave links as the wireless backhaul and mmWave based end-users can be made practically feasible for deployment with the appropriate choice/placement of directional antennas and with suitable setting of thresholds at different tiers.

Chapter 4

Wireless Ad-hoc Sensor Networks: Detection

In Chapters 2 and 3, we presented the performance analysis for single-tier and multi-tier HetNet cellular networks, respectively. However, as stated in Chapter 1 [Section 1.1], device-centric (ad-hoc) networks are of interest in future generations due to their requirements of low latency and wider spectrum. Furthermore, sensor networks are used in different areas for different applications such as metering, environment monitoring and localisation. 5G and the future generations are considering to benefit from localisation in wireless network design and optimisation [23]. Therefore, in this chapter, we study the localisability for wireless ad-hoc sensor networks. These networks are infrastructure-less, require minimal configuration and exhibit random topology, [25, 29, 38–40, 42, 43]. The first step in localisation is the detection process, where the sensor node detects the target's signal (i.e. the sensor node is covered by the target). In the literature, [87, 118], detection probability is defined according to a fixed scenario. A fixed scenario refers to the configuration of fixed sensors with fixed detection range; neglecting the channel variations and interference; where the "active" sensors are located. "Active" sensors are referred to as the sensors which are the closest to the target when channel variations (e.g. small-scale fading) are neglected. Then, these sensors successfully participate in the localisation process. However, in a practical scenario, random channel variations and all possible sensors

configurations should be considered for accurate detection and localisation analysis. The second step in the localisation process is the usage of the "active" sensors' range based measurements to localise the target node which is discussed in more detail in Chapter 5.

4.1 Introduction

In this chapter, we consider a three-dimensional MASNET consisting of a large number of inexpensive sensor nodes distributed over a large region. MASNET is typically used, for target detection and localisation to provide a greater level of situational awareness for units in the operational region. Although the number of sensors might be fixed, yet due to communication outage, node failure or blockage, the actual number of participating sensors in detection and localisation is random, which makes the analysis intractable. Therefore, in this chapter, we propose a tractable model to analyse the localisation performance metrics such as detection probability and S -localisability probability. S -localisability probability is defined as the probability that at least S sensor nodes detected the target's signal and successfully participated in the localisation procedure. Using the tools of stochastic geometry, we derive closed-form and easy-to-use expressions for these metrics. To accurately design a wireless ad-hoc sensor network that can be exploited in localisation, it is essential to know the minimum number of sensors that maximises the localisability. Towards that, we maximise the minimum S -localisability to obtain the optimal sensors' density λ_s^* . The results show that the MASNET must have λ_s^* sensors per unit volume for at least S sensors to be able to detect, .

To observe the utility of the expressions in a practical scenario, we consider a MASNET with a fixed number of sensors that are randomly located. First, it is shown that it is an NP-hard difficult to compute the aforementioned performance metrics for a large number of sensors. Second, the expressions, which are derived and averaged for random numbers and locations, accurately provide the performance metrics of the fixed network, which emphasises the benefits of the stochastic geometry tools.

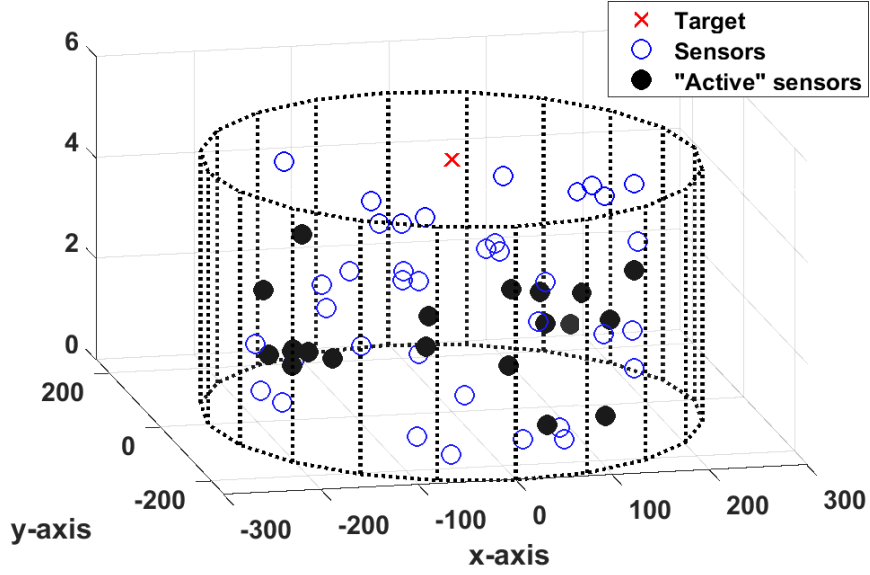


Figure 4.1 3-dimensional System Model MASNET with red cross as the typical target node, blue and black circles are sensors and "active" sensors, respectively.

4.2 System Model

We consider a three-dimensional region, where a target located in an unknown location communicates to a typical destination located at an unknown location. The sensors are scattered randomly in the region, following a PPP Φ_s with intensity λ_s , i.e., the locations of the sensors are independent and identically distributed (i.i.d.) uniformly over the region and the number of sensors (N), the cardinality of Φ_s , is a Poisson random variable with mean $\lambda_s|\mathcal{V}|$, where $|\mathcal{V}| = \pi R^2 h$ is the volume of the cylindrical region with R and h being the radius and height of the region, respectively as shown in Fig. 4.1.

This assumption reflects the practical nature of WSNs since the number of active sensors change randomly due to the communication outage and node failure. This is denoted in Fig. 4.1, where the black circles indicate the "active" sensors, i.e., the sensors that detected the transmitted target signal. This is the main difference between our work and the literature, wherein literature the number of sensors detected the target signal is assumed to be deterministic and defined according to a certain sensing (detection) range. However, in our work, we consider the number of "active"

Table 4.1 Summary of Notations

Symbol	Description
Φ_s	PPP
λ_s	Intensity of PPP
P_t	Transmit power
P_r	Received power
σ_n^2	Variance of noise
α	Path-loss exponent ($\alpha > 2$)
r_i	Distance from the i^{th} sensor node to the target
h_s	Small-scale fading channel
R	Radius of region of interest (ROI)
h	Height of ROI

sensors is random because we take into account the channel effects such as path-loss and small-scale fading.

Due to Slivnyak's theorem [57] and the stationarity of the homogeneous PPP, the target to be localised can be considered at the origin. Each sensor node, equipped by a single antenna, collects measurements from the transmission from the target.

The assumption of a single antenna per sensor is well-matched with the MASNET in military field applications where we use inexpensive sensors dropped in a certain region with large numbers.

In this chapter, first, we consider the target detection problem. In Chapter 5, we compute the localisation error using different range based localisation approaches.

Assuming Rayleigh fading, the received signal at s^{th} sensor, based on the presence of the target, can be written as a binary hypothesis testing problem as

$$\mathcal{H}_0 : y_s = n_s, \quad (4.1)$$

$$\mathcal{H}_1 : y_s = \frac{a h_s}{r_s^{\alpha/2}} + n_s, \quad (4.2)$$

where n_s is the additive white Gaussian noise (AWGN) with zero mean and σ_n^2 variance, a is the target's transmitted signal, $h_s \sim \mathcal{CN}(0, 1)$ and r_s^α are the small scale fading coefficient and the path loss governed by the exponent α , respectively.

Under the sufficient statistics $(|y_s|^2)$ with the threshold γ_{th} , the false alarm and

detection probabilities at each sensor are obtained as [119],

$$p_f = e^{-\frac{\gamma_{th}}{\sigma_n^2}}, \quad (4.3)$$

$$p_d = e^{-\epsilon r_s^\alpha}, \quad (4.4)$$

where $\epsilon = \frac{\gamma_{th} - \sigma_n^2}{\mathbb{E}[a^2]}$.

After the target detection, each sensor node forwards its decision to the FC, which fuses these decisions using a fusion method such as OR-rule to provide the final decision. In the following section, we analyse the detection performance at the FC for the PPP based sensor network.

4.3 Performance Analysis

For a target detection problem, at least one sensor is enough to detect the presence of a target. But for a target localisation problem, a minimum number of sensors is required to detect the location of the target. This minimum number depends on the localisation technique (AoA, ToA, TDoA) and the dimensional space (2D or 3D). For example, the minimum numbers of "active" sensor nodes S in \mathbb{R}^2 are 2, 3 and 4 for AoA, ToA and TDoA, respectively. While for \mathbb{R}^3 , we need 3, 4 and 5 "active" sensor nodes for AoA, ToA and TDoA, respectively. To combine the sensors' decisions, we assume OR-rule at FC and compute the probability when at least S sensors detect the target.

4.3.1 Detection Probability Analysis

As a start for the detection analysis, we consider the hard-decision detection because it is simple and will provide us with some useful information through the closed-form expressions derived. However, for the future work, we plan to analyse also the soft-decision detection as stated in Chapter 6 [Section 6.2]. Because, in literature, soft-decision is known to outperform the hard-decision but the disadvantage of soft-decision is that it requires huge bandwidth, large delay and complex analysis at the

FC. The detection probability of the network at the FC is defined as the probability that at least one sensor detects the target's transmission. From (4.4), we observe that the detection probability for each sensor depends on the distance between the sensor node and the typical target r_s . Under the assumption of a PPP network, this parameter is a random variable.

Proposition 8 *Hence the detection probability of the considered network is expressed as*

$$P_d = 1 - \exp(-v), \quad \text{where} \quad v = \frac{2\pi\lambda_s h}{\alpha} \epsilon^{\frac{-2}{\alpha}} \Gamma\left(\frac{2}{\alpha}, \epsilon R^\alpha\right), \quad (4.5)$$

$\Gamma(.,.)$ in the lower incomplete Gamma function and the rest of the notations are in Table 4.1.

Proof 8 *The probability of detection at the FC is defined as the probability that at least one sensor detects the target's transmission given that the target transmits \mathcal{H}_1 . This can be written mathematically as,*

$$\begin{aligned} P_d &= \mathbb{P}(\text{at least one sensor heard} | \mathcal{H}_1), \\ &\stackrel{(a)}{=} \mathbb{E}_\Phi \left[1 - \prod_{i \in \Phi} (1 - p_d^i) \right] \\ &= 1 - \mathbb{E}_\Phi \left[\prod_{i \in \Phi} (1 - p_d^i) \right], \\ &\stackrel{(b)}{=} 1 - \exp \left(- \int_{\mathbb{R}^3} \lambda_s (1 - (1 - p_d^i)) d\mathbf{x} \right), \\ &\stackrel{(c)}{=} 1 - \exp \left(- \int_0^{2\pi} \int_0^h \int_0^R \lambda_s \exp(-\epsilon r^\alpha) r dr dp d\theta \right), \\ &\stackrel{(d)}{=} 1 - \exp \left(-2\pi\lambda_s h \int_0^R \exp(-\epsilon r^\alpha) r dr \right), \end{aligned} \quad (4.6)$$

where (a) follows from the Binomial distribution [120], (b) follows the PGFL given in Appendix A [57], (c) follows the substitution of (4.4), (d) follows the computation of the 3-D integral and the closed-form expression is denoted as given in (4.5).

This concludes the proof.

The above expression shows that increasing the density improves detection performance. Also for the 3-D model, the height h has the same impact as the sensors' density λ_s .

Similarly, the false alarm probability P_f of the network obtained at the FC is defined as the probability that at least one sensor detects the target given that the target did not transmit.

Proposition 9 *From (4.3), we observe that the false alarm probability of each sensor is fixed and dependent on the threshold and the noise variance σ_n^2 and is given as*

$$P_f = 1 - e^{-\pi\lambda_s h R^2 p_f}, \quad (4.7)$$

where p_f is defined in (4.3).

The false alarm probability of the considered network P_f depends on the mean parameter of the PPP $\lambda_s|\mathcal{V}|$ and the false alarm probability of each sensor which we assume is the same for all sensors. This assumption is valid as we assume a homogeneous sensor network, however, a heterogeneous sensor network is an interesting problem that we can consider in our future work.

Proof 9 *The false alarm probability P_f of the network can be computed following the same steps given in Proof 8 as*

$$\begin{aligned} P_f &= 1 - \exp\left(-\int_{\mathbb{R}^3} \lambda_s (1 - (1 - p_f)) d\mathbf{x}\right) \\ &= 1 - \exp\left(-\int_0^{2\pi} \int_0^h \int_0^R \lambda_s p_f r dr d\theta\right) \\ &= 1 - \exp\left(-\lambda_s \pi R^2 h e^{-\frac{\gamma_{th}}{\sigma_n^2}}\right), \end{aligned} \quad (4.8)$$

This concludes the proof.

It can be noted that the detection problem depends on the chosen threshold. From the above expressions (4.3) and (4.8), the threshold can be chosen using either false alarm probability of each sensor p_f or the false alarm probability of the considered network P_f . Since the probability of detection of the network is composed

of the detection probability decisions from each sensor, it is reasonable to define the threshold for each sensor to get a fixed local false alarm probability, given as

$$\gamma_{\text{th}} = -\sigma_n^2 \ln(p_f), \quad (4.9)$$

which depends only on the noise power. However, intuitively, the threshold should change based on the density of the sensors to keep the false alarm probability of the network within a limit. Therefore, the threshold to keep the false alarm probability of the network fixed can be obtained as

$$\gamma_{\text{th}} = -\sigma_n^2 \ln \left(\ln \left(\frac{\ln(1 - P_f)}{-\pi \lambda_s h R^2} \right) \right), \quad (4.10)$$

which depends not only on intensity λ_s , but also depends on the volume of the cylindrical region \mathcal{V} , representing the global applicability of the threshold in the network. For the rest of the chapter, we consider the threshold based on the individual false alarm probability of each sensor.

4.3.2 S -localisability probability

To detect the presence of the target, the detection probability was discussed in Section 4.3.1. However, in practice, to get a rough estimate about the localisation metrics, the measurements from multiple sensors are required. In this section, we analyse the S -localisability probability P_L^S which is defined as the probability that at least S sensors detect the target and participate in the localisation procedure. For a fixed sensor network, choosing S out of the total number of sensors is an NP-hard problem. Moreover, considering random location in the PPP network, it adds to the difficulty of the S -localisability probability analysis.

Proposition 10 *The S -localisability probability is defined as the probability that at least S sensors detected the target's signal and successfully participate in the*

localisation. Mathematically, expressed as

$$P_L^S = 1 - \sum_{k=0}^{S-1} \frac{v^k}{k!} e^{-v}, \quad (4.11)$$

where v is defined in (4.5).

Proof 10 According to the definition of P_L^S , mathematically it can be denoted as

$$\begin{aligned} P_L^S &= \mathbb{P}(\text{at least } S \text{ sensors heard}) \\ &= 1 - \sum_{k=0}^{S-1} \mathbb{E}_{\Phi_s} [\mathbb{P}(A_k)], \\ &\stackrel{(a)}{=} 1 - \sum_{k=0}^{S-1} \frac{v^k}{k!} e^{-v}. \end{aligned} \quad (4.12)$$

where v is given in (4.5), (a) follows from the derivation of $\mathbb{E}_{\Phi_s} [\mathbb{P}(A_k)]$ which is provided in Section 4.4.

This concludes the proof.

The above result shows that the chances of the presence of S "active" sensors are Poisson distributed with the mean proportional to the sensors' density, height and threshold. Note that the height plays the same role as the density in finding the sensors, which shows the importance of the 3-D model considered.

Remark 1 We observe that the detection probability P_d is equal to the S -localisability probability when $S = 1$. This can be verified by comparing (4.5) to (4.12)| $_{S=1}$ and also through the P_d and P_L^S plots in Figures 4.2 and 4.4, respectively.

4.4 Optimal density for S -localisability

Based on the dependence of density, a natural question arises what should the density be to guarantee S "active" sensors. The answer to this question is given in Proposition 12, but before that, we need to compute the minimal S -localisability probability as shown in Proposition 11.

$$\begin{aligned}
\mathbb{E}_{\Phi_s} [\mathbb{P}(A_k)] &\stackrel{(a)}{=} \mathbb{E}_{\Phi_s} \left[\sum_{\substack{U \subseteq \Phi_s \\ |U|=k}} \left[\prod_{u \in U} \zeta_{i_u} \prod_{u \in \Phi_s \setminus U} (1 - \zeta_j) \right] \right], \\
&= \mathbb{E}_{\Phi_s} \left[\frac{1}{k!} \sum_{i_1 \in \Phi_s} \dots \sum_{i_k \in \Phi_s \setminus \{i_1, \dots, i_{k-1}\}} \left[\prod_{l=1}^k \zeta_{i_l} \prod_{j \in \Phi_s \setminus \{i_1, \dots, i_k\}} (1 - \zeta_j) \right] \right], \\
&\stackrel{(b)}{=} \frac{1}{k!} \left[\int_{\mathbb{R}^3} \dots \int_{\mathbb{R}^3} \int_{\mathcal{N}_k} \prod_{l=1}^k \zeta_{i_l} \right. \\
&\quad \left. \prod_{j \in \Phi_s \setminus \{i_1, \dots, i_k\}} (1 - \zeta_j) \Lambda(d\mathbf{x}_1) \dots \Lambda(d\mathbf{x}_k) \mathcal{P}_{x_1, \dots, x_k}(\Phi_s) \right], \\
&= \frac{1}{k!} \int_{\mathbb{R}^3} \dots \int_{\mathbb{R}^3} \prod_{l=1}^k \zeta_{i_l} \Lambda(d\mathbf{x}_1) \dots \Lambda(d\mathbf{x}_k) \\
&\quad \left[\int_{\mathcal{N}_k} \prod_{j \in \Phi_s \setminus \{i_1, \dots, i_k\}} (1 - \zeta_j) \mathcal{P}_{x_1, \dots, x_k}(\Phi_s) \right], \\
&\stackrel{(c)}{=} \frac{1}{k!} \prod_{l=1}^k \left[\int_{\mathbb{R}^3} \zeta_l \Lambda(d\mathbf{x}_l) \right] \mathbb{E}_{\Phi_s}^! \left[\prod_{j \in \Phi_s} (1 - \zeta_j) \right], \\
&\stackrel{(d)}{=} \frac{1}{k!} \left[\int_{\mathbb{R}^3} \zeta_l \Lambda(d\mathbf{x}_l) \right]^k \mathbb{E}_{\Phi_s} \left[\prod_{j \in \Phi_s} (1 - \zeta_j) \right] = \frac{v^k}{k!} e^{-v}. \tag{4.14}
\end{aligned}$$

Proposition 11 *We define minimal S -localisability probability, which is the probability that exact S sensors participate in the localisation procedure, and is given as*

$$P_{L_{\min}}^S = \mathbb{E}_{\Phi_s} [\mathbb{P}(A_k)] = \frac{v^k}{k!} e^{-v}, \quad [k = S], \tag{4.13}$$

where v is given in (4.5).

Proof 11 *We state $\mathbb{E}_{\Phi_s} [\mathbb{P}(A_k)]$ as given in (4.14), where (a) follows from Corollary 1 in [121], (b) follows from the proof of Theorem 1 in [121], (c) follows from Lemma 1 in [122] and (d) follows from the Slivnyak's theorem [57].*

This concludes the proof.

Given the sensors' density and the sensors' thresholds, the minimal localisability expresses the occurrence of S "active" sensors. Therefore, assuming the fixed detec-

tion threshold, we can maximise the minimal S -localisability to obtain the optimal sensors' density λ_s^* . Proposition 12 expresses this result.

Proposition 12 *The optimal sensors' density to obtain S -localisable sensors is*

$$\lambda_s^* = \frac{\alpha S \epsilon_\alpha^{\frac{2}{\alpha}}}{2\pi h \Gamma\left(\frac{2}{\alpha}, \epsilon R^\alpha\right)}, \quad (4.15)$$

where the notations are stated in Table 4.1.

Proof 12 *The optimisation problem can be formulated as the following*

$$\begin{aligned} \underset{\lambda_s}{\text{maximize}} \quad & P_{L_{\min}}^S(\lambda_s) = \frac{v^S(\lambda_s)}{S!} e^{-v(\lambda_s)} \\ \text{subject to} \quad & \lambda_s |V| \geq S, \end{aligned} \quad (4.16)$$

where $v(\lambda_s)$ is defined in (4.5). Using the Lagrangian function, we get

$$\mathbb{L}(\lambda_s) = -\frac{v^S(\lambda_s)}{S!} e^{-v(\lambda_s)} - \rho[\lambda_s |V| - S], \quad (4.17)$$

where ρ is the Lagrange multiplier. The derivative of the Lagrangian function with respect to λ_s is computed as :

$$\frac{\partial \mathbb{L}}{\partial \lambda_s} = \frac{e^{-v(\lambda_s)}(S - v(\lambda_s))v^{S-1}(\lambda_s) \frac{\partial v(\lambda_s)}{\partial \lambda_s}}{S!} - \rho |V| \quad (4.18)$$

Using the KKT conditions, and in particular the complementary slackness condition, $\rho[\lambda_s |V| - S] = 0$, we obtain the optimal $v^* = S$ and due to the linear relation between v and λ_s . The optimal λ_s^* can be found as

$$\lambda_s^* = \frac{\alpha S \epsilon_\alpha^{\frac{2}{\alpha}}}{2\pi h \Gamma\left(\frac{2}{\alpha}, \epsilon R^\alpha\right)} \quad (4.19)$$

This concludes the proof.

This result shows that to get S "active" sensors, the density should scale with S . Also if the height increases the density decreases. It implies that with the proper

Table 4.2 The values for parameters used in simulation and analytical results.

Parameter	Value
R	200 m
h	5 m
α	3
$\mathbb{E}[a^2]$	1, 0.1
Noise power	-30 dBm

3-D modelling, the requirement on the number of sensors can be reduced, which is important to reduce the cost of the sensor network.

4.5 Results

In this section, we compare the numerical results derived in Sections 4.3 and 4.4 with the simulation results. The values for the parameters used are specified in Table 4.2.

4.5.1 PPP Model

Fig. 4.2 plots the global probability of detection with respect to the sensors' density for different local false alarm probabilities, assuming local detection threshold expressed in (4.9). It can be observed that the analytical results agree with the simulations. It can be noted that increasing either the false alarm probability, the transmission power, or the density, the detection probability increases. A similar observation can be seen from Figure 4.3, where the detection probability versus the false alarm probability is plotted by varying the sensors' density λ_s . Figure 4.4 depicts the S -localisability probability versus the sensors' density for different values of S . We observe that the localisability probability increases with the sensors' density, which is the same behaviour in Fig. 4.2.

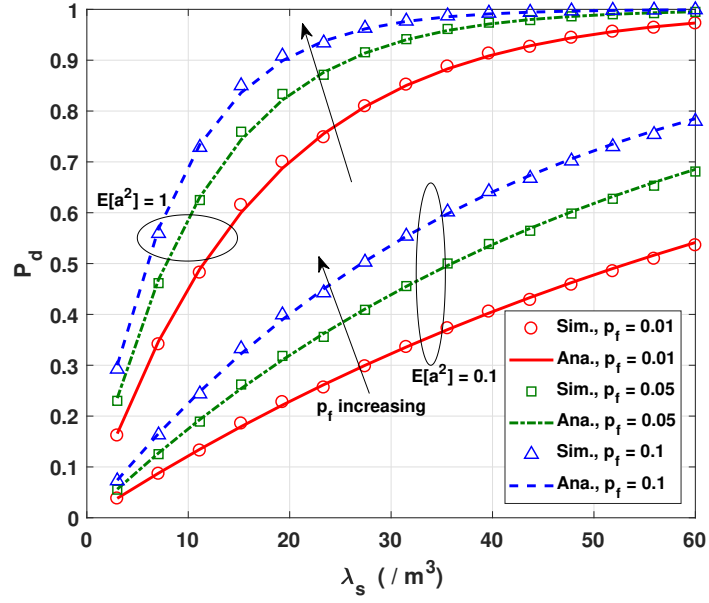


Figure 4.2 The probability of detection P_d with respect to the intensity of the PPP of the sensors λ_s at different false alarm probabilities and different transmit power $\mathbb{E}[a^2]$.

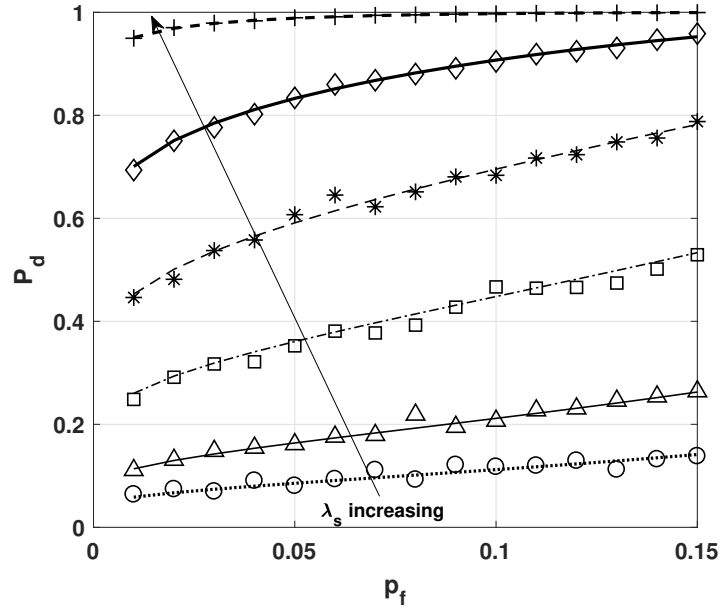


Figure 4.3 The probability of detection P_d with respect to the false alarm probability p_f at different intensities λ_s . Markers are the simulation results and the lines are the analytical results.

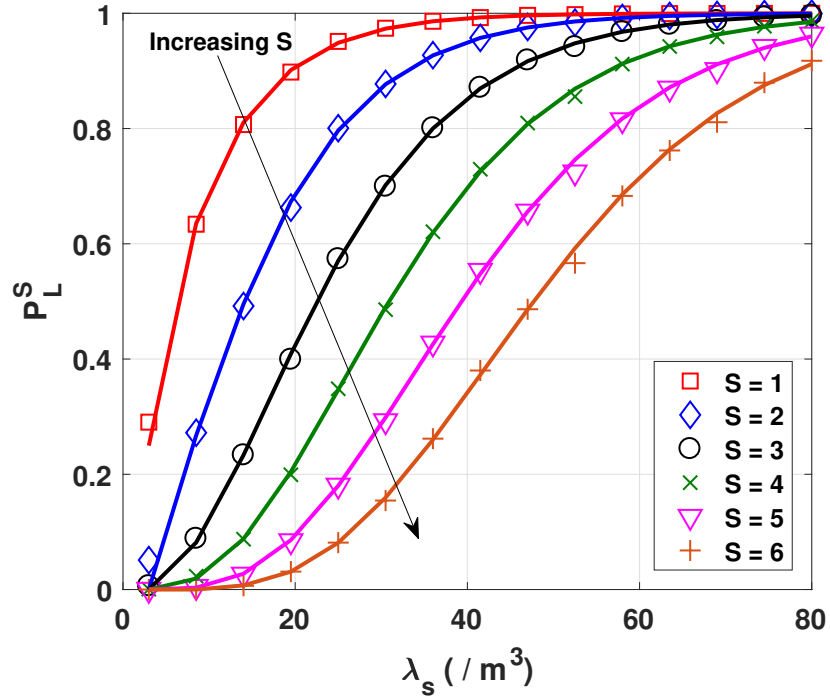


Figure 4.4 The S -localisability probability P_L^S with respect to the intensity of the PPP of the sensors λ_s .

But for a fixed density, we notice that the localisability probability decreases with the increase in S sensors (see (4.12)). This is because, for a fixed sensors' density (λ_s), the probability for more "active" sensors to reach a consensus decreases as the S increases (the set $\{S, S+1, S+2, \dots, N\}$ decreases).

This result can also be observed in Figure 4.5, which plots the minimal S -localisability probability for the density λ_s . As S is increasing, the peaks can be seen to be reducing. Figure 4.5 points the optimal density which maximises the S -localisability. Moreover, the optimal densities from the analytical and simulation are compared in Table 4.3. It can be seen that the analytically optimised density fits well with simulations. For the present settings, the optimal density can be regarded as a lower bound on the minimum number of sensors needed to obtain the S -localisability probability greater than 0.5 ($P_L^S \geq 0.5$).

For example, it can be verified by inserting the optimal intensity λ_1^* in Figure 4.4 and conclude that $\lambda_1^* \approx 9$, i.e., at least 9 sensors per meter cubed are needed for a detection probability ($(P_d \equiv P_L^1)$ as stated in Remark 1) greater than 0.5. This is

an interesting result as it provides an insight about the required number of sensors which is a crucial part of a localisation procedure.

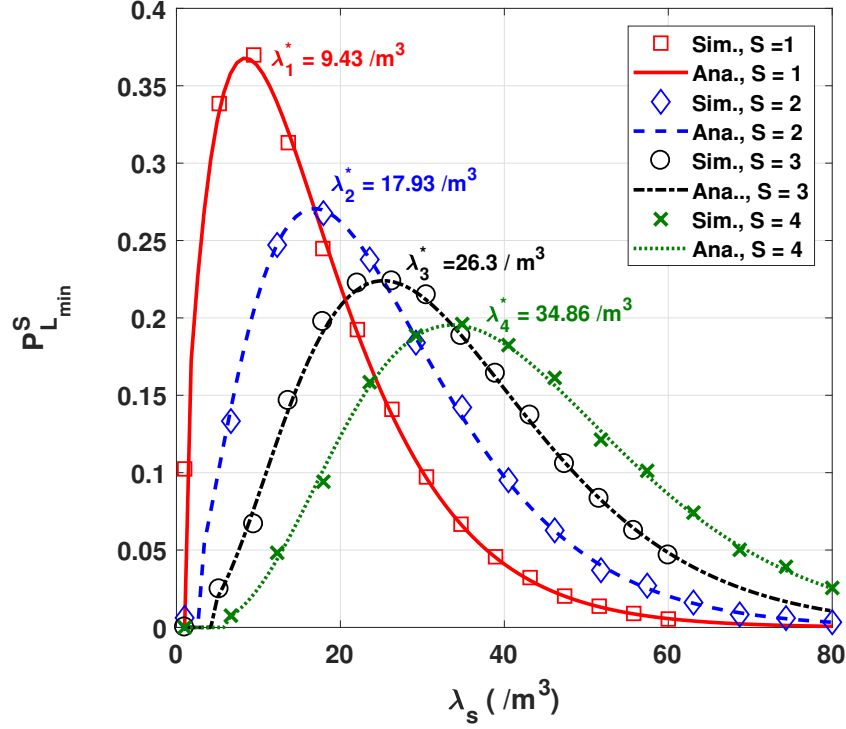


Figure 4.5 The minimal S -localisability probability $P_{L_{\min}}^S$ with respect to intensity of the PPP of the sensors λ_s

Table 4.3 The optimal intensities λ_s^*

S	$\lambda_{\text{Ana.}}^* (\backslash m^3)$ (4.19)	$\lambda_{\text{Sim.}}^* (\backslash m^3)$ (Figure 4.5)
1	8.4	9.4
2	16.8	17.9
3	25.2	26.3
4	33.6	34.86

4.5.2 Fixed Model

To this end, we presented the detection performance results averaged over the random PPP networks. In Figure 4.6, we present the same performance results considering a fixed network [5], where the fixed locations are assumed for a fixed number of sensors over the same cylindrical region as the PPP network above. In other words,

this fixed scenario can be regarded as an instance of the PPP network. Figure 4.6 demonstrates the agreement of the analytical results for the PPP network with the fixed one. It concludes that the PPP assumption is fairly accurate for the practical sensor networks. Moreover, it can be observed from equation (4.14) that analytically for the fixed scenario, it is computationally intensive process to compute the global probabilities due to the requirement for the search of all the possible S -combinations of sensors out of the total number of sensors (N). Therefore, it highlights the effectiveness of stochastic geometry in the analysis of the performance metrics such as detection probability and S -localisability probability for the practical networks.

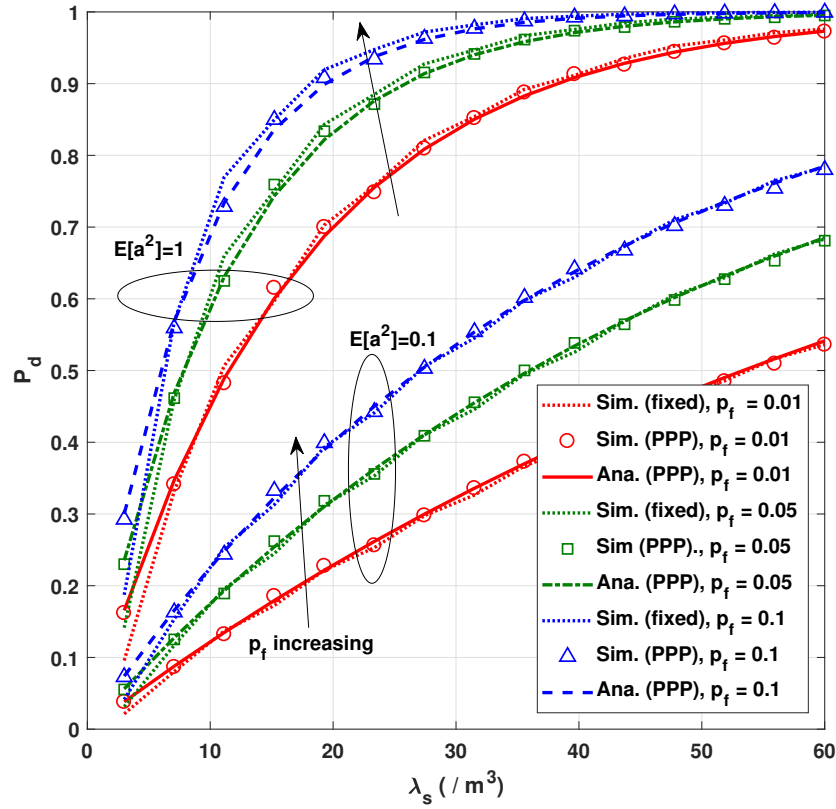


Figure 4.6 The probability of detection P_d with respect to the false alarm probability p_f at different intensities λ_s .

4.6 Summary

To summarise this chapter, we analysed the detection and localisability performance of a 3-D MASNET. We assumed that the sensors' positions are modelled as a PPP and a typical target that is located at the origin. Due to Slivnyak's theorem, the location of the target will not affect the results of the analysis. However, in the next chapter, we assume an unknown target location.

In practice, the active number of sensors that participate in detection and localisation vary randomly due to communication outage, blockage and node failure.

Therefore, we proposed a tractable approach for the analysis of the performance metrics such as detection probability and S -localisability probability for the considered network. S -localisability probability refers to the probability that at least S sensors detect that target's signals and successfully participate in the localisation. As expected, the detection and S -localisability probabilities increased as the density of the network increased. However, for a fixed density, we showed that the S -localisability probability metric decreased as the number S increased, this is because the probability to have S sensors detecting the target at the same time decreased as S increased.

As seen from the results, these defined metrics are increasing functions for the density λ . Thus, we considered the minimal S -localisability probability, which refers to having *exact* S sensors that can detect the target and successfully participate in the localisation process. Using this metric, we proposed an optimisation problem to find the optimal density of sensors required to maximise the minimal S -localisability probability. We showed an analytical expression for the optimal density λ_s^* that depends on S sensors, height and radius of the PPP region, path-loss exponent α and the threshold. Moreover, in the results, we showed that the optimal density computed analytically fits with the simulations.

Finally, we considered a fixed model, which represents a single instance of the PPP network. For the fixed model, the number of sensors and their locations are fixed over the cylindrical region. Simulation results have verified the analytical

results and demonstrated that for a fixed MASNET the performance metrics have the same behaviour as the analysed ones. However, obtaining the numerical results for the fixed model is computationally complex, thereby concluding the benefit of the stochastic geometry tools in deriving closed-form and easy-to-use expressions. Furthermore, using the fixed model, a comparison between different range based localisation algorithms will be presented in Chapter [5](#).

Chapter 5

Wireless Ad-hoc Sensor Networks: Localisation

In Chapter 4, we discussed the localisation analysis for ad-hoc sensor networks, in terms of the detection and localisability probabilities. These probabilities give an intuition about the number of active nodes that detected the target's signal and successfully participate in localisation. Furthermore, in this chapter, we focus on the analysis of the localisation error concerning the number of active nodes participating in the localisation procedure and not on localisation algorithms. In literature, extensive research has been conducted on different localisation algorithms using range-based or range-free techniques as discussed in Chapter 1. However, less research is related to the analysis of the minimum number of active nodes participating in the localisation procedure. Thus, this motivated us to analyse the minimum number of sensor nodes required to participate in localisation and use these sensors' measurements in the conventional localisation algorithms presented in literature. Specifically, we compute the localisation error for urban and rural environments using a centralised range based localisation techniques relying on the distance measurements based on ToA and TDoA. We define the localisation error as the distance difference between the estimated target location and the actual (typical) target location which is assumed to be at the origin. Please note that this analysis also holds for any random target location. In localisation literature, as shown in Chapter 1 (Table

1.1), there is always a trade-off between complexity and performance of different localisation techniques. Thus, we choose ToA and TDoA which are less complex techniques that results in acceptable performance as demonstrated by the results of this chapter.

5.1 Introduction

As stated in Chapter 1, localisation techniques can be classified into two categories. First, range-based techniques rely on measurements of distances between nodes that are often based on received signal strength (RSS) [47], ToA [42, 50, 123], and TDoA [51, 52]. Second, range-free techniques [124], on the other hand, rely on knowledge of connectivity possibilities, i.e., who is connected to whom, to ascertain locations. Furthermore, localisation can adopt a distributed approach, where the sensors perform many calculations and analysis to locate the target node (i.e the node that needs to be localised), or a centralised approach where sensors perform limited analysis. For the latter case, there is a greater instance of sensors simply forwarding information to a central sensor or FC, which can be a CH from one of the sensors. The FC fuses the local decisions via a global fusion rule to reach a global decision about the target. This structure is suboptimal, however other strategies would have a higher communication (energy) cost [54]. In this chapter, we con-

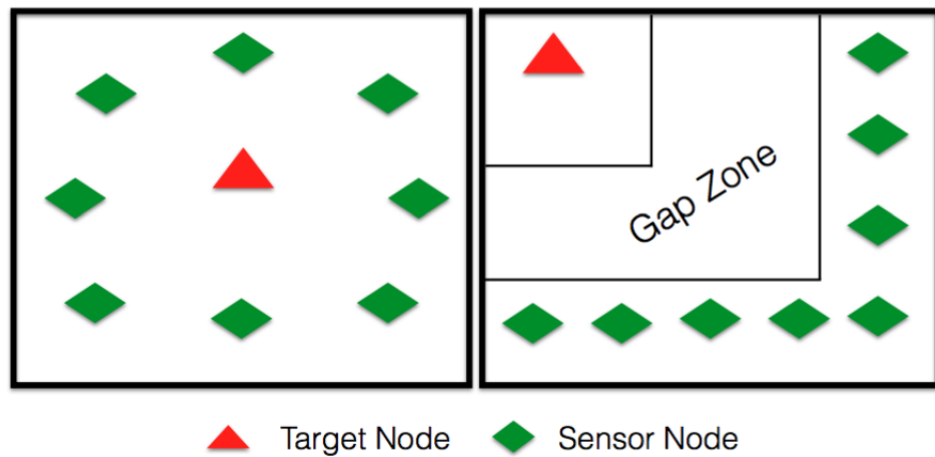


Figure 5.1 2-D top view of System model in Chapter 4 for the two scenarios mixed (left) and separated (right).

Table 5.1 Notations and Definitions

Notation	Meaning
n	Dimensional space
\mathbf{p}	Position vector of the target node $\mathbf{p} = [x \ y \ z]^T$
\mathbf{p}_i	Position vector of sensor nodes $\mathbf{p} = [x_i \ y_i \ z_i]^T$
$\ \cdot\ _2$	Euclidean norm
\mathbf{A}^T	Transpose of matrix \mathbf{A}
$[\mathbf{A}]_j$	j^{th} element of matrix \mathbf{A}
\mathbf{A}^\dagger	Pseudo inverse of matrix \mathbf{A}
$\text{edm}(\mathbf{T})$	Squared distances between target nodes
$\text{edm}(\mathbf{S})$	Squared distances between sensor nodes
$\text{edm}(\mathbf{T}, \mathbf{S})$	Squared distances between target and sensor nodes
$\mathbf{G} = \mathbf{P}^T \mathbf{P}$	Gram Matrix
\mathbf{W}	Mask matrix
\mathbf{J}	Geometric Centering Matrix
$\mathbf{1}$	Column vector of all ones
$\text{diag}(\mathbf{G})$	Column vector of the diagonal entries of \mathbf{G}
$\ \cdot\ _F$	Frobenius Norm
p	Degree of polynomial, where $p = 2n$

sider our system model to be the same as the fixed model discussed in Chapter 4. In particular, we examine the target localisation using a centralised range based approaches relying on the distance measurements based on ToA and TDoA. The ToA range based approach can be used in search and rescue scenario [42], where the sensor nodes are locating one of their nodes. This approach leverages an algorithm based on a class of matrix structure called EDMs [90]. EDMs are matrices of the squared distances between points and have many useful properties that will be discussed in more details in Section 5.3. They are used in different applications such as psychometrics, crystallography, machine learning, wireless sensor networks, acoustics, and more. The different EDM properties can be used for the specific purpose of improving localisation performance when the FC cannot receive certain sensors information due to fading or shadowing, etc.

While this interesting approach to the problem of localisation is successful, it is also shown that at high delay values (urban environment) the proposed alternating rank-based EDM algorithm outperforms the conventional LLS based algorithm for the minimum number of sensors. Furthermore, the localisation error decreases when

the conditioning of EDM is better, i.e., when the sensors are further apart from each other and closer to the target.

On the other hand, when no clock synchronisation is available between the nodes, then a better approach is the TDoA range based. In Section 5.4, we extend the LLS algorithm [26, 91] to TDoA. Using TDoA results in an alteration in the calculation of matrix \mathbf{D} , which will include not only Δd but also $(\Delta d)^2$. The LLS performance is compared with WLS [53], and SRD-LS [52]. Although LLS algorithm is known to be of low complexity, its main disadvantage is that its performance is sensitive to the outliers. Thus, to have a better performance, outliers must be identified and their effect should be minimised. Once the outliers are identified, WLS can be used such that the outliers have smaller weights and hence have minimum impact on the final result. In general, the performance of WLS is dependent on the choice of the weights.

However, it has been shown in [52] that SRD-LS demonstrates the best performance with respect to finding the estimated target node position. SRD-LS uses a different approach than multi-lateration; that is used for LLS and WLS; to estimate the target node location. The approach is based on the minimisation of the LS criterion.

5.2 System Model

We consider the same 3-D MASNET system model proposed in Chapter 4. Two proposed scenarios are shown in Fig. 5.1. One is a mixed scenario where the target and sensor nodes are in the same region and the other is a separated scenario, where the target node and sensor nodes are separated by a gap zone. We assume the location of sensor nodes and the distances between them are known. For the centralised approach, the sensors acquire the time information of the received RF signal, then these time measurements are forwarded to the FC. The next task for the FC depends on which technique being used.

- For ToA, the FC converts the time measurements into corresponding distances.

- For the TDoA, the first sensor is chosen to be the reference sensor. Then, the FC subtracts the receiving times of all other sensors from the reference sensor.

Then, these ToA and TDoA measurements are multiplied by the speed of signal propagation to get the distance and distance differences measurements, respectively. Since we consider 3-D space, we need at least 4 (5) sensor nodes for ToA (TDoA) to localise the target node.

5.3 ToA localisation algorithms

In this section, the range based information that is transmitted to the FC from the sensor nodes are ToA estimates and sensor position information. The FC will then perform an initial analytical task, which will eventually achieve localisation of the RF emissions. This task is translating the ToA measurements and sensor nodes' positions into distances. We compare between the performance of the conventional LLS algorithm and the proposed alternating rank-based EDM algorithm. In the first localisation step, the range measurements between the target node and the sensor nodes

$$\hat{d}_i^2 = \|\mathbf{p} - \mathbf{p}_i\|_2^2 = (x - x_i)^2 + (y - y_i)^2 + (z - z_i)^2, \quad (5.1)$$

where the notations are given in Table 5.1.

5.3.1 LLS algorithm

By reorganising (5.1), and introducing a new dummy variable $R = x^2 + y^2 + z^2$, we obtain

$$-2x_ix - 2y_iy - 2z_iz + R = \hat{d}_i^2 - x_i^2 - y_i^2 - z_i^2, \quad (5.2)$$

which can be also written in a matrix form

$$\mathbf{A}\mathbf{\Lambda} = \mathbf{b}, \quad (5.3)$$

where

$$\mathbf{\Lambda} = [x \ y \ z \ R]^T, \mathbf{A} = \begin{bmatrix} -2x_1 & -2y_1 & -2z_1 & 1 \\ -2x_2 & -2y_2 & -2z_2 & 1 \\ \cdot & \cdot & \cdot & \cdot \\ \cdot & \cdot & \cdot & \cdot \\ -2x_S & -2y_S & -2z_S & 1 \end{bmatrix}, \mathbf{b} = \begin{bmatrix} \hat{d}_1^2 - x_1^2 - y_1^2 - z_1^2 \\ \hat{d}_2^2 - x_2^2 - y_2^2 - z_2^2 \\ \cdot \\ \cdot \\ \hat{d}_S^2 - x_S^2 - y_S^2 - z_S^2 \end{bmatrix} \quad (5.4)$$

Due to the linear model in (5.3), the LLS solution and target estimated position $\hat{\mathbf{p}}$ are, respectively, given by

$$\hat{\Lambda} = \mathbf{A}^\dagger \mathbf{b}, \quad \hat{\mathbf{p}} = [[\mathbf{\Lambda}]_1 \ [\mathbf{\Lambda}]_2 \ [\mathbf{\Lambda}]_3], \quad (5.5)$$

where $\mathbf{A}^\dagger = (\mathbf{A}^T \mathbf{A})^{-1} \mathbf{A}^T$ and the rest of the notations are in Table 5.1. Although LLS is a low complexity algorithm, its main disadvantage is that its performance is sensitive to the outliers. Therefore, we propose the alternating rank-based EDM algorithm which is explained in Section 5.3.2.

5.3.2 Alternating Rank-based EDM algorithm

The use of EDMs leads to two key analytical steps :

- Given a matrix with noisy data, test if its structure is EDM or not.
- Given an incomplete set of distances as shown in Figure 5.2, determine whether a configuration of points exists that generates a matrix that is EDM.

Before explaining the proposed alternating rank-based EDM algorithm, we state the basic definitions and properties for the EDM in Section 5.3.2.1.

5.3.2.1 Definition and properties of EDM

EDMs are matrices of the squared distances between points, (i.e., distances between sensor and target nodes, and distances between sensor nodes) and because they have a certain structure, they have many useful properties and applications such

Algorithm 1 Alternating Rank Based EDM Algorithm [90]

Inputs: \mathbf{D} , \mathbf{W} , n , max.tolerance

Output: \mathbf{E}

```

1: Initialisation and Definitions:
2:  $\mathbf{D}_{11^T-\mathbf{W}} \leftarrow \mu$       Initialise unknown entries
3:  $\mathbf{J} \leftarrow \mathbf{I} - \frac{1}{k}\mathbf{1}\mathbf{1}^T$     Define Geometric centering matrix
4: repeat
5:    $\mathbf{G} \leftarrow \frac{-1}{2}\mathbf{J}\mathbf{D}\mathbf{J}$       Compute Gram Matrix
6:    $\mathbf{U}, [\lambda]_{i=1}^k \leftarrow \text{EVD}(\mathbf{G})$   Eigenvalue Decomposition
7:    $\Sigma \leftarrow \text{diag}(\lambda_1, \dots, \lambda_n, 0, \dots, 0)$ 
8:   Compute  $\mathbf{G} \leftarrow \mathbf{U}\Sigma\mathbf{U}^T$ 
9:   Compute  $\mathbf{E} = \text{diag}(\mathbf{G})\mathbf{1}^T - 2\mathbf{G} + \mathbf{1}\text{diag}(\mathbf{G})$ 
10:  Compute  $e_1 = \|\mathbf{E} - \mathbf{D}\|_F$ 
11:   $\mathbf{E}_{\mathbf{W}} \leftarrow \mathbf{D}_{\mathbf{W}}$       Enforce known entries
12:   $\mathbf{E}_{\mathbf{I}} \leftarrow 0$       Set Diagonal to zero
13:   $(\mathbf{E})_- \leftarrow 0$       Assign zeros to the negative entries
14:  Compute  $e_2 = \|\mathbf{E} - \mathbf{D}\|_F$ 
15:  if  $(e_1 < \text{max. tolerance}) \vee (e_2 < \text{max.tolerance})$  then return  $\mathbf{E}$ 
16:  else
17:     $\mathbf{D} \leftarrow \mathbf{E}$ 
18:
19:  end if
20: until Convergence or MaxIter
21:  $\text{EVD}(\mathbf{E}) = \mathbf{Q}\Sigma\mathbf{Q}^T$   Eigenvalue Decomposition to obtain the target position
22:  $\Sigma \leftarrow \text{diag}(\lambda_1, \dots, \lambda_{n+2}, 0, \dots, 0)$ 
23:  $\mathbf{X} = \Sigma^{1/2}\mathbf{Q}^T$ 

```

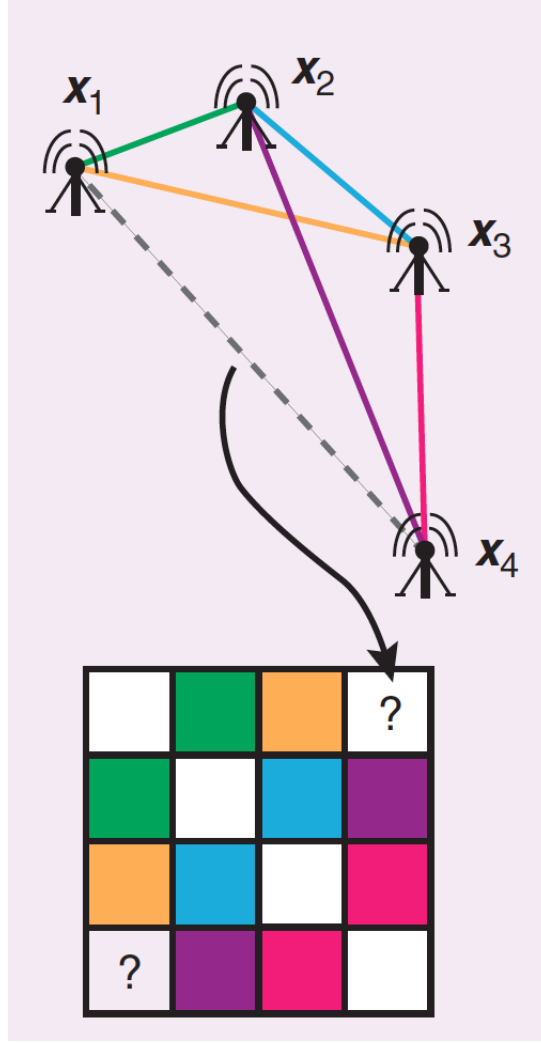


Figure 5.2 Estimated pairwise distances is illustrated with one distance missing [90].

as crystallography, wireless sensor networks, acoustics, etc [90]. The main EDM-related task is to reconstruct the original node location. This task is an inverse problem which is more complex than the forward problem of calculating the EDM given the nodes locations. Therefore, we would like to have an analytic expression for the EDM in terms of nodes locations.

Consider a collection of S sensor nodes in a n -dimensional Euclidean space, ascribed to the columns of matrix $\mathbf{P} \in \mathbb{R}^{n \times S}$, $\mathbf{P} = [\mathbf{p}_1, \mathbf{p}_2, \dots, \mathbf{p}_S]$, $\mathbf{p}_i \in \mathbb{R}^n$. Then the squared distance between \mathbf{p}_i and \mathbf{p}_j can be calculated using (5.1) and when the norm is expanded then we obtain

$$d_{ij} = (\mathbf{p}_i - \mathbf{p}_j)^T (\mathbf{p}_i - \mathbf{p}_j) = \mathbf{p}_i^T \mathbf{p}_i - 2\mathbf{p}_i^T \mathbf{p}_j + \mathbf{p}_j^T \mathbf{p}_j. \quad (5.6)$$

Equation (5.6) can be also written in the matrix equation $\mathbf{D} = [d_{ij}]$

$$\text{edm}(\mathbf{P}) \stackrel{(\text{def.})}{=} \mathbf{1}\text{diag}(\mathbf{P}^T\mathbf{P}) - 2\mathbf{P}^T\mathbf{P} + \text{diag}(\mathbf{P}^T\mathbf{P})\mathbf{1}^T, \quad (5.7)$$

where the notations are defined in Table 5.1. From (5.7), we discover an important property for the EDM, which is stated in Proposition 13.

Proposition 13 *Rank of EDMs : The rank of an EDM corresponding to nodes in \mathbb{R}^n is at most $n + 2$ [90].*

Proof 13 *Since the rank of \mathbf{P} is at most n (i.e. it has n rows) then the rank of $\mathbf{P}^T\mathbf{P}$ is also at most n . The rank of the remaining two summands in (5.7) is one. Using rank inequalities, the rank of the sum of matrices cannot exceed the sum of the ranks of the summands.*

This concludes the proof.

Proposition 13 is powerful as it states that the rank of EDM is dependent on the n dimensional space which can be $\{2, 3\}$ and independent of the number of nodes which can be in the order of hundreds or thousands.

The alternating rank-based EDM algorithm exploits the two pieces of information available, which are a subset of potentially noisy distances and the desired embedding dimension, to calculate the relative position of the target node. This is done by alternating between these two properties in the hope that the algorithm converges to an EDM from the produced sequence of matrices. The approach is shown in detail in Algorithm 1 and appropriate definitions may be seen in Table 5.1.

We consider two sets of nodes, where the first set is a single target node ($m = 1$) and the second set comprises the S sensor nodes. Following the approach in [90], the input distance matrix to the algorithm is defined in the following structure

$$\mathbf{D} = \begin{bmatrix} \text{edm}(\mathbf{T}) & \text{edm}(\mathbf{T}, \mathbf{S}) \\ \text{edm}(\mathbf{S}, \mathbf{T}) & \text{edm}(\mathbf{S}) \end{bmatrix}, \quad (5.8)$$

since we consider a single target, so $\text{edm}(\mathbf{T}) = 0$. The squared distances between the sensor nodes $\text{edm}(\mathbf{S})$ are known since we assume that the sensor nodes locations are known. This is an additional advantage of rank-based EDM approach, where the distances between sensors and their locations act as reference and additional information. According to the symmetric property $\text{edm}(\mathbf{T}, \mathbf{S}) = \text{edm}(\mathbf{S}, \mathbf{T})$, which are the squared distances between the target and sensor nodes measured using the time information of received signal at each sensor, these measured distances are subject to noise (delay) due to multi-path components. The input mask matrix \mathbf{W} is defined as follows

$$\mathbf{W} = \begin{bmatrix} \mathbf{W}_{\mathbf{T}} & \mathbf{W}_{\mathbf{T},\mathbf{S}} \\ \mathbf{W}_{\mathbf{S},\mathbf{T}} & \mathbf{W}_{\mathbf{S}} \end{bmatrix} \quad (5.9)$$

where the elements in $\mathbf{W}_{\mathbf{T},\mathbf{S}}$ and $\mathbf{W}_{\mathbf{S},\mathbf{T}}$ are defined as follows:

$$w_{i,j} = \begin{cases} 1, & \text{if } (m, j) \in K \\ 0, & \text{otherwise,} \end{cases} \quad (5.10)$$

where m is the index of target node, j is the index of sensor nodes (i.e. $j = 1, 2, \dots, s$), and K is the set of observed distances between target and sensor nodes. Furthermore, the indexing $\mathbf{D}_{\mathbf{W}}$ is defined as the restriction of \mathbf{D} to the entries where \mathbf{W} is non-zero. Thus the goal of the mask matrix, \mathbf{W} , is simply to differentiate between the observed and unobserved entries in \mathbf{D} .

To ensure convergence of the algorithm, rank thresholding; i.e. truncating the eigenvalues $[\lambda] = \lambda_1, \dots, \lambda_d, 0, \dots, 0$, is performed on the $\mathbf{G} = \mathbf{P}^T \mathbf{P}$, and then \mathbf{E} is computed as in (5.7) for centered locations. A linear map from \mathbf{G} to an \mathbf{E} is given in step 9 in Algorithm 1 [125]. Then, to follow the structure of EDM given in (5.8), we assign zeros to diagonal and negative elements of matrix \mathbf{E} .

After convergence, the next stage is to apply the multidimensional scaling (MDS) algorithm [53], [26], in order to determine the best point set representation of a given set of distances. The MDS has analytical solutions that can be obtained via eigenvalue decomposition of a transform of the EDM. Second, the MDS technique is relatively resilient to distance errors due to the over-determined nature of the

problem. Moreover, the results presented in [41], showed that MDS have similar performance to maximum likelihood estimator (MLE) on condition that all distance measurements are available. The MDS is shown in the last three steps of Algorithm 1, where we know that the resulting \mathbf{E} is an EDM with rank $n + 2$, so we perform eigenvalue decomposition and use only the squared root of the first $n + 2$ eigenvalues multiplied by the eigenvectors matrix \mathbf{Q} to obtain the target position. Note that the position resulting from MDS is a relative position, which may be rotated, or translated.

Thus, as a final step for the localisation problem, a procrustes analysis [126] is applied, which is the problem of finding the optimum alteration that happened to the nodes. Since the initial locations of sensor nodes are known, these locations are compared to the new locations that we recomputed. After computing the rotation matrix and the translated vector, these values are compensated on the relative position of target node to provide a good estimate for the target node location. The details and proof of this analysis can be found in [90] [Section II (C)].

Finally, algorithm 1 can be summarised as

- Tabulate the known distances between sensors and the measured distances between that target and the sensors as the structure given in (5.8)
- Using the rank property and the symmetric structure of \mathbf{D} , calculate a new matrix of distances \mathbf{E} . This matrix should be checked to have the diagonal elements zeros and no negative elements. Then compute the error between the input and the calculated matrices and repeat until convergence.
- The resultant matrix is considered an EDM, so we use MDS to obtain the relative target position. This relative position may be rotated or translated, therefore, we use the procrustes analysis and the known positions of the sensor nodes to find the estimated target position $\hat{\mathbf{p}}$.

5.4 TDoA localisation algorithms

In alternating rank-based EDM and LLS algorithms used in previous results, the ToA of the received signals at the sensor nodes were used to localise the target. Our motivation was based on a similar approach in [127], where joint synchronisation and localisation for the sensor nodes using EDM approach was performed. However, to localise the target node, where target location and the transmit time are unknowns and there is no centralised clock between the target and the sensor nodes. A better and more practical approach is to use TDoA measurements which only requires synchronisation between the sensor nodes.

5.4.1 LLS and WLS

For the TDoA, there is a slight alteration in LLS and WLS algorithms in the calculation for matrix \mathbf{A}_{TDoA} and vector \mathbf{b}_{TDoA} that were calculated in Section 5.12 which is given as

$$\begin{aligned} \mathbf{A}_{\text{TDoA}} &= [x \ y \ z]^T, \\ \mathbf{A}_{\text{TDoA}} &= 2 \begin{bmatrix} x_1 - x_r & y_1 - y_r & z_1 - z_r \\ x_2 - x_r & y_2 - y_r & z_2 - z_r \\ . & . & . \\ . & . & . \\ x_S - x_r & y_S - y_r & z_S - z_r \end{bmatrix}, \\ \mathbf{b}_{\text{TDoA}} &= \begin{bmatrix} \hat{d}_r^2 - \hat{d}_1^2 - k_r + k_1 \\ \hat{d}_r^2 - \hat{d}_2^2 - k_r + k_2 \\ . \\ . \\ \hat{d}_r^2 - \hat{d}_S^2 - k_r + k_S \end{bmatrix}, \end{aligned} \tag{5.11}$$

where we assume r^{th} sensor to be the reference node and define $k_i = x_i^2 + y_i^2 + z_i^2$, $i = 1, 2, \dots, S$. The estimated target position for LLS technique is given as

$$\hat{\mathbf{p}}_{\text{TDoA}}^{\text{LLS}} = \hat{\mathbf{\Lambda}}_{\text{TDoA}} = \mathbf{A}_{\text{TDoA}}^\dagger \mathbf{b}_{\text{TDoA}}, \quad (5.12)$$

where the notations are in Table 5.1 and Section 5.12.

While the estimated target position for WLS technique is given as

$$\hat{\mathbf{p}}_{\text{TDoA}} = \hat{\mathbf{\Lambda}}_{\text{TDoA}} = \left(\mathbf{A}^T \mathbf{W}^{-1} \mathbf{A} \right)^{-1} \mathbf{A}^T \mathbf{W}^{-1} \mathbf{b}, \quad (5.13)$$

where \mathbf{W} is the weighting diagonal matrix and the rest of the notations are in Table 5.1.

As stated in Section 5.12, LLS is a low complexity algorithm, but its main disadvantage is that its performance is sensitive to the outliers. In order to have a better performance, outliers must be identified and their effect should be minimised. Once the outliers are identified, we can use the WLS such that the outliers have smaller weights and hence have minimum impact on the final result. Our approach to identify outliers is by examining the average signal-to-noise ratio (SNR) over multiple time slots. In such a case, the sensors with lower SNRs are considered to be the outliers. The weights are calculated by dividing the SNRs of all sensors by the maximum SNR. This ensures that the outliers (having low SNRs) have low weights. In general, the performance of WLS is dependent on the choice of the weights. The procedure suggested is just an intuitive way to obtain the weights. More intricate methods for determining the weights can be used for improving the results.

5.4.2 SRD-LS algorithm

However, for this problem, it has been shown in [52] that SRD-LS demonstrates the best performance with respect to finding the estimated target node position. SRD-LS uses a different approach than multi-lateration to estimate the target node location. The approach is based on the minimisation of the LS criterion and is given

by

$$\underset{\mathbf{p} \in \mathbb{R}^n}{\text{minimize}} \sum_{i=1}^S (-2\mathbf{p}_i^T \mathbf{p} - 2d_i \|\mathbf{p}\| - g_i)^2, \quad (5.14)$$

where $g_i = d_i^2 - \|p_i\|^2$. Since this problem is non-convex, finding its exact solution is in principle a difficult task. So this problem (5.14) is rewritten as a quadratic problem with two quadratic constraints (5.15) (where a linear constraint is a special case of a general quadratic constraint) [52].

$$\underset{\mathbf{y} \in \mathbb{R}^{n+1}}{\text{minimize}} \quad \|\mathbf{B}\mathbf{y} - \mathbf{g}\|^2, \quad (5.15)$$

$$\text{subject to} \quad \mathbf{y}^T \mathbf{C} \mathbf{y} = 0, y_{n+1} \geq 0, \quad (5.16)$$

where

$$[\mathbf{y}]_{(n+1) \times 1} = \begin{pmatrix} \mathbf{p}^T & \|\mathbf{p}\|^T \end{pmatrix},$$

$$[\mathbf{C}]_{(n+1) \times (n+1)} = \begin{pmatrix} \mathbf{I}_n & \mathbf{0}_{n \times 1} \\ \mathbf{0}_{1 \times n} & -1 \end{pmatrix},$$

and

$$[\mathbf{B}]_{S \times (n+1)} = \begin{pmatrix} -2\mathbf{p}_1^T & -2d_1 \\ \cdot & \cdot \\ \cdot & \cdot \\ -2\mathbf{p}_S^T & -2d_s \end{pmatrix} \quad (5.17)$$

It was shown that based on the special structure of (5.15), an efficient algorithm was derived to find a global solution to this problem [52]. More details about the SRD-LS algorithm is in [52].

The SRD-LS algorithm solution procedures is shown in Algorithm 2. As stated in Algorithm 2, if \mathbf{z} satisfies $z_{n+1} \geq 0$, then \mathbf{z} is a global optimum solution. However, there is no guarantee that z_{n+1} will indeed be nonnegative, especially in high noise levels. In this case, we search for all roots for which the $(n+1)^{\text{th}}$ element of $\tilde{\mathbf{y}}(\lambda_i)$ is nonnegative. The SRD-LS solution is the vector with the smallest objective function. For large number of sensors and large number of time slots, SRD-LS usually results in the global optimum. This conclusion will be confirmed using the results in Section

5.5.2.

5.5 Results

In this section, we present the results of the algorithms proposed in the previous sections. Our main objective is to compare between the localisation error using the minimum number of sensors (4 or 5 for ToA or TDoA) and the total number of "active" sensors that detected the signal (Chapter 4).

5.5.1 ToA Algorithms

In a three-dimensional space, the minimum number of sensors required to localise the target is four. The total number of "active" sensors is ten (fixed model in Chapter 4). A comparison between the proposed alternating rank-based EDM algorithm and the conventional method based on LLS [128] is indicated in Fig. 5.3 and Fig. 5.4.

We present a comparison of localisation error for using all ten sensors with that obtained using four randomly picked sensors out of the available ten. We assume that all the sensors detected the transmitted signal from the target, i.e., there is no missing information. The height of the target node is set to 5 m and the heights of the sensor nodes are varying between 0 and 4 m. The sensors and target nodes are randomly distributed in an area of $200 \times 200 \text{ m}^2$ for the mixed scenario.

Algorithm 2 SRD-LS Algorithm [52]

Inputs: \mathbf{B} , \mathbf{g} , \mathbf{C}

Output: \mathbf{y}

- 1: Find λ^* to $\tilde{\mathbf{y}}(\lambda)^T \mathbf{C} \tilde{\mathbf{y}}(\lambda) = 0$, $\lambda \in I_1$, where $\tilde{\mathbf{y}}(\lambda) = (\mathbf{B}^T \mathbf{B} + \lambda \mathbf{C})^{-1} \mathbf{B}^T \mathbf{g}$,
 - 2: set $\mathbf{z} = \tilde{\mathbf{y}}(\lambda^*)$
 - 3: **if** ($z_{n+1} > 0$) **then return** $(\mathbf{y})^*$ which is the first n elements of (\mathbf{z}) (i.e. global optimum solution)
 - 4: **else**
 - 5: Find all the roots $\lambda_1, \dots, \lambda_p$ to $\tilde{\mathbf{y}}(\lambda)^T \mathbf{C} \tilde{\mathbf{y}}(\lambda) = 0$, $\lambda \in I_0 \cup I_2$ for which the $(n+1)$ th element of $\tilde{\mathbf{y}}(\lambda_i)$ is non-negative
 - 6: Let \mathbf{z} be the vector with the smallest objective function among the vectors $\mathbf{0}$, $\tilde{\mathbf{y}}(\lambda_1), \dots, \tilde{\mathbf{y}}(\lambda_p)$ **return** \mathbf{y} which is the first n elements of \mathbf{z}
 - 7: **end if**
-

For the separated scenario, the target node is randomly located in an area of $20 \times 20 \text{ m}^2$, whereas the sensors are divided into two equal perpendicular rectangular areas of $200 \times 20 \text{ m}^2$ and $20 \times 180 \text{ m}^2$ with a gap zone in between as shown in Fig. 5.1. The position of target and the ten "active" sensors nodes are randomly chosen. The delay parameter, μ is the mean of the exponential random variable in [129, 130].

The amount of added delay can be treated as a positive bias to the theoretical time of flight that a signal would take to travel between the transmitter and the receiver if they were in free space. Hence, it represents noise included in the time information measurements. For example, if $\mu = -8.5$, it is equivalent to $10^{-8.5} \approx 3 \text{ ns}$ and if $\mu = -7$, it is equivalent to $10^{-7} \approx 100 \text{ ns}$. Consequently, low values of μ translates to low mean values of additional random time delays and therefore less noise and vice versa for high values of μ .

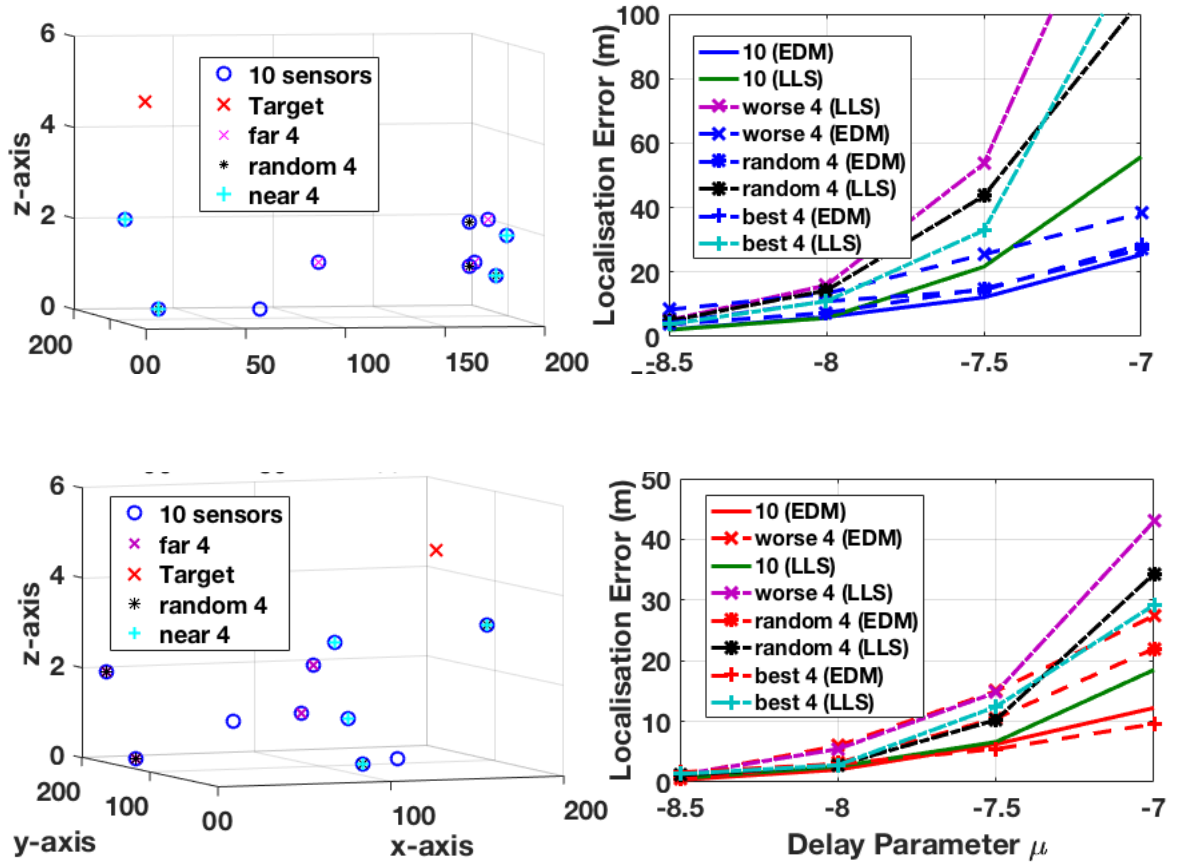


Figure 5.3 Localisation error vs μ for the two scenarios: separated (top) and mixed (bottom), with different number of sensors ($N_s = 4, 10$). The solid lines are for the ten sensors and the dotted lines are for two different picks of four sensors.

5.5.1.1 Localisation error plots versus varying the delay parameter μ

The first set in Fig. 5.3 compares the localisation error over four randomly picked sensors and when all "active" ten sensors are used, in terms of average location error, i.e., error between the estimated and actual target node position. First, we observe that the localisation errors for the separated scenarios are larger than mixed scenarios. This is because the sensors in the separated scenarios experience similar receiving time information, hence calculate similar distances. This leads to an EDM which is not well-separated in terms of distances and hence not well-conditioned [131]. However, in the mixed scenarios, the sensors experience varying receiving times and corresponding distances, improving the conditioning of the EDM, leading to better performance [131].

Moreover, for smaller values of μ (low noise), both the proposed alternating rank-based EDM algorithm and the conventional LLS algorithm with the minimum number of sensors (four), achieve localisation errors closer to the ten sensor results. However, the performance gap between using all ten sensors and only four sensors, is prominent for higher values for μ . This is because more information (obtained using all ten sensors) is beneficial at higher noise levels. Also, there are some rare cases, such as the case using the best four sensors in high noise, where four sensors perform better than ten using the proposed algorithm. This occurs when these sensors are close to the target and experience smaller overall delays. As the amount of noise increases, the proposed alternating rank-based EDM algorithm outperforms the corresponding LLS algorithm. The high noise levels result in large deviation of the measured distances from the expected value, thereby causing outliers in the system. These outliers in-turn degrade the performance of the conventional LLS algorithm, resulting in large errors in the estimated target node position.

5.5.1.2 CDF plots for random choice of sensors

The random choice of sensors' behaviour is analysed in detail in Fig. 5.4, where the CDF of the localisation error is plotted for the proposed alternating rank-based EDM algorithm evaluated using all possible combinations of four out of ten sensors.

The figures also show the LLS performance using all ten sensors with and without outliers. For no outliers case, we assume that all sensors experience the similar delay.

The delay distribution used for the no outlier case is uniform with small standard deviation. These results confirm the observations from Fig. 5.3, that for approximately 90% of the combinations, the proposed algorithm outperforms the LLS algorithm with outliers at high delay $\mu = -7$. However, the LLS algorithm without outliers performs better than the proposed algorithm. This indicates that the proposed alternating rank-based EDM algorithm is more robust towards handling outliers than the conventional LLS algorithm.

5.5.2 TDoA Algorithms

In this section, we provide the results for the average localisation error for LLS, WLS and SRD-LS. For all the algorithms, we calculate the average TDoA and the average SNR over multiple time slots. The average TDoA is obtained by only using the TDoA measurements [132] of the time slots in which the sensors detected the transmission from the target. The detection in these results is based on the received power at each sensor. If the received power at the sensor is bigger than the threshold (receiver sensitivity) [133], then the sensor detects the received signal (Chapter 4).

5.5.2.1 Localisation error plots versus varying number of time slots

In Figure 5.5, the average localisation error plots vs. the number of time slots are presented for mixed and separated scenarios. The localisation error is higher in the separated scenario due to two reasons. First, there is an increased gap between the target and sensor nodes locations. Second, the receiving times for all the sensors are close to each other. As expected, we observe from Figure 5.5 that LLS gives the worst performance. The use of WLS slightly improves the performance and the SRD-LS demonstrates the best performance.

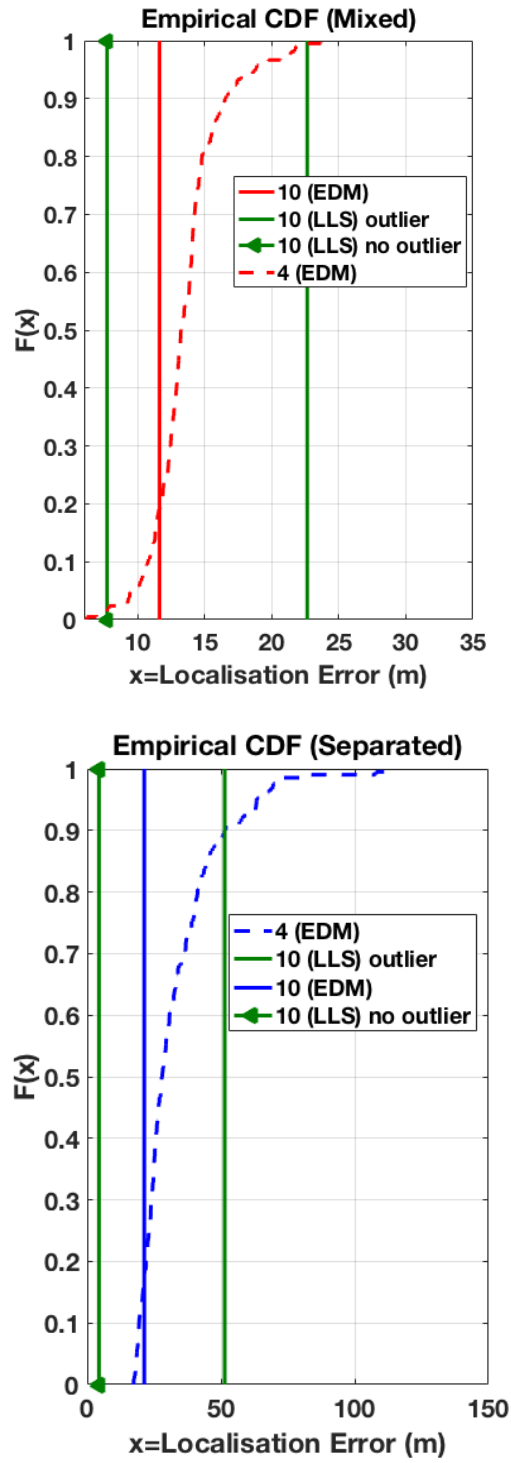


Figure 5.4 CDF plot for the random choice of four sensors from the ten sensors for the mixed (top) and separated (bottom) scenarios with high delays $\mu = -7$.

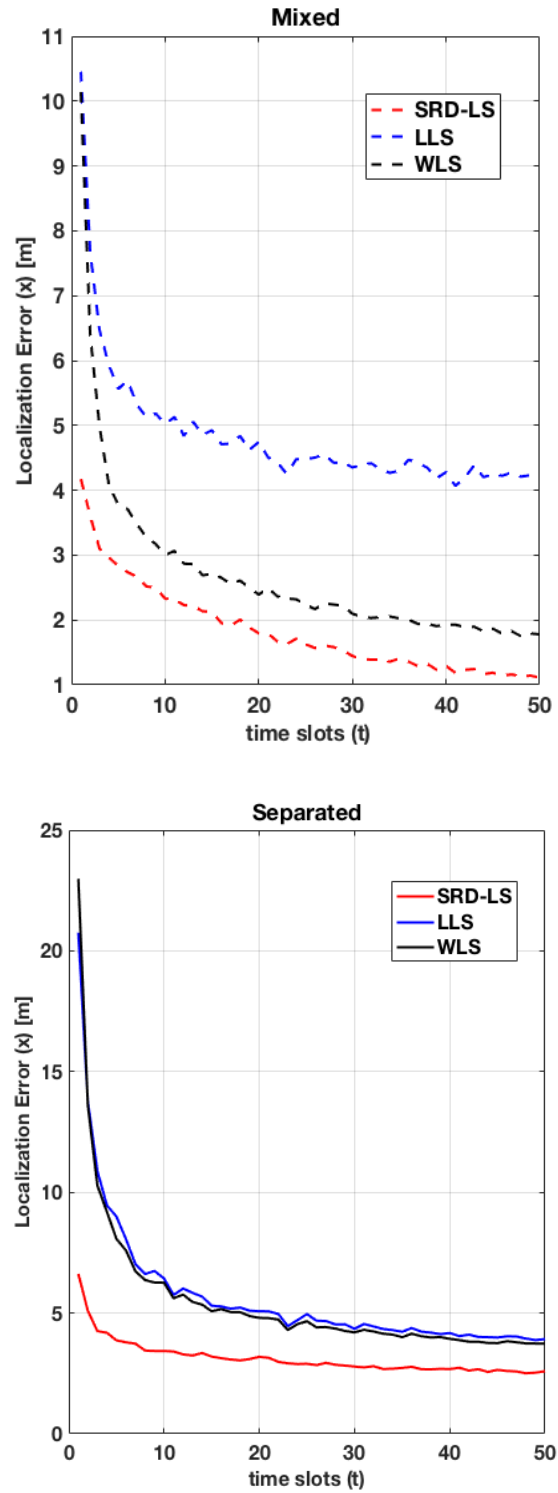


Figure 5.5 Localisation error vs. varying numbers of time slots for three localisation algorithms for the mixed (top) and separated (bottom) scenarios.

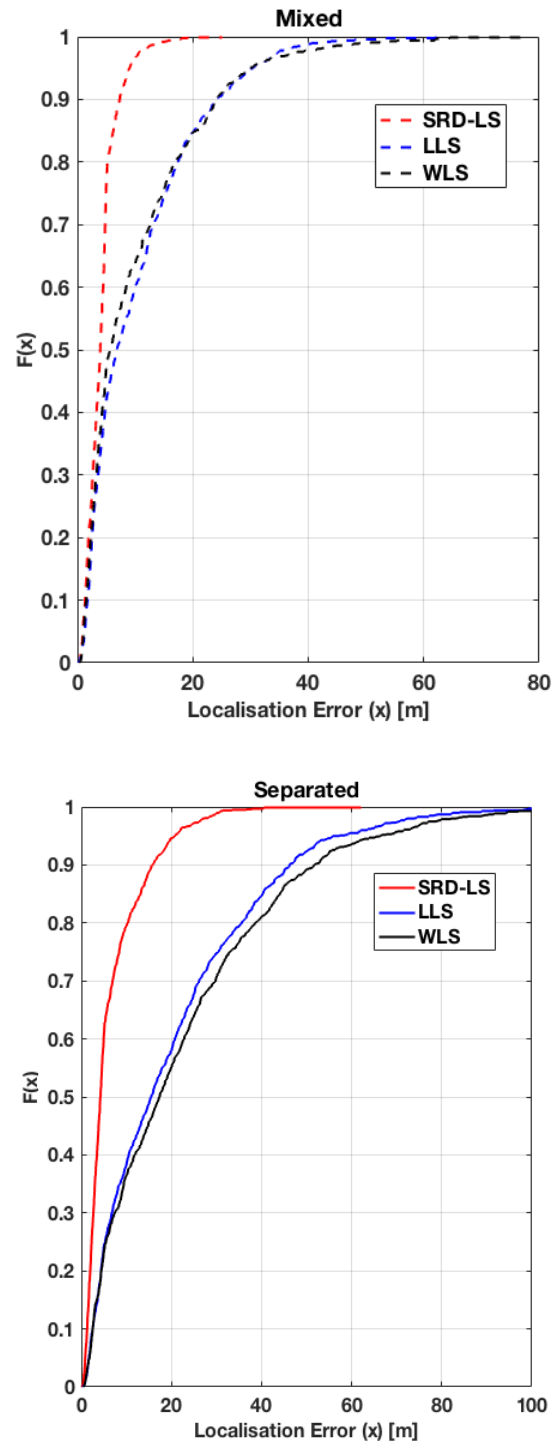


Figure 5.6 CDF plots for the localisation error for $t = 1$ for the mixed (top) and separated (bottom) scenarios.

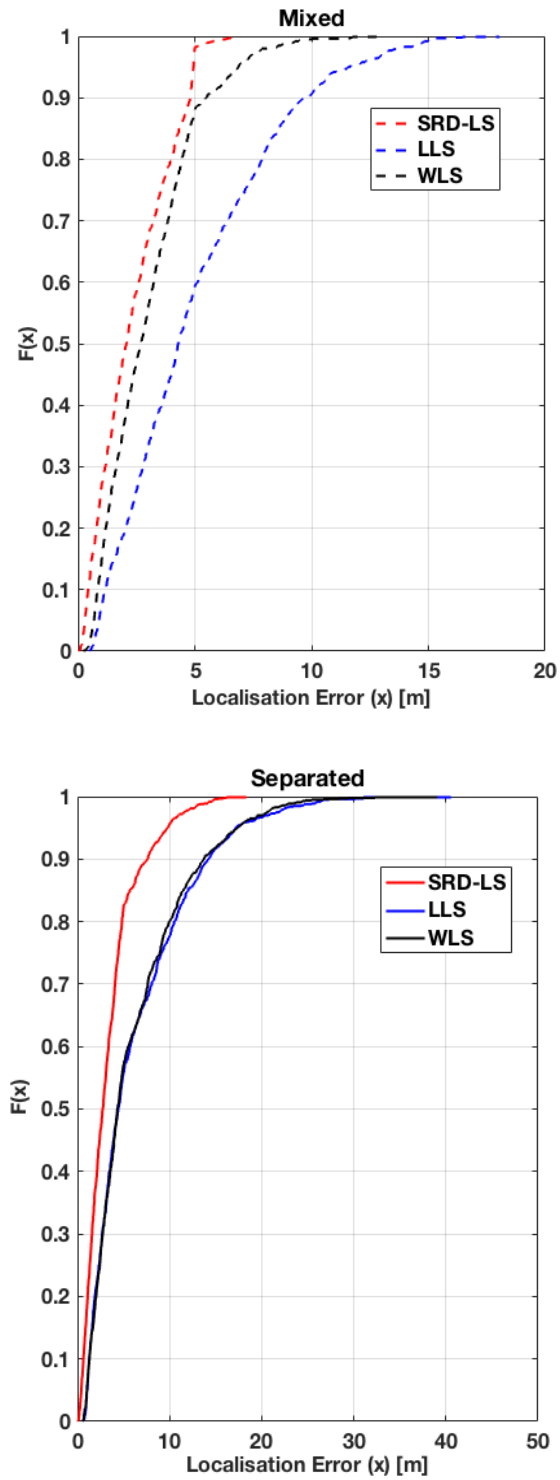


Figure 5.7 CDF plots for the localisation error for $t = 10$ for the mixed (top) and separated (bottom) scenarios.

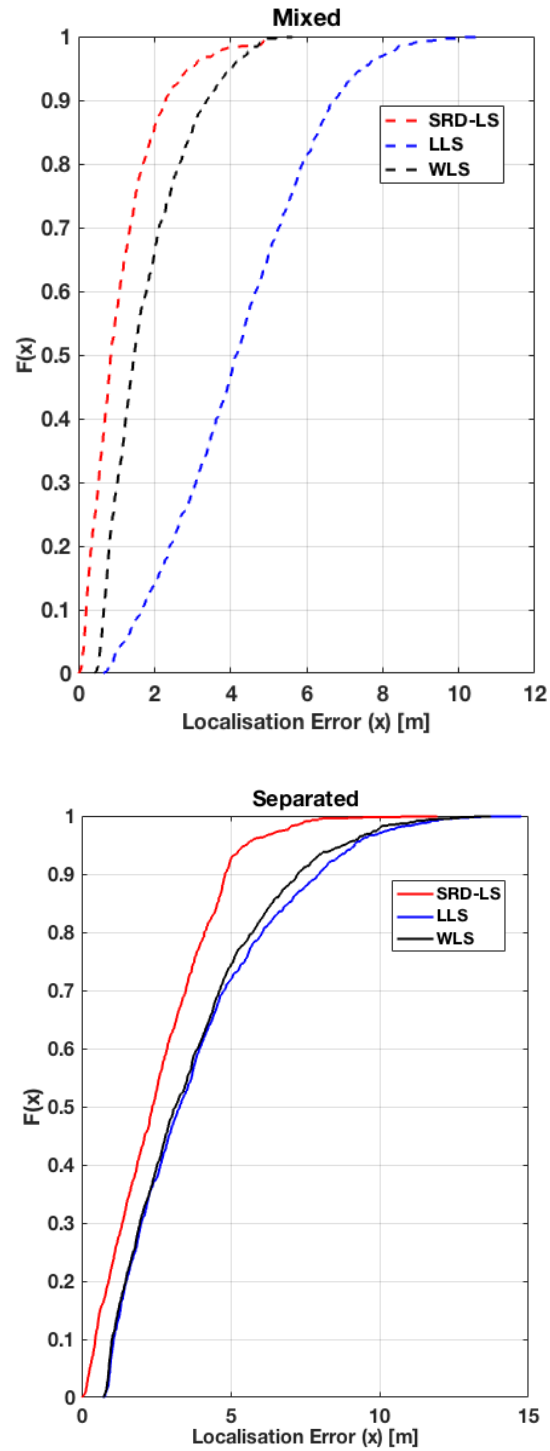


Figure 5.8 CDF plots for the localisation error for $t = 50$ for the mixed (top) and separated (bottom) scenarios.

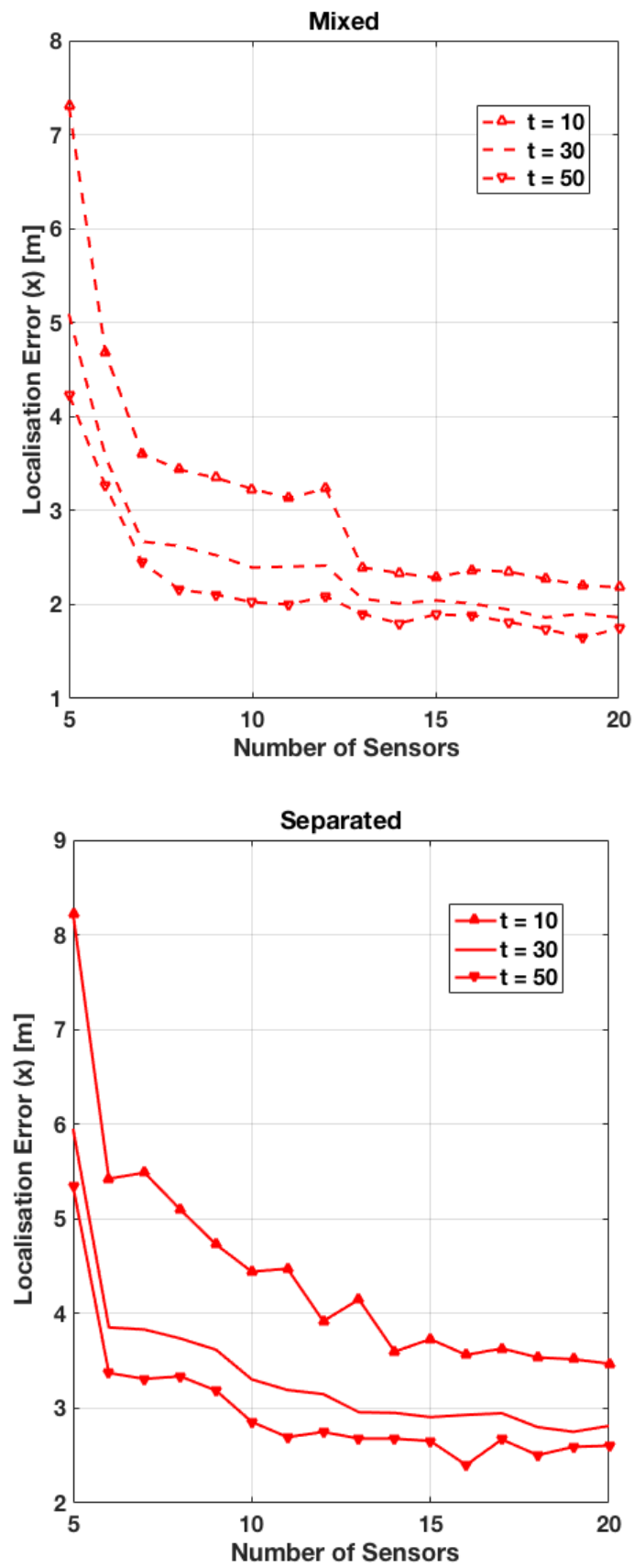


Figure 5.9 Localisation error vs different number of sensors for $t = \{10, 30, 50\}$ for the mixed (top) and separated (bottom) scenarios.

5.5.2.2 CDF plots for the localisation error

The CDF plots for the localisation error are shown in Figures 5.6, 5.7, and 5.8 at three different time slots $t = \{1, 10, 50\}$. The CDF plots further illustrate how all three algorithms perform with respect to a predefined acceptable localisation error of 10 m. In Figure 5.6, for $t = 1$, the SRD-LS algorithm achieves an error less than 10 m ($x < 10$) around 80% and 75% for mixed and separated scenarios, respectively. For the WLS and LLS the percentages were around 60% and 40% for mixed and separated scenarios, respectively. As the number of time slots increases, these percentages increase too. This suggests that using multiple time slots leads to better localisation. An interesting observation is that for mixed scenarios with $t = 10$ onwards (Figures 5.7 and 5.8, the performance of WLS is comparable to that of the SRD-LS. This is because of the sensors are more scattered in a mixed scenario than the separated scenario, making it amenable for a weight-based approach.

5.5.2.3 Localisation error plots versus varying number of sensors

Finally, we evaluate the performance of the best algorithm (SRD-LS) with respect to the "active" number of sensors (Chapter 4), given a fixed number of time slots ($t = \{10, 30, 50\}$). The results are shown in Figure 5.9. As expected, the localisation error decreases as the number of sensors increases. This is because the amount of information increases with the increase in the number of sensors.

5.5.2.4 CDF plots for urban and rural environments

We evaluate the best performance algorithm SRD-LS, where the average SNRs and the probability of detection for all sensors is computed using wireless world initiative new radio (WINNER) channel [129, 130]. According to the probability of detection for each sensor, we define a masking matrix \mathbf{W} of 1s and 0s, the entry 1 denotes sensor detected the signal and 0 otherwise. Using only the active sensors' (detected the signal) locations (Chapter 4) and their corresponding time measurements, we follow the procedures in Section 5.4.2 to localise the target.

As expected, the results in Figures 5.10 and 5.11, show that exploiting more

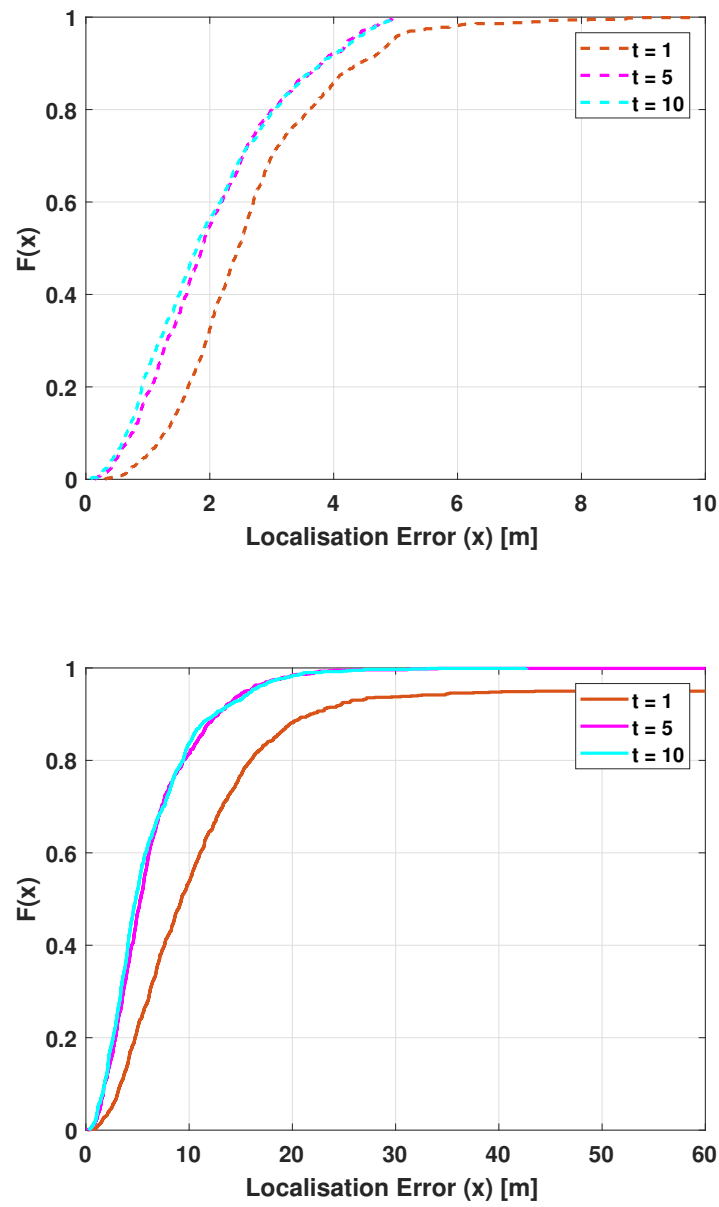


Figure 5.10 CDF plots for the localisation error for $t = \{1, 5, 10\}$ using SRD-LS for mixed (top) and separated (bottom) rural environments.

time slots improve the localisation performance especially in urban environment (high delay). The worst localisation results are shown in the urban environments (Fig. 5.11). This is because SRD-LS does not perform well in high noise levels as the global optimum solution is not obtained. However, for the rural environment (Fig. 5.10), using 5 time slots and onwards result in very good localisation results. Therefore, we conclude that having a large number of sensors and large number of time slots is needed to have a better localisation performance in urban environments.

5.5.2.5 Results using EM Terrano Software

The results for the estimated target location using EM Terrano measurements is presented in Figures 5.12 and 5.13 for mixed and separated scenarios, respectively. These results are obtained by exploiting sensors' locations and time measurements and using Section 5.4.2 to obtain the estimated target location. The estimated target location using all "active" sensors for SRD-LS and LLS is demonstrated. In Fig. 5.12, we observe that the localisation error is mainly in the height. This is because the sensors are not scattered which results in having receiving times of some sensors that are very close to each other. Because there is no outliers, the LLS is performing well, as expected. Then, using the minimum number of best sensors for each scenario, the best estimated target location is computed. The receiving time measurements for these results were averaged over LOS and multi-path components. Note that best sensors are chosen to be more scattered sensors. When we looked at the delay experienced by these sensors, we observed that these sensors also experienced smaller delay values. Therefore, the estimates using only the five best sensors are better than using all sensors. In addition to that, the results also show that if we exploit the receiving time measurements for LOS components only, then a very good estimation of the estimated target location can be estimated. In Fig. 5.13, the separated scenario results are good due to the placement of the sensors and the gap is not so big.

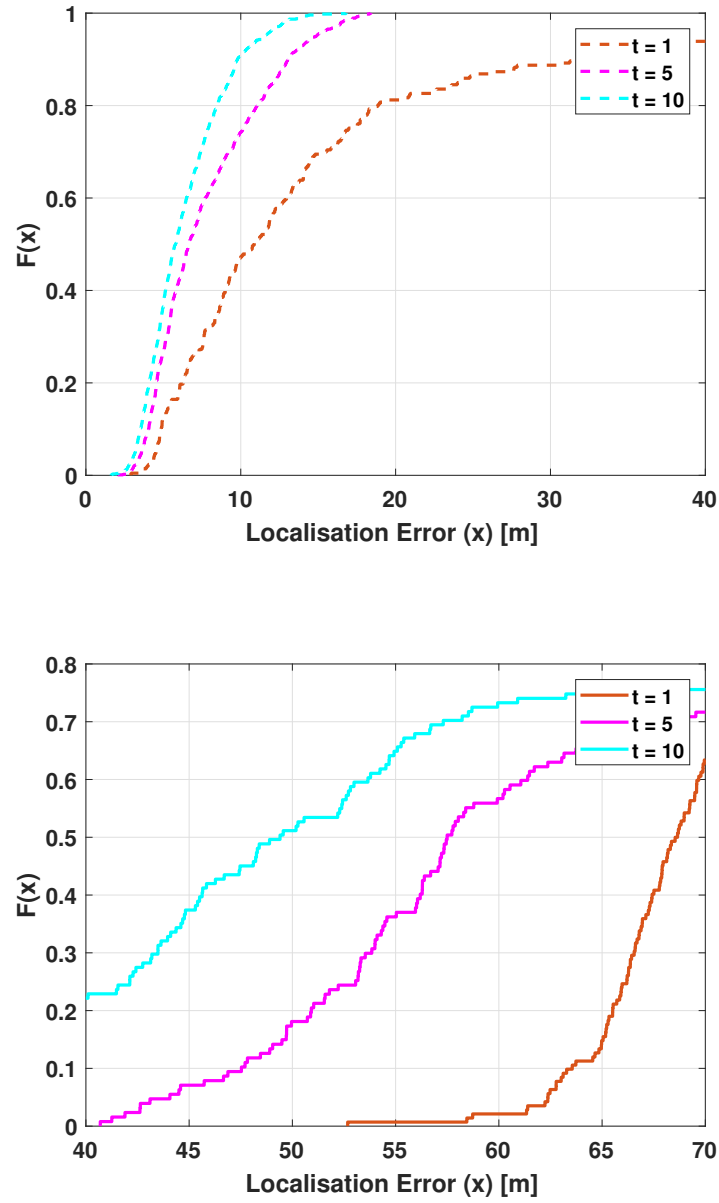


Figure 5.11 CDF plots for the localisation error for $t = \{1, 5, 10\}$ using SRD-LS for mixed (top) and separated (bottom) urban environments

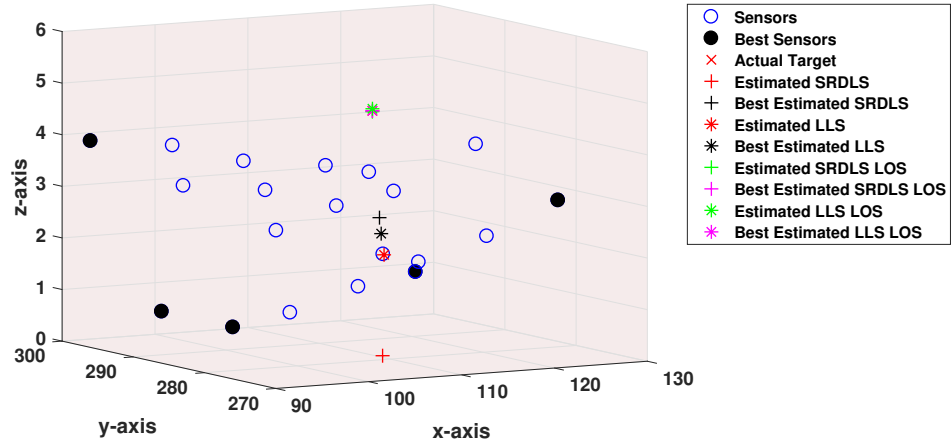


Figure 5.12 Sensor nodes, actual and estimated target locations using EM Terrano measurements for a mixed scenario ($P_T = -23$ dB).

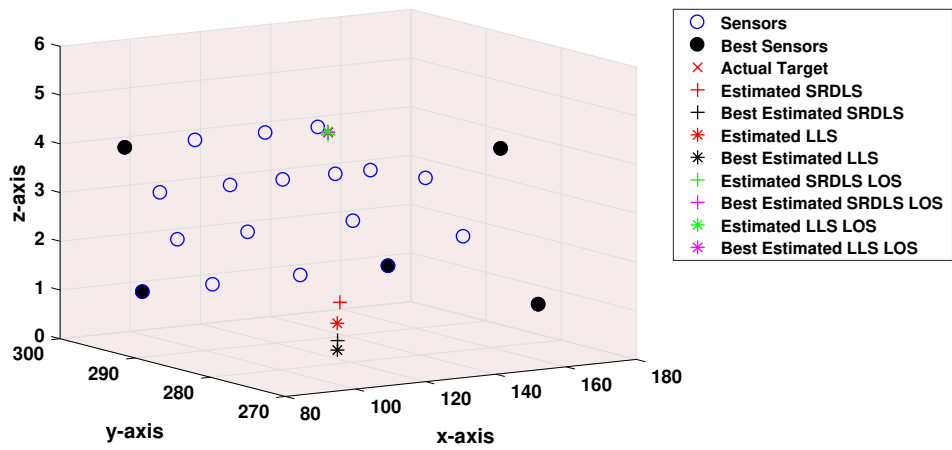


Figure 5.13 Sensor nodes, actual and estimated target locations using EM Terrano measurements for a separated scenario ($P_T = -23$ dB).

5.6 Summary

In this chapter, a comparison between the performance of ToA and TDoA range based localisation algorithms was presented. We considered a mixed and separated scenarios for the locations of the sensors as shown in Figure 5.1.

For ToA algorithms, two centralised localisation algorithms were studied. The two algorithms are LLS and alternating rank-based EDM. It was shown that at high delay values the proposed alternating rank-based EDM algorithm outperformed the conventional LLS algorithm for the minimum number of sensors. The results indicate that the localisation error depends on the amount of delay and the operating scenario for the sensors (separated or mixed). The sensor nodes in the separated scenario experience similar receiving time information which results in larger localisation error than in the mixed scenario where the receiving times are much different. Also, the error decreases when the conditioning of EDM is better, i.e., when the sensors are further apart from each other and closer to the target. Furthermore, unlike the LLS algorithm, the proposed algorithm is less sensitive to outliers resulting from larger errors in the measured distances, thereby making it suitable for the required application.

For TDoA algorithms, three centralised localisation algorithms were examined. The three algorithms are LLS, WLS and SRD-LS. The LLS and WLS are given as a multi-lateration problem, while the SRD-LS is based on the minimisation of the LS criterion. The LLS is low complexity but its performance is sensitive to outliers. Once we identify the outliers, the WLS was used such that the outliers have smaller weights and hence have minimum impact on the final result. However, it has been shown in literature that SRD-LS demonstrates the best performance with respect to finding the estimated target node position. In low noise levels, for large number of sensors and time slots, SRD-LS usually results in a global optimum solution. However, in large noise levels SRD-LS might not result in global optimum. The number of time slots refer to the number of times at which the target transmits and also the number of time measurements.

The results show that LLS gave the worst performance, then WLS slightly improved the performance and SRD-LS gave the best performance. We observed that as the number of time slots increased, the maximum localisation error decreased, as expected. Moreover, an interesting observation was that for mixed scenarios at high number of time slots the performance of WLS was comparable to the performance of SRD-LS. The reason is at mixed scenarios the sensors were more scattered making it amenable for a weight-based approach. Finally, as identified, the localisation error decreased as the number of sensors increased.

Chapter 6

Conclusions and Suggestions for Future Work

Finally, we conclude this dissertation with a broad set of conclusions related to our work in Section 6.1. We also discuss some interesting future work in Section 6.2.

6.1 Conclusions

As stated earlier, the goals for 5G mobile networks and the performance measures associated with them are focusing on the improvement of the future networks in terms of better capacity, capability and coverage. HetNets incorporating a layered structure of macrocells, femtocells and picocells, results in better coverage and higher spectrum efficiency. The coverage increases because the BSs in one tier can fill the coverage holes of other tiers, while the spectrum efficiency is improved because of better load balancing of users across different tiers. One of the goals of 5G mobile networks is URLLC, where ultra-high reliability and ultra-low latency can be achieved. Thus, 5G considers to benefit from the localisation in wireless networks design and optimisation, especially wireless ad-hoc sensor networks.

In this thesis, we have analysed the performance of single-tier SCN, hybrid multi-tier HetNet and ad-hoc sensor networks. One of the challenges of the analysis of these networks is random locations and number of communication nodes. An

inherent property of ad-hoc sensors networks and SCN is randomness and it occurs due to blockage, node failure, mobility of communication nodes or communication outage. Stochastic geometry is considered one of the powerful tools that enable the analysis of such random networks. It is a mathematical research area that is used to analyse and study random spatial patterns to provide mathematical and statistical models. Point process theory can be considered the main subfield of stochastic geometry.

To this end, our conclusions regarding the performance analysis of SCN, HetNet and ad-hoc sensor networks can be summarised as follows:

- We investigated the coverage performance of downlink femtocell networks when each UT is equipped with a directional antenna. We derived a closed form expression of the coverage probability using a simplified mathematical model that provides an approximate distribution for femtocell signal to co-channel interference ratio by approximating the number of strong interfering FBSs to a binomial distribution. Finally, the simulated and analytical results demonstrated that the coverage performance of femtocell networks improves considerably when directional antenna is used at the UT [11].
- We extended our work in [11], to the performance analysis of multi-tier SCN, specifically, a three-tier hybrid cellular HetNet was considered using microwave (μ Wave) links for the first two tiers and mmWave links for the last tier. The two-tiers with μ Wave links formed a wireless backhaul to the last tier with mmWave links. Because the main challenge in having a wireless backhaul is to suppress interference. Therefore, we proposed a novel and practical model where we reused the μ Wave infrastructure and equipped the BSs with directional antennas to have a robust wireless backhaul network. We assumed that the rate required by the mmWave users is comparable to that offered by the μ Wave links to solve the bottleneck rate problem. Different configurations based on the placement of the directional antennas at each tier were explored. Using the conventional minimum rate model, we analysed the key performance indicators, namely, the coverage probability, ASE and EE. We presented the

simulation results associated with these parameters. To analyse the wireless backhaul exploited in this hybrid network, we investigated an optimisation problem for the overall ASE and EE with respect to the optimal SIR threshold required for μ Wave and mmWave links. Results showed that the optimal SIR threshold required for the μ Wave tiers (wireless backhaul) depends only on the path-loss exponent and that for the mmWave tier depends on the area of LOS region. Finally, we considered the average rate under coverage and showed that the ASE and EE are strictly decreasing functions with respect to the threshold, thereby concluding that they can be maximised by choosing the lowest possible SIR threshold available in the system [6].

- We assumed a 3-D model based MASNET with randomly located sensor nodes. While many detection and localisation works focused on 2-D models, we included the height in the 3-D model to accurately model the high path-loss in low-powered sensor nodes. For this model, we derived the exact expressions of the detection probability, S -localisability probability and minimal S -localisability probability, which agree with simulations. To accurately design a sensor network, it is essential to know the minimum number of the sensors that maximises the localisability. Towards that, we maximised the minimum S -localisability to obtain the optimal sensors' density λ_s^* . We presented that to be able to detect with at least S sensors, the MASNET must have λ_s^* sensors per unit volume. We considered a MASNET with fixed locations, to observe the utility of the expressions in a practical scenario. First, we know that it is NP-hard difficult to compute the aforementioned performance metrics for a large number of sensors. Second, the expressions, which are derived and averaged for random locations, accurately provided the performance metrics of the fixed network, which emphasised the beneficial use of the stochastic geometry tools [89].
- We analysed the effect of the number of sensors on the non-cooperative target node localisation. Our work examined the target localisation using a centralised range based approach. For ToA, the work leverages an algorithm

based on a class of matrix structure called EDMs for the specific purpose of improving localisation performance which can be exploited when the FC cannot receive certain sensors' information due to fading or shadowing, etc. While this interesting approach to the problem of localisation was shown to be successful, the results presented the proposed alternating rank-based EDM algorithm outperformed the conventional LLS based algorithm for the minimum number of sensors at high delay values. When the sensors are further apart from each other and closer to the target, this is referred to as good conditioning of EDM, the localisation error results decreased leading to a better localisation performance [42].

- TDoA range based is a better approach, when no clock synchronisation is available between the target and sensor nodes. Thus, we extended the LLS algorithm [26, 91] to TDoA. Moreover, we compared the LLS performance to the WLS [53], and SRD-LS [52]. Although LLS algorithm is known to be of low complexity, its main disadvantage is that its performance is sensitive to the outliers. Thus, outliers must be identified and their effect should be minimised to have a better performance. Once we identified the outliers, we used the WLS such that the outliers have smaller weights and hence have minimum impact on the final result. However, it has been shown in [52] that SRD-LS demonstrates the best performance with respect to finding the estimated target node position. SRD-LS uses a different approach which is based on the minimisation of the LS criterion. Our results showed that the localisation error decreases when the sensors are not too far from the target node and are scattered enough. Finally, we achieved better localisation performance as the number of sensors increased as well as the number of time slots.

6.2 Suggestions for Future Work

6.2.1 Performance analysis of multi tier hybrid network using an inhomogeneous PPP

An interesting problem to solve is the performance analysis for multi tier hybrid network under the assumption of inhomogeneous PPP. An inhomogeneous PPP is a PPP where its density is not fixed. An example of an inhomogeneous PPP is a scenario where we have different densities for different subregions. To solve this we divide the whole inhomogeneous PPP region into finite number of homogenous PPP subregions.

6.2.2 Soft-Decision Detection Analysis in Ad-hoc Sensor Networks

In Chapter 4, we analysed the performance of ad-hoc sensor networks in terms of detection and S -localisability probability based on a hard decision sent from the sensors to the FC. This refers to the sensors transmits the decision as a 1 or 0 for detection or not, respectively. We want to extend this work by analysing the considered network based on soft decision, where the sensors transmit their received signal or the likelihood of the target to the FC. The FC makes its decision accordingly by combining the received signal from different sensors.

6.2.3 Localisation analysis for Heterogeneous Sensor Networks.

Another possible extension is the usage of HetNet sensor networks to detect and localise a single target. HetNet sensor networks refer to networks where the sensors have different capabilities. For example, cheap sensors that have limited analysis capabilities and smart sensors that are equipped with multiple antennas. As these HetNet sensors will have different decisions, the FC would have to combine these

decisions to reach a global decision. In other words, the FC would have to use a hybrid localisation technique such as AoA/TDoA.

6.2.4 Analysis of multiple target detection and localisation

Multiple target detection and localisation is a challenging and interesting problem. First step is detection which can be considered as a multi hypothesis problem, from this step we can have information about the number of targets present. For the localisation, we exploit the sensors accordingly to localise these targets.

Appendix A

Stochastic Geometry Background

Stochastic geometry is the area of mathematical research that is focused on providing suitable mathematical models and appropriate statistical methods to analyze and study random spatial patterns [55–57]. Stochastic geometry has been a rich branch of applied probability with several applications such as material science, image analysis, astronomy, biology, communications and more. In communications in particular, stochastic geometry has succeeded in providing a unified mathematical paradigm in order to model different types of wireless networks, characterize their operation and understand their behaviour.

One of the strengths of the analysis using stochastic geometry tools is capturing the inherent spatial randomness in wireless networks. This spatial randomness can occur due to communication outage, node failure, blockage or mobility of the communication nodes. Furthermore, the models obtained using stochastic geometry analysis takes into account other sources of uncertainties such as fading and shadowing. In some special cases, the stochastic geometry analysis may lead to closed-form expressions that governs the behaviour of the system. As a result, these expressions provide insightful design guidelines and better understanding of network operation, that is hard to be achieved using computationally intensive simulations.

A.1 Mathematical Preliminaries

In this section, some of the definitions and theorems that are commonly used in the analysis are presented.

Definition 1 *Point Process (PP)* – A point process is a countable random collection of points that repose in some space, usually the Euclidean space \mathbb{R}^d , where $d = \{2, 3\}$, for 2 or 3 dimensional space [134]. A point process and an instance (realisation) of the PP are denoted by Φ and ϕ , respectively. The number of points of a PP in the set A , $A \subset \mathbb{R}^d$, is denoted by $\Phi(A)$.

Definition 2 *Void Probability* – Given a PP Φ , its void probabilities over all bounded sets A are defined as $\mathbb{P}(\Phi(A) = 0)$, for $A \subset \mathbb{R}^d$. Two PPs are equivalent if they have the same void probability distributions for all bounded sets.

Definition 3 *Stationary* – A PP $\Phi = \{x_n\}$ is stationary if the translated PP $\Phi_x = \{x_n + x\}$ has the same distribution as Φ for every $x \in \mathbb{R}^d$.

Isotropic – A PP $\Phi = \{x_n\}$ is isotropic if the rotated PP $\mathbf{r}\Phi_x = \{\mathbf{r}x_n\}$ has the same distribution as Φ for every rotation \mathbf{r} about the origin.

Motion-Invariant – A PP Φ is motion invariant if it is stationary and isotropic.

Definition 4 *Density (Intensity) Measure λ* – For a stationary PP Φ , its density is defined as follows

$$\lambda = \frac{\mathbb{E}[(\Phi(A))]}{|A|}, \quad (\text{A.1})$$

for every $A \subset \mathbb{R}^d$, where $|A|$ is the area of A . The density of a PP is independent of a particular choice of the set A . Stationarity of a PP implies a constant density λ .

In wireless networks, a common and analytically convenient assumption for the nodes' locations distribution is the homogeneous (stationary) PPP of intensity λ .

Definition 5 *Homogeneous Poisson Point Process (HPPP)* – A stationary PP Φ of density λ is PPP if the number of points in any bounded set $A \subset \mathbb{R}^d$ has a Poisson

distribution with mean $\lambda|A|$, i.e.

$$\mathbb{P}(\Phi(A) = k) = \frac{(\lambda|A|)^k}{k!} \exp -\lambda|A|, \quad (\text{A.2})$$

and the number of points in disjoint sets are independent, i.e. for every $A \subset \mathbb{R}^d$ and $B \subset \mathbb{R}^d$ with $A \cap B = \emptyset$, $\Phi(A)$ and $\Phi(B)$ are independent.

Definition 6 *Thinning* – The process of removal of certain points from a PP is referred to thinning, usually removing the points is according to a probabilistic rule. Independent thinning means that the removal event is independent for all points. An interesting result can be seen in Proposition 14 when applying independent thinning to a PPP.

Proposition 14 If $g : \mathbb{R}^d \rightarrow [0, 1]$ is a thinning function and is applied to a HPPP Φ by deleting each point x with probability $1 - g(x)$, independently of all other points. This thinning procedure results in an inhomogeneous PPP with intensity function $\Lambda(x) = \lambda g(x)$.

An inhomogeneous PPP is defined in a similar manner as the HPPP in Definition 5, except that the intensity of the PPP is not constant but it is a function as stated in Proposition 14. There are two main theorems that we exploited in our work of the performance analysis of cellular and ad-hoc networks. These theorems are stated in the following Propositions 15 and 16.

Proposition 15 *Sum over PPPs: The Campbell Theorem*

Let Φ of density λ and $f(x) : \mathbb{R}^d \rightarrow \mathbb{R}^+$, then

$$\mathbb{E} \left[\sum_{x \in \Phi} f(x) \right] = \begin{cases} \lambda \int_{\mathbb{R}^d} f(x) dx & \text{homogeneous PPP} \\ \int_{\mathbb{R}^d} f(x) \Lambda(x) dx & \text{inhomogeneous PPP.} \end{cases} \quad (\text{A.3})$$

Proposition 16 *Product over PPPs: Probability Generating Functional (PGFL)*

Let Φ of density λ and $f(x) : \mathbb{R}^d \rightarrow [0, \infty)$ be a measurable function, then

$$\mathbb{E} \left[\prod_{x \in \Phi} f(x) \right] = \begin{cases} \exp(-\lambda \int_{\mathbb{R}^2} (1 - f(x)) dx) & \text{homogeneous PPP} \\ \exp(-\int_{\mathbb{R}^2} (1 - f(x)) \Lambda(x) dx) & \text{inhomogeneous PPP} \end{cases} \quad (\text{A.4})$$

Definition 7 *Palm Distribution* – Palm distributions are the conditional counterparts distributions for the point processes, and they occur when the point process is conditioned to have a point at $x \in \mathbb{R}^d$. The definition of Palm distribution is provided in terms of the Campbell measure, which is a measure on $\mathbb{R}^d \times N$. The reduced Campbell measure of a PP is given as

$$C^!(A \times Y) = \begin{cases} \mathbb{E} \left[\sum_{x \in \Phi \cap A} \mathbf{1}(\Phi \setminus \{x\} \in Y) \right], & \text{for any set } A \subset \mathbb{R}^d \text{ and } Y \in \mathcal{N} \\ \int_{\mathbb{R}^d} \mathbf{P}^{!x}(Y) d\Lambda(x), & \text{if } C(\cdot \times Y) \text{ is continuous with respect to } \Lambda, \end{cases} \quad (\text{A.5})$$

where $\mathbf{P}^{!x}$ denotes the reduced Palm measure of the process Φ . In other words, this is equal to conditioning on the PP having a point at the origin and not counting it.

The use of the Palm measure arises in a wireless network, for example when we calculate outage probability which requires conditioning on either receiver or transmitter location. Based on (A.5), we present the following Proposition 17

Proposition 17 *If $f(x, \phi)$ is a measurable function on $\mathbb{R}^d \times N$, then*

$$\mathbb{E} \left[\sum_{x \in \Phi} f(x, \Phi \setminus \{x\}) \right] = \int_{\mathbb{R}^d} \int_N f(x, \phi) dC^!(x, \phi). \quad (\text{A.6})$$

By combining Mecke's theorem in Proposition 17 and the definition of Campbell measure according to the intensity measure Λ , (A.6) can be rewritten as

$$\mathbb{E} \left[\sum_{x \in \Phi} f(x, \Phi \setminus \{x\}) \right] = \int_{\mathbb{R}^d} \mathbb{E}^{!x}[f(x, \phi)] d\Lambda(x). \quad (\text{A.7})$$

Finally, due to Slivnyak's theorem

Proposition 18 *The Palm measure of a PPP is given by*

$$\mathbf{P}^{!o} = \mathbf{P}. \quad (\text{A.8})$$

Proposition 18 states that an additional point at origin o does not change the distribution of the other points of the PPP. Therefore, for a HPPP, the Mecke theorem is given as

$$\mathbb{E} \left[\sum_{x \in \Phi} f(x, \Phi \setminus \{x\}) \right] = \lambda \int_{\mathbb{R}^d} \mathbb{E}[f(x, \phi)] dx. \quad (\text{A.9})$$

Definition 8 *If $v(x) : \mathbb{R}^d \rightarrow (0, \infty)$, then the conditional PGFL is*

$$\tilde{\mathcal{G}}[v] = \mathbb{E}^{!o} \left[\prod_{x \in \Phi} v(x) \right]. \quad (\text{A.10})$$

For a PPP, due to Slivnyak's theorem the conditional PGFL is equal to PGFL that is defined in Proposition 16 for homogeneous and inhomogeneous PPP.

Bibliography

- [1] T. Nguyen. Small Cell Networks and the Evolution of 5G (Part 1). <https://www.qorvo.com/design-hub/blog/small-cell-networks-and-the-evolution-of-5g>, 2017.
- [2] J. G. Andrews, S. Buzzi, W. Choi, S. V. Hanly, A. Lozano, A. C. K. Soong, and J. C. Zhang. What will 5G be? *IEEE Journal on Select. Areas in Commun.*, 32(6):1065–1082, June 2014.
- [3] Understanding 5G: Perspectives on future technological advancements in mobile, Dec. 2014.
- [4] M. Agiwal, A. Roy, and N. Saxena. Next generation 5G wireless networks: A comprehensive survey. *IEEE Commun. Surveys Tuts*, 18(3):1617–1655, 2016.
- [5] H. S. Dhillon, R. K. Ganti, F. Baccelli, and J. G. Andrews. Modeling and analysis of K-tier downlink heterogeneous cellular networks. *IEEE J. on Select. Areas in Commun.*, 30(3):550–560, April 2012.
- [6] H. Shoukry, N. Mysore Balasubramanya, S. Vuppala, and M. Sellathurai. Performance analysis of a wireless backhaul in a three-tier hybrid network with directional antennas. *IEEE Access*, 7:18332–18344, 2019.
- [7] A. Umer, S. A. Hassan, H. Pervaiz, Q. Ni, and L. Musavian. Coverage and rate analysis for massive MIMO-Enabled heterogeneous networks with millimeter wave small cells. In *IEEE 85th Veh. Technology Conference (VTC Spring)*, pages 1–5, Jun. 2017.

- [8] Y. Hao, Q. Ni, H. Li, and S. Hou. On the energy and spectral efficiency tradeoff in massive mimo-enabled hetnets with capacity-constrained backhaul links. *IEEE Trans. on Commun.*, 65(11):4720–4733, Nov 2017.
- [9] R. F. Rudd and M. Nekovee. Millimetre-wave propagation in urban clutter for 5g systems. In *Loughborough Antennas Propagation Conference (LAPC)*, pages 1–2, Nov 2017.
- [10] Y. Yang Y. Zhang and L. Dai. Energy efficiency maximization for device-to-device communication underlaying cellular networks on multiple bands. *IEEE Access J.*, 2016.
- [11] H. Shoukry, R. Qian, and M. Sellathurai. Performance analysis in indoor femtocell networks using espar antennas. In *IEEE 17th Int. Workshop on Signal Process. Advances in Wireless Commun. (SPAWC)*, pages 1–5, July 2016.
- [12] V. Chandrasekhar, J. G. Andrews, and A. Gatherer. Femtocell networks: a survey. *IEEE Commun. Mag.*, 46(9):59–67, September 2008.
- [13] Y. Shi, H. Osman, E. Hepsaydir, and J. Wang. Indoor wireless femtocell measurements. In *IEEE Int. Conference on Commun. (ICC)*, pages 2166–2171, Jun. 2015.
- [14] A. Acakpovi, K.Koumadi, and H. Sewordor. Performance analysis of femtocell in an indoor cellular network. *Int. Journal of Computer Networks and Wireless Commun. (IJCNWC)*, 3(3), Jun. 2013.
- [15] R. P. Mathur, A. Pratap, and R. Misra. Distributed algorithm for resource allocation in uplink 5G networks. In *Proceedings of the 7th ACM Int. Workshop on Mobility, Interference, and MiddleWare Management in HetNets*, page 1. ACM, 2017.
- [16] C. Li, J. Zhang, J. G. Andrews, and K. B. Letaief. Success probability and area spectral efficiency in multiuser mimo hetnets. *IEEE Trans. on Commun.*, 64(4):1544–1556, April 2016.

- [17] H. Wang, S. H. Leung, and R. Song. Uplink area spectral efficiency analysis for multichannel heterogeneous cellular networks with interference coordination. *IEEE Access*, 6:14485–14497, 2018.
- [18] Y. S. Soh, T. Q. S. Quek, M. Kountouris, and H. Shin. Energy efficient heterogeneous cellular networks. *IEEE J. on Select. Areas in Commun.*, 31(5):840–850, May 2013.
- [19] H. Jo, Y. J. Sang, P. Xia, and J. G. Andrews. Heterogeneous cellular networks with flexible cell association: A comprehensive downlink sinr analysis. *IEEE Trans. on Wireless Commun.*, 11(10):3484–3495, October 2012.
- [20] H. ElSawy, E. Hossain, and M. Haenggi. Stochastic geometry for modeling, analysis, and design of multi-tier and cognitive cellular wireless networks: A survey. *IEEE Commun. Surveys Tutorials*, 15(3):996–1019, March 2013.
- [21] U. N. Kar and D. K. Sanyal. An overview of device-to-device communication in cellular networks. *ICT Express*, 4:203–208, Dec. 2018.
- [22] P. Zhang, J. Lu, Y. Wang, and Q. Wang. Cooperative localization in 5G networks: A survey. *ICT Express*, 3:27–32, Mar. 2017.
- [23] R. Di Taranto, S. Muppirisetty, R. Raulefs, D. Slock, T. Svensson, and H. Wymeersch. Location-aware communications for 5G networks: How location information can improve scalability, latency, and robustness of 5G. *IEEE Signal Process. Magazine*, 31(6):102–112, Nov 2014.
- [24] E. Pievanelli, A. Plesca, R. Stefanelli, and D. Trincherro. Dynamic wireless sensor networks for real time safeguard of workers exposed to physical agents in constructions sites. In *2013 IEEE Topical Conference on Wireless Sensors and Sensor Networks (WiSNet)*, pages 55–57, Jan 2013.
- [25] A. R. de la Concepcion, R. Stefanelli, and D. Trincherro. Adaptive wireless sensor networks for high-definition monitoring in sustainable agriculture. In *2014 IEEE Topical Conference on Wireless Sensors and Sensor Networks (WiSNet)*, pages 67–69, Jan 2014.

- [26] W. Dargie and C. Poellabauer. *Fundamentals of Wireless Sensor Networks: Theory and Practice*. Wiley Publishing, 2010.
- [27] Z. Jia and B. Guan. Received signal strength difference based tracking estimation method for arbitrarily moving target in wireless sensor networks. *Int. Journal of Distributed Sensor Networks*, 14, Mar. 2018.
- [28] A. Mathur, T. Newe, and M. Rao. Healthcare WSN: Cluster elections and selective forwarding defense. In *9th Int. Conference on Next Generation Mobile Applications, Services and Technologies*, pages 341–346, Sep. 2015.
- [29] M. S. Kumar and R. Ramanathan. Impact of anchor position errors on WSN localization using mobile anchor positioning algorithm. In *Int. Conference on Wireless Commun., Signal Process. and Networking (WiSPNET)*, pages 1924–1928, March 2017.
- [30] J. A. del Peral-Rosado, J. A. Laspez-Salcedo, Sunwoo Kim, and G. Seco-Granados. Feasibility study of 5G-based localization for assisted driving. In *Int. Conf. on Localization and GNSS (ICL-GNSS)*, pages 1–6, Jun. 2016.
- [31] K. Witrisal, P. Meissner, E. Leitinger, Y. Shen, C. Gustafson, F. Tufvesson, K. Haneda, D. Dardari, A. F. Molisch, A. Conti, and M. Z. Win. High-accuracy localization for assisted living: 5G systems will turn multipath channels from foe to friend. *IEEE Signal Process. Mag.*, 33(2):59–70, Mar. 2016.
- [32] B. K. Chaurasia, S. Verma, and G. S. Tomar. Attacks on anonymity in VANET. In *Int. Conference on Computational Intelligence and Communication Networks*, pages 217–221, Oct 2011.
- [33] R. Kaur, T. P. Singh, and V. Khajuria. Security issues in vehicular ad-hoc network(VANET). In *2nd Int. Conference on Trends in Electronics and Informatics (ICOEI)*, pages 884–889, May 2018.
- [34] J. G. Andrews, N. Jindal, M. Haenggi, R. Berry, S. A. Jafar, D. Guo, S. Shakkottai, R. W. Heath Jr., M. J. Neely, S. Weber, and A. Yener. Re-thinking information theory for mobile ad hoc networks. *CoRR*, 2007.

- [35] Y. Miao, Z. Sun, N. Wang, and H. Cruickshank. Comparison studies of MANET-satellite and MANET-cellular networks integrations. In *Int. Conference on Wireless Commun. Signal Process. (WCSP)*, pages 1–5, Oct 2015.
- [36] H. Qin, Z. Mi, C. Dong, and H. Wang. A practical topology control method for smartphone based ad hoc networks experiment. In *8th Int. Conference on Wireless Commun. Signal Process. (WCSP)*, pages 1–5, Oct 2016.
- [37] S. Pandi, S. Wunderlich, and F. H. P. Fitzek. Reliable low latency wireless mesh networks? from myth to reality. In *2018 15th IEEE Annual Consumer Commun. Networking Conference (CCNC)*, pages 1–2, Jan 2018.
- [38] N. Yamaguchi, Y. Sakai, T. Shiraishi, S. Onishi, and T. Kowata. E-kakashi project, an agri sensor network using ad hoc network technology. In *SICE Annual Conference 2011*, pages 2808–2810, Sep. 2011.
- [39] J. Heo, J. Kim, J. Seo, S. Lim, J. Ahn, J. Ahn, W. Kim, and T. Lee. A study on the implementation of a wireless ad-hoc sensor network based on the IEEE 1451.5. In *The 9th Int. Conference on Advanced Communication Technology*, volume 1, pages 419–422, Feb 2007.
- [40] J. Jeong, S. Guo, T. He, and D. Du. APL: Autonomous passive localization for wireless sensors deployed in road networks. In *IEEE INFOCOM 2008 - The 27th Conference on Computer Commun.*, pages 583–591, April 2008.
- [41] Y. Zhou and F. Wong. Relative localization for small wireless sensor networks. In *In: Zhou Y., Kunz T. (eds) Ad Hoc Networks. Lecture Notes of the Institute for Computer Sciences, Social Informatics and Telecommunications Engineering, vol 184. Springer, Cham, 2017.*
- [42] H. Shoukry, S. Vuppala, P. Chambers, M. Sellathurai, and J. Thompson. Non-cooperative target localisation using rank based EDM approach. In *Sensor Signal Process. for Defence Conference (SSPD)*, pages 1–4, Dec 2017.

- [43] I. Bekmezci and F. Alagoz. New TDMA based sensor network for military monitoring (mil-mon). In *MILCOM 2005 - 2005 IEEE Military Commun. Conference*, volume 4, pages 2238–2243, Oct 2005.
- [44] M. Wu, J. Zhao, W. Dai, and X. Gui. A range-based adaptive target localization method in wireless sensor networks with mobile anchors. In *2018 2nd IEEE Advanced Information Management, Communicates, Electronic and Automation Control Conference (IMCEC)*, pages 1205–1209, May 2018.
- [45] S. Jadhav and K. N. Nagesh. Isolated node localization probability in wireless ad-hoc networks. In *Second Int. Conference on Advances in Electronics, Computers and Commun. (ICAECC)*, pages 1–6, Feb 2018.
- [46] D. Yildiz, S. Karagol, O. Ozgonenel, S. Tadiparthi, and M. Bikdash. Three-dimensional sensor localization using modified 3n algorithm. In *2016 IEEE 30th Int. Conference on Advanced Information Networking and Applications (AINA)*, pages 334–338, March 2016.
- [47] Y. I. Wu, H. Wang, and X. Zheng. WSN localisation using RSS in three-dimensional space; A geometric method with closed-form solution. *IEEE Sensors J.*, 16(11):4397–4404, Jun. 2016.
- [48] R. Zhang, J. Liu, X. Du, B. Li, and M. Guizani. AoA-based three-dimensional multi-target localization in industrial WSNs for LOS conditions. *Sensors (Basel, Switzerland)*, 18(8), 2018.
- [49] T. Slavisa, B. Marko, D. Rui, and B. LuÅns. On target localization using combined RSS and AoA measurements. *Sensors (Basel, Switzerland)*, 2018.
- [50] Z. Ma and K. C. Ho. ToA localisation in the presence of random sensor position errors. In *IEEE Int. Conf. Acoust., Speech and Signal Process. (ICASSP)*, pages 2468–2471, 2011.
- [51] P. Singh and S. Agrawal. TDoA based node localisation in wsn using neural networks. In *Int. Conf. Commun. Syst. and Network Technologies*, pages 400–404, 2013.

- [52] A. Beck, P. Stoica, and J. Li. Exact and approximate solutions of source localisation problems. *IEEE Trans. on Signal Process.*, 56(5):1770–1778, May 2008.
- [53] T. E. Abrudan. *Multidimensional Scaling For Localisation*. http://geta.aalto.fi/en/courses/abrudan_new_version.pdf, 2012.
- [54] B. M. Hussain and A. Jamoos. Fusion of likelihood ratio test based decisions in wireless sensor networks. In *Int. Conference on Commun., Signal Process., and their Applications (ICCSPA '15)*, pages 1–5, Feb 2015.
- [55] D. Stoyan, W. Kendall, and J. Mecke. *Stochastic Geometry and its Applications*. 2nd ed., John Wiley and Sons, 1996.
- [56] W. D. Stoyan and J. Mecke. *"Stochastic Geometry and its Applications"*. 2nd ed., John Wiley and Sons, 2008.
- [57] S. N. Chiu, D. Stoyan, W. S. Kendall, and J. Mecke. *Stochastic Geometry and its Applications*. 3rd ed., New York: John Wiley and Sons, 2013.
- [58] R. Qian and M. Sellathurai. Interference mitigation in femtocell networks using single-radio parasitic antennas. In *IEEE Int. Conf. on Commun. (ICC)*, pages 2828–2833, Jun 2015.
- [59] H. C. Lee, D. C. Oh, and Y. H. Lee. Mitigation of inter-femtocell interference with adaptive fractional frequency reuse. In *Proc. IEEE ICC*, pages 1–5, May 2010.
- [60] S. H. Ali and V. Leung. Dynamic frequency allocation in fractional frequency reused OFDMA networks. *IEEE Trans. Wireless Commun.*, 8(8):4286–4295, Aug 2009.
- [61] L. Venturino, N. Prasad, and X. Wang. Coordinated scheduling and power allocation in downlink multicell OFDMA networks. *IEEE Trans. Veh. Technol.*, 58(6):2835–2848, Jul 2009.

- [62] V. Chandrasekhar, J. G. Andrews, T. Muharemovict, Z. Shen, and A. Gatherer. Power control in two-tier femtocell networks. *IEEE Trans. Wireless Commun.*, 8(8):4316–4328, aug 2009.
- [63] R. Razavi and H. Claussen. Self-configuring switched multi-element antenna system for interference mitigation in femtocell networks. In *Proc. IEEE PIMRC*, pages 237–242, sep 2011.
- [64] A. H. Tsai, J. H. Huang, L. C. Wang, and R. B. Hwang. High capacity femtocells with directional antennas. In *Proc. IEEE WCNC*, pages 1–6, apr 2010.
- [65] S. Chen, Z. Feng, Q. Zhang, and P. Zhang. Interference mitigation and capacity optimization in cooperative public femtocell networks with cognitive enabled multi-element antennas. In *IEEE Globecom Workshops*, pages 652–656, dec 2012.
- [66] R. Razavi, L. Ho, H. Claussen, and D. López-Pérez. Improving small cell performance through switched multi-element antenna systems in heterogeneous networks. *IEEE Trans. Veh. Technol.*, PP:1, aug 2014.
- [67] Z. Su, B. Ai, Y. Lin, D. He, K. Guan, N. Wang, G. Ma, and L. Niu. User association and wireless backhaul bandwidth allocation for 5G Heterogeneous networks in the millimeter-wave band. *China Commun.*, 15(4):1–13, April 2018.
- [68] T. M. Nguyen, W. Ajib, and C. Assi. Designing wireless backhaul heterogeneous networks with small cell buffering. *IEEE Trans. on Commun.*, 2018.
- [69] U. Siddique, H. Tabassum, and E. Hossain. Downlink spectrum allocation for in-band and out-band wireless backhauling of full-duplex small cells. *IEEE Trans. on Commun.*, 65(8):3538–3554, Aug 2017.
- [70] S. Chen, H. Jin, Y. Li, and M. Peng. Performance analysis of two-tier femtocell networks in Nakagami-m fading channels. In *Int. Conference on Wireless Communications Signal Process. (WCSP)*, pages 1–5, Oct 2013.

- [71] Y. Kim, S. Lee, and D. Hong. Performance analysis of two-tier femtocell networks with outage constraints. *IEEE Trans. on Wireless Commun.*, 9(9):2695–2700, Sep 2010.
- [72] F. Zafari, A. Gkelias, and K. K. Leung. A survey of indoor localization systems and technologies. *IEEE Commun. Surveys and Tutorials*, 2018.
- [73] M. Xiao, S. Mumtaz, Y. Huang, L. Dai, Y. Li, M. Matthaiou, G. K. Karagiannis, E. Björnson, K. Yang, C. I, and A. Ghosh. Millimeter wave communications for future mobile networks. *IEEE J. on Select. Areas in Commun.*, 35(9):1909–1935, Sept 2017.
- [74] X. Ge, B. Yang, J. Ye, G. Mao, C. Wang, and T. Han. Spatial spectrum and energy efficiency of random cellular networks. *IEEE Trans. on Commun.*, 63(3):1019–1030, March 2015.
- [75] T. S. Rappaport, S. Sun, R. Mayzus, H. Zhao, Y. Azar, K. Wang, G. N. Wong, J. K. Schulz, M. Samimi, and F. Gutierrez. Millimeter wave mobile communications for 5g cellular: It will work! *IEEE Access*, 1:335–349, 2013.
- [76] T. Bai and R. W. Heath. Coverage and rate analysis for millimeter-wave cellular networks. *IEEE Trans. on Wireless Commun.*, 14(2):1100–1114, Feb 2015.
- [77] S. Singh, M. N. Kulkarni, and J. G. Andrews. A tractable model for rate in noise limited mmwave cellular networks. In *48th Asilomar Conference on Signals, Systems and Computers*, pages 1911–1915, Nov 2014.
- [78] R. W. Heath, N. González-Prelcic, S. Rangan, W. Roh, and A. M. Sayeed. An overview of signal processing techniques for millimeter wave mimo systems. *IEEE J. of Select. Topics in Signal Process.*, 10(3):436–453, April 2016.
- [79] M. S. Omar, M. A. Anjum, S. A. Hassan, H. Pervaiz, and Q. Niv. Performance analysis of hybrid 5G cellular networks exploiting mmwave capabilities in suburban areas. In *IEEE Int. Conference on Commun. (ICC)*, pages 1–6, May 2016.

- [80] M. S. Omar, S. A. Hassan, H. Pervaiz, Q. Ni, L. Musavian, S. Mumtaz, and O. A. Dobre. Multi-objective optimization in 5G hybrid networks. *IEEE Internet of Things J.*, 2018.
- [81] J. Schloemann, H. S. Dhillon, and R. M. Buehrer. Localization performance in cellular networks. In *2015 IEEE Int. Conference on Communication Workshop (ICCW)*, pages 871–876, June 2015.
- [82] J. Schloemann, H. S. Dhillon, and R. M. Buehrer. Toward a tractable analysis of localization fundamentals in cellular networks. *IEEE Trans. on Wireless Commun.*, 15(3):1768–1782, March 2016.
- [83] J. Schloemann, H. S. Dhillon, and R. M. Buehrer. A tractable analysis of the improvement in unique localizability through collaboration. *IEEE Trans. on Wireless Commun.*, 15(6):3934–3948, June 2016.
- [84] J. Werner, J. Wang, A. Hakkarainen, D. Cabric, and M. Valkama. Performance and cramer-rao bounds for doa/rss estimation and transmitter localization using sectorized antennas. *IEEE Trans. on Veh. Technology*, 65(5):3255–3270, May 2016.
- [85] E. Monier and G. Chardon. Cram r-rao bounds for the localization of anisotropic sources. In *IEEE Int. Conference on Acoustics, Speech and Signal Process. (ICASSP)*, pages 3281–3285, March 2017.
- [86] J. Wang, J. Chen, and D. Cabric. Cramer-rao bounds for joint rss/doa-based primary-user localization in cognitive radio networks. *IEEE Trans. on Wireless Commun.*, 12(3):1363–1375, March 2013.
- [87] A. Savvides, W. L. Garber, R. L. Moses, and M. B. Srivastava. An analysis of error inducing parameters in multihop sensor node localization. *IEEE Trans. on Mobile Computing*, 4(6):567–577, Nov 2005.
- [88] X. Liu, C. Liu, W. Liu, Y. Zhang, and X. Zeng. Research on wireless sensor network node localization algorithm. In *2nd Int. Conference on Frontiers of Sensors Technologies (ICFST)*, pages 170–173, April 2017.

- [89] H. Shoukry, N. Garg, and M. Sellathurai. Tractable analysis of target detection and localisation in a three dimensional MASNET. *in preparation for submission*, Sep 2019.
- [90] I. Dokmanic, R. Parhizkar, J. Ranieri, and M. Vetterli. Euclidean Distance Matrices: Essential theory, algorithms, and applications. *IEEE Signal Process. Mag.*, 32(6):12–30, Nov. 2015.
- [91] S.A. Aldalahmeh, M. Ghogho, D. McLernon, and E. Nurellari. Optimal fusion rule for distributed detection in clustered wireless sensor networks. *EURASIP J. on Advances in Signal Process.*, Jan 2016.
- [92] H. Claussen, L. Ho, and L. Samuel. An overview of the femtocell concept. *Bell Labs Technical J.*, 13(1):221–245, 2008.
- [93] A. Abdalrazik, H. Soliman, M. F. Abdelkader, and T. M. Abuelfadl. Power performance enhancement of underlay spectrum sharing using microstrip patch espar antenna. In *IEEE Wireless Commun. and Networking Conf.*, pages 1–6, April 2016.
- [94] P. E. Tsakalaki, D. Wilcox, E. De Carvalho, C. Papadias, and T. Ratnarajah. Spectrum sensing using single-radio switched-beam antenna systems. In *Proc. 7th Int. ICST Conf. on Cognitive Radio Oriented Wireless Networks and Commun. (CROWNCOM)*, pages 118–123, Jun 2012.
- [95] D. Wilcox, E. Tsakalaki, A. Kortun, T. Ratnarajah, C. Papadias, and M. Sellathurai. On spatial domain cognitive radio using single-radio parasitic antenna arrays. *IEEE J. Sel. Areas Commun.*, 31(3):571–580, Feb 2013.
- [96] A. Kausar, H. Mehrpouyan, M. Sellathurai, R. Qian, and S. Kausar. Energy efficient switched parasitic array antenna for 5G networks and IoT. In *Loughborough Antennas Propagation Conference (LAPC)*, pages 1–5, Nov 2016.
- [97] M. Rzymowski, P. Woznica, and L. Kulas. Single-anchor indoor localization using espar antenna. *IEEE Antennas and Wireless Propag. Lett.*, 15:1183–1186, 2016.

- [98] T. Gou, C. Wang, and S. A. Jafar. Aiming perfectly in the dark-blind interference alignment through staggered antenna switching. *IEEE Trans. on Signal Process.*, 59(6):2734–2744, June 2011.
- [99] C. Plapous, J. Cheng, E. Taillefer, A. Hirata, and T. Ohira. Reactance domain MUSIC algorithm for espar antennas. In *33rd European Microwave Conference Proceedings (IEEE Cat. No.03EX723C)*, volume 2, pages 793–796 vol.2, Oct 2003.
- [100] F. Baccelli and B. Blaszczyszyn. *"Stochastic Geometry and Wireless Networks, Volume II - Applications"*. Now Publishers, vol. 2, 2009.
- [101] B. Yang, G. Mao, M. Ding, X. Ge, and X. Tao. Dense small cell networks: From noise-limited to dense interference-limited. *IEEE Trans. on Veh. Technology*, 67(5):4262–4277, May 2018.
- [102] S. Weber, J. G. Andrews, and N. Jindal. The effect of fading, channel inversion, and threshold scheduling on ad hoc networks. *IEEE Trans. on Information Theory*, 53(11):4127–4149, Nov 2007.
- [103] A. Papoulis. *Probability, Random Variables, Stochastic Processes*. McGraw Hill, 1991.
- [104] B. R. Cobb, R. Rumi, and A. Salmeron. Approximating the distribution of a sum of log-normal random variables. In *Sixth European Workshop on Probabilistic Graphical Models, Granada, Spain*, 2012.
- [105] U. Siddique, H. Tabassum, E. Hossain, and D. I. Kim. Wireless backhauling of 5G small cells: challenges and solution approaches. *IEEE Wireless Commun.*, 22(5):22–31, October 2015.
- [106] J. Zhao, T. Q. S. Quek, and Z. Lei. Heterogeneous cellular networks using wireless backhaul: Fast admission control and large system analysis. *IEEE J. on Select. Areas in Commun.*, 33(10):2128–2143, Oct 2015.

- [107] N. Wang, E. Hossain, and V. K. Bhargava. Joint downlink cell association and bandwidth allocation for wireless backhauling in two-tier hetnets with large-scale antenna arrays. *IEEE Trans. on Wireless Commun.*, 15(5):3251–3268, May 2016.
- [108] P. Huang and K. Psounis. Efficient mmwave wireless backhauling for dense small-cell deployments. In *2017 13th Annual Conference on Wireless On-demand Network Systems and Services (WONS)*, pages 88–95, Feb 2017.
- [109] E. Zola, A. J. Kassler, and W. Kim. Joint user association and energy aware routing for green small cell mmwave backhaul networks. In *IEEE Wireless Commun. and Networking Conference (WCNC)*, pages 1–6, March 2017.
- [110] J. Zhao, S. Zhao, H. Qu, and G. Ren. Modeling and analyzing multi-tier millimeter/micro wave hybrid caching networks. *IEEE Access*, 6:52703–52712, 2018.
- [111] S. Singh, M. N. Kulkarni, A. Ghosh, and J. G. Andrews. Tractable model for rate in self-backhauled millimeter wave cellular networks. *IEEE J. on Select. Areas in Commun.*, 33(10):2196–2211, Oct 2015.
- [112] B. Khamidehi and M. Sabbaghian. Resource allocation for SC-FDMA femto-cell networks. *IEEE Trans. on Veh. Technology*, pages 1–1, 2017.
- [113] O. Y. Kolawole, S. Vuppala, and T. Ratnarajah. Multiuser millimeter wave cloud radio access networks with hybrid precoding. *IEEE Syst. J.*, pages 1–12, 2017.
- [114] J. G. Andrews, F. Baccelli, and R. K. Ganti. A tractable approach to coverage and rate in cellular networks. *IEEE Trans. on Commun.*, 59(11):3122–3134, November 2011.
- [115] M. D. Renzo, A. Guidotti, and G. E. Corazza. Average rate of downlink heterogeneous cellular networks over generalized fading channels: A stochastic geometry approach. *IEEE Trans. on Commun.*, 61(7):3050–3071, July 2013.

- [116] E. Turgut and M. C. Gursoy. Energy efficiency in relay-assisted mmwave cellular networks. In *IEEE 84th Veh. Technology Conference (VTC-Fall)*, pages 1–5, Sept 2016.
- [117] S. Boyd and L. Vandenberghe. *"Convex Optimization"*. Press Syndicate of the University of Cambridge, 2004.
- [118] J. Gribben and A. Boukerche. Probabilistic estimation of location error in wireless ad hoc networks. In *2010 IEEE Global Telecommunications Conference GLOBECOM 2010*, pages 1–5, Dec 2010.
- [119] M. Barkat. *Signal Detection and Estimation*. Artech House, 2nd edition, 2007.
- [120] D. R. Poulsen, M. Z. Spivey, and R. J. Marks. The poisson process and associated probability distributions on time scales. In *2011 IEEE 43rd Southeastern Symposium on System Theory*, pages 49–54, March 2011.
- [121] U. Schilcher, S. Toumpis, M. Haenggi, A. Crismani, G. Brandner, and C. Bettstetter. Interference functionals in poisson networks. *IEEE Trans. on Information Theory*, 62(1):370–383, Jan 2016.
- [122] C. Saha, M. Afshang, and H. S. Dhillon. 3GPP-inspired HetNet model using poisson cluster process: Sum-product functionals and downlink coverage. *IEEE Trans. on Commun.*, 66(5):2219–2234, May 2018.
- [123] Y. Zou and Q. Wan. Asynchronous time-of-arrival-based source localization with sensor position uncertainties. *IEEE Commun. Lett.*, 20(9):1860–1863, Sep. 2016.
- [124] L. Gui, A. Wei, and T. Val. A range-free localization protocol for wireless sensor networks. In *Int. Symp. Wireless Commun. Syst. (ISWCS), Paris*, pages 496–500, 2012.
- [125] J. Dattorro. *Convex Optimization and Euclidean Distance Geometry*. Meboo Publishing, 2005.

- [126] P. H. SchÄŹnenmann. *A Solution of the Orthogonal Procrustes Problem with Applications to Orthogonal and Oblique Rotation*. Ph.D. dissertation, Univ. Illinois, Urbana-Champaign, 1964.
- [127] H. Naseri and V. Koivunen. Cooperative joint synchronization and localization using time delay measurements. In *IEEE Int. Conf. Acoust., Speech and Signal Process. (ICASSP)*, pages 3146–3150, 2016.
- [128] G. S. Kuruoglu, M. Erol, and S. Oktug. Localization in wireless sensor networks with range measurement errors. In *Fifth Advanced Int. Conference on Telecommunications*, pages 261–266, May 2009.
- [129] *WINNER II Channel Models Part I*. Deliverable D1.1.2 Radio Channel Models, ver 1.2, 30.9.2007.
- [130] *WINNER II Channel Models Part II*. Deliverable D1.1.2 Radio Channel Measurement and Analysis Results, ver 1.1, 30.9.2007.
- [131] K. Ball. Eigenvalues of Euclidean distance matrices. *Journal of Approximation Theory*, 68(1):74–82, 1992.
- [132] N. Patwari, A. O. Hero, M. Perkins, N. S. Correal, and R. J. O’Dea. Relative location estimation in wireless sensor networks. *IEEE Trans. on Signal Process.*, 51(8):2137–2148, Aug 2003.
- [133] A. Majlesi and B. H. Khalaj. An adaptive fuzzy logic based handoff algorithm for interworking between wlans and mobile networks. In *The 13th IEEE Int. Symposium on Personal, Indoor and Mobile Radio Commun.*, volume 5, pages 2446–2451, Sept 2002.
- [134] D. J. Daley and D. Vere-Jones. *An introduction to the theory of point processes. Vol. II*. Probability and its Applications (New York). Springer, 2008.